

Development and Interpretation of Downhole Data from Downhole Vibration Monitoring Tool

By

© Rebayetur Rahman

A thesis submitted to the School of Graduate Studies
in partial fulfillment of the requirement for the degree of
Master of Engineering

July 2015

Faculty of Engineering and Applied Science
Memorial University of Newfoundland

St. John's, Newfoundland, Canada

ABSTRACT

Drillstring vibration is a major contributor to drillstring failure, downhole tool failure and has been a major concern in the oil and gas industries for several decades. Oil and gas well drilling is highly expensive. Any kind of failure during drilling operation costs several hundred thousand dollars a day. So understanding of drillstring dynamics is very important for effective and efficient drilling. Effective and efficient drilling is the key contributor for industry's success. Many academic and industry organizations have invested millions of dollars for a better drilling experience. This investigation presents the contribution to develop a downhole vibration monitoring tool and interpretation method of measured data for better understanding of downhole dynamic condition. All three modes of vibration-axial, torsional, lateral vibration can be captured by this tool using accelerometers and magnetometer. Recorded data can be used to study different vibration modes. Data is processed using moving average filter to remove noise in the data and frequency spectra are created based on an FFT analysis algorithm. A 2D bond graph model is also developed using lumped segment approach to predict downhole vibration. However, this 2D model has some limitations. Data used for analysis in this thesis is obtained from field trial experiments conducted under Advanced Drilling Laboratory, Memorial University of Newfoundland.

ACKNOWLEDGEMENT

First of all, I would like to show my sincere gratitude to the almighty God, the most gracious and merciful for giving me the courage, strength and patience to carry out this research work. I would like to express my deepest gratitude to my academic supervisors- Dr. Geoff Rideout and Dr. Stephen Butt for their guidance, professional supervision, constant encouragement and all kind of support throughout the work since the day I started working with them. It was a great learning experience and a great pleasure to work with them. This research work would be incomplete without their support and assistance in every stage. I would like show my deepest appreciation to the current and former Project Managers namely Farid Arvani (former), Brock Gillis (former) and Pushpinder Sing Rana (current) in Advanced Drilling Laboratory for their assistance, useful suggestions and comments during the research work. I would like to thank all the current and previous Advanced Drilling Laboratory group members specially Ahmed Elnahas for his expert opinion and suggestions. I also would like to thank Moya Crocker, Academic Program Administrator of Graduate Studies at Memorial University of Newfoundland for her support. Finally, I would like to thank Mohammed Raju Hossian, Mahmud Sharif Sazidy, Mahmuda Tanni and Md. Mejbahul Sarker for their support in any event during my program of study and research work.

This research has been conducted at Advanced Drilling Laboratory, Memorial University of Newfoundland and funded by the Atlantic Canada Opportunities Agency (AIF Contract no: 781-2636-1920044), Research and Development Corporation (RDC) of Newfoundland

and Labrador, Suncor Energy and Husky Energy. I am grateful to them for the funding provided to conduct this investigation.

Finally, I would like to show my deepest gratitude to my parents, brother and my sisters for their inspiration to complete this work and would like to dedicate this work to them.

TABLE OF CONTENTS

ABSTRACT	i
ACKNOWLEDGEMENT	ii
TABLE OF CONTENTS.....	iv
LIST OF FIGURES	viii
LIST OF TABLES	xii
NOMENCLATURE	xiii
1 CHAPTER 1: INTRODUCTION	1
1.1 Introduction	1
1.2 Drilling System.....	2
1.3 Research Objectives	6
1.4 Thesis Outline.....	7
2 CHAPTER 2: LITERATURE REVIEW	9
2.1 Introduction	9
2.2 Axial Vibration (Bit Bounce)	10
2.2.1 Bit Bounce Detection Criteria.....	11
2.2.2 Reasons	11
2.2.3 Solutions	12
2.3 Torsional Vibration (Stick Slip)	12
2.3.1 Stick Slip Detection Criteria	13
2.3.2 Reasons:	14

2.3.3	Solutions	14
2.4	Lateral Vibration (Bit/BHA Whirl)	15
2.4.1	Bit Whirl	15
2.4.2	BHA Whirl.....	16
2.4.3	Detection Criteria.....	17
2.4.4	Reasons	18
2.4.5	Solutions	18
2.5	Coupling	19
2.6	Downhole Sensor Sub Background.....	19
3	CHAPTER 3: DOWNHOLE SENSOR SUB.....	26
3.1	Introduction	26
3.2	Mechanical Design	27
3.3	Electrical Design.....	29
3.4	Electronics	32
3.4.1	ADXL345 Accelerometers	32
3.4.2	HMC5983 Magnetometer	33
3.4.3	Arduino Leonardo Microcontroller Board.....	33
3.4.4	MicroSD Card Breakout Board.....	34
4	CHAPTER 4: FIELD TRIAL DATA INTERPRETATION	36
4.1	Introduction	36
4.2	Field Trial	36
4.3	Data Calculation	37

4.4	Signal Processing.....	40
4.4.1	Filtering.....	41
4.4.1.1	Moving Average Filter	43
4.4.1.1.1	Procedure.....	46
4.4.1.1.2	Results.....	49
4.4.2	Fast Fourier Transform (FFT).....	61
4.4.2.1	Test Signal	62
4.4.2.2	FFT Results.....	64
4.5	RPM.....	73
5	CHAPTER 5: FIELD VIBRATION PREDICTION	77
5.1	Introduction	77
5.2	Natural Frequency	77
5.3	Theory of Vibration.....	79
5.3.1	Axial Vibration	79
5.3.2	Torsional Vibration.....	82
5.3.3	Lateral Vibration.....	85
5.4	Simulation.....	88
5.4.1	Bond Graph Background	88
5.4.2	Bond Graph Basic Elements	89
5.4.2.1	Basic 1-Port Elements.....	89
5.4.2.2	Basic 2-Port Elements.....	92
5.4.2.3	Basic 3-Port Junction Elements.....	93

5.4.2.4	Causality	96
5.4.3	Model & Simulation Results.....	99
5.4.3.1	Bond Graph Model	99
5.4.3.2	Results and Model Validation	104
6	CHAPTER 6: SUMMARY AND CONCLUSIONS.....	107
6.1	Introduction	107
6.2	Summary of Present Work	108
6.3	Limitations of Present Work.....	109
6.4	Recommendations for Future Work	110
	REFERENCES	111
	APPENDICES	116

LIST OF FIGURES

Figure 1.1 Schematic of a conventional rotary drilling system [5].....	4
Figure 1.2 (a) PDC bit and (b) RC bit [6]	6
Figure 2.1 Different mode of drillstring vibration [9]	10
Figure 2.2 Bit failure due to bit bounce [13]	12
Figure 2.3 Bit failure due to stick slip [13].....	14
Figure 2.4 BHA whirl [9].....	17
Figure 2.5 PDC bit damage from backward whirl [10]	18
Figure 2.6 Sensor mounting configuration of DVMCS tool [22].....	20
Figure 2.7 Schematic of DVMCS tool [22]	21
Figure 2.8 VMS tool [23].....	22
Figure 2.9 Assembly drawing of bit based data acquisition system [24]	23
Figure 2.10 Downhole Dynamics Sensor layout [26].....	25
Figure 3.1 Mechanical design of downhole sensor sub [27]	27
Figure 3.2 Detail view of the central hub [27].....	29
Figure 3.3 Circuit diagram of the electronics	30
Figure 3.4 Electrical power supply to the electronics.....	31
Figure 3.5 ADXL345 accelerometer [28].....	32
Figure 3.6 HMC5893 magnetometer [30].....	33
Figure 3.7 Arduino leonardo [31]	34
Figure 3.8 MicroSD breakout board [32].....	34
Figure 4.1 Aerial view of Greenslades Construction Quarry B site [34].....	37

Figure 4.2 Sensor package layout	38
Figure 4.3 Filter bands [37].....	42
Figure 4.4 Different types of filter response [38]	43
Figure 4.5 Example of a moving average filter (original signal) [39]	44
Figure 4.6 Example of a moving average filter (after noise reduction) [39]	45
Figure 4.7 Example of a moving average filter (after noise reduction) [39]	45
Figure 4.8 20-sim model for axial displacement calculation.....	47
Figure 4.9 20-sim model for lateral displacement (whirl) calculation.....	47
Figure 4.10 20-sim model for torsional acceleration calculation.....	48
Figure 4.11 Demeaned axial acceleration using moving average filter	49
Figure 4.12 Demeaned axial displacement using moving average filter	50
Figure 4.13 Demeaned axial acceleration using moving average filter	50
Figure 4.14 Demeaned axial displacement using moving average filter	51
Figure 4.15 Demeaned axial acceleration using moving average filter	51
Figure 4.16 Demeaned axial displacement using moving average filter	52
Figure 4.17 Demeaned axial acceleration using moving average filter	52
Figure 4.18 Demeaned axial displacement using moving average filter	53
Figure 4.19 Demeaned lateral acceleration using moving average filter.....	54
Figure 4.20 Demeaned lateral acceleration using moving average filter.....	55
Figure 4.21 Demeaned lateral acceleration using moving average filter.....	55
Figure 4.22 Demeaned lateral acceleration using moving average filter.....	56
Figure 4.23 Drillstring whirl	57
Figure 4.24 Drillstring whirl	57

Figure 4.25 Drillstring whirl	58
Figure 4.26 Drillstring whirl	58
Figure 4.27 Demeaned angular velocity using moving average filter	59
Figure 4.28 Demeaned angular velocity using moving average filter	60
Figure 4.29 Demeaned angular velocity using moving average filter	60
Figure 4.30 Demeaned angular velocity using moving average filter	61
Figure 4.31 Separate test signals for FFT test.....	62
Figure 4.32 Combined test signals for FFT test.....	63
Figure 4.33 Frequency spectrum for FFT test.....	63
Figure 4.34 Frequency spectrum for axial vibration.....	65
Figure 4.35 Frequency spectrum for axial vibration.....	65
Figure 4.36 Frequency spectrum for torsional vibration.....	67
Figure 4.37 Frequency spectrum for torsional vibration.....	67
Figure 4.38 Frequency spectrum for torsional vibration.....	68
Figure 4.39 Frequency spectrum for torsional vibration.....	68
Figure 4.40 Frequency spectrum for lateral vibration (AlatX)	69
Figure 4.41 Frequency spectrum for lateral vibration (AlatY)	70
Figure 4.42 Frequency spectrum for lateral vibration (AlatX)	70
Figure 4.43 Frequency spectrum for lateral vibration (AlatY)	71
Figure 4.44 Frequency spectrum for torsional vibration with low pass filter.....	72
Figure 4.45 Frequency spectrum for torsional vibration with low pass filter.....	72
Figure 4.46 Magnetometer data smoothing for RPM calculation.....	73
Figure 4.47 Average rotary speed of drillstring.....	74

Figure 4.48 Instantaneous rotary speed of drillstring	74
Figure 4.49 Average rotary speed of drillstring.....	75
Figure 4.50 Instantaneous rotary speed of drillstring	75
Figure 5.1 Mass spring system [47].....	78
Figure 5.2 Longitudinal vibration of a bar [41]	79
Figure 5.3 Natural frequency (axial) vs length graph	81
Figure 5.4 Torsional vibration of a shaft [41].....	82
Figure 5.5 Natural frequency (torsional) vs length graph.....	84
Figure 5.6 Lateral vibration of a beam [41].....	85
Figure 5.7 Natural frequency (lateral) vs length graph.....	87
Figure 5.8 Bond graph representation ideal sources.....	90
Figure 5.9 Bond graph representation of inductive, capacitive and inductive element.....	90
Figure 5.10 Bond graph representation of basic 2-port elements	92
Figure 5.11 Bond graph representation of 0-junction.....	94
Figure 5.12 Bond graph representation of 1-junction.....	95
Figure 5.13 Causal marks	96
Figure 5.14 Different causality combination	96
Figure 5.15 Schematic of rigid body segment	99
Figure 5.16 Schematic of a joint section.....	100
Figure 5.17 Bond graph model of a rigid body.....	102
Figure 5.18 Bond graph model of a joint.....	103
Figure 5.19 Bond graph model of a 2D drillstring model.....	104

LIST OF TABLES

Table 5.1 Theoretical natural frequency for axial vibration	81
Table 5.2 Theoretical natural frequency for torsional vibration	84
Table 5.3 Theoretical natural frequency for lateral vibration	87
Table 5.4 Effort and flow variables in different physical domain	89
Table 5.5 Causality for basic 1-port elements.....	97
Table 5.6 Causality for basic 2-port elements.....	98
Table 5.7 Causality for basic 3-port elements.....	98
Table 5.8 Axial Natural Frequency.....	105
Table 5.9 Lateral Natural Frequency	105
Table 5.10 Lateral natural frequency with axial load for 30m length.....	106
Table 5.11 Lateral natural frequency with axial load for 60m length.....	106

NOMENCLATURE

A	Cross-sectional area of drillstring
A_{axial}	Axial acceleration
$A_{lateral}$	Lateral acceleration
A_{shock}	Axial acceleration while shock
$A_{torsional}$	Torsional acceleration
A_{lx}	Lateral acceleration component in x-axis
A_{ly}	Lateral acceleration component in y-axis
a_{1x}	Recorded axial acceleration from accelerometer # 1
a_{2x}	Recorded axial acceleration from accelerometer # 2
a_{3z}	Recorded axial acceleration from accelerometer # 3
a_{1x}'	Corrected axial acceleration from accelerometer # 1
a_{2x}'	Corrected axial acceleration from accelerometer # 2
a_{3z}'	Corrected axial acceleration from accelerometer # 3
E	Modulus of elasticity
f_n	Natural frequency in hertz
G	Modulus of rigidity
k	Stiffness of spring
l	Drillstring length

m	Drillstring mass
n	Number of segments
P	Applied load
P_{cri}	Critical load
ω	Angular velocity in radians
ω_n	Natural frequency in radian/s
ρ	Density of drillstring material
ν	Poisson's ratio

ABBREVIATION

BHA	Bottom Hole Assembly
BOP	Blowout Preventer
FFT	Fast Fourier Transform
MWD	Measurement While Drilling
NPT	Non-Productive Time
PDC	Polycrystalline Diamond Compact
RC	Roller Cone
ROP	Rate of Penetration
RPM	Revolution Per Minute
WOB	Weight on bit

SYMBOLS FOR BOND GRAPH

C Capacitive element

I Inductive element

R Resistive element

Se Efforts source

Sf Flow source

MTF Modulated Transformer

1 CHAPTER 1:

INTRODUCTION

1.1 Introduction

Drilling process is widely used in oil and gas exploration industries. The very first oil wells were drilled in China in earlier 4th century. They drilled approximately 243 *m* using drill bits attached to bamboo poles [1]. The first ever commercial oil well was drilled in North America was in Oil Springs, Ontario, Canada in 1858 [1]. Since then the technology for oil and gas drilling has been developing day by day and reaching milestones one after another. Drilling in oil and gas industries is very expensive, especially for offshore drilling. Drilling

operation costs several hundred thousand dollars a day for a single well. So it is very important in the drilling industries to reduce the drilling Non-Productive Time (NPT). NPT is the time creditable to events in drilling that delays the progress of the planned activities that includes bit failure, downhole tool failure, connection failure etc. This can happen due to severe downhole vibration. Drillstring vibration is a very common phenomena during drilling operation and a major contributor to downhole tool failure. With the knowledge of downhole dynamic conditions, downhole drilling vibration can be reduced and expensive downhole tools can be saved from early failure. Thus the Non-Productive Time can be reduced which will reduce the operating cost.

The main goal of this present work is to develop a downhole vibration monitoring tool and develop the interpretation method of the downhole data recorded in a field trial by this vibration monitoring tool known as sensor sub. Another goal is to develop a simple multibody model to capture axial and lateral vibration.

This chapter will give a general introduction of drilling systems and equipment, and an outline of the research work.

1.2 Drilling System

Various drilling methods have been developed in oil and gas industries because of different geologic conditions ranging from hard rock to sand/gravel. Among all the drilling process “rotary drilling” is the most frequently used drilling process in oil and gas exploration and production. In the conventional rotary drilling process, a drill bit is attached on the lower

end of a drill string and the drill string rotates with high RPM. The basic process of a rotary drilling system involves the following [2]:

- Downward force acting on drill bit.
- Drill bit rotation.
- Drilling fluid circulation.

A drilling operation involves the following six basic functions to produce a hole [3]:

- Transmitting energy to the rock face from the surface.
- Reduction of the rock from its monolithic state.
- Removal of the rock cuttings from wellbore.
- Control formation fluid and maintain wellbore pressure.
- Borehole maintenance during drilling.
- Preservation and control of the borehole.

In general, a conventional rotary drilling system consists of power generation unit, hoisting system, fluid circulation system, rotary drive, well control system, data acquisition and monitoring system. A schematic of conventional rotary drilling system is shown in Figure 1.1.

Internal combustion engines, mostly diesel electric power engines are used in the drilling rig as its power source. Most rotary drilling rigs need 1000 – 1300 horsepower, while shallow drilling rigs need 500 horsepower [4]. The power system mainly supplies power to the rotary system, hoisting system, drilling fluid circulation system and auxiliaries like

blowout preventer (BOP), water pumps etc. Drill pipe acts as a prime mover which converts the electrical energy generated from a diesel engine into mechanical energy. This mechanical energy is transmitted to the rock surface through drill collar, drill bit and other drill string components, which is used to crush the rock.

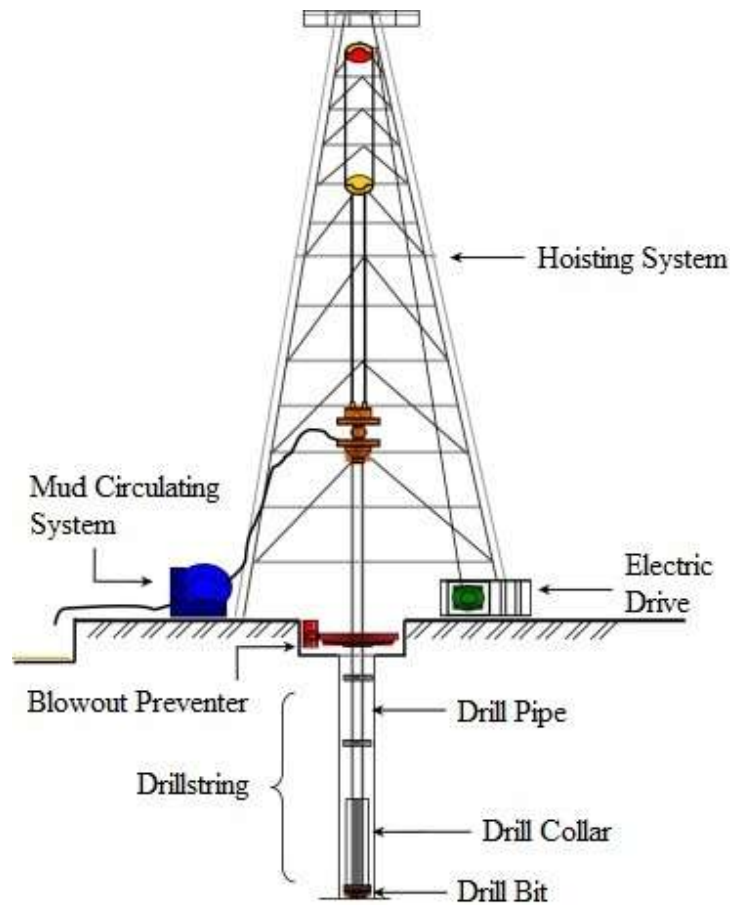


Figure 1.1 Schematic of a conventional rotary drilling system [5]

The main task of the hoisting system is to lower and raise the drill string, casings, and downhole tools into or out of the well. Basically the hoisting system in a drilling rig is made up of draw works, mast or derrick, crown block, traveling block and wire rope.

The main purpose of a fluid circulation system is to remove the rock cuttings from the bottom hole surface during drilling operation. A drilling fluid is used in the circulation system which is known as mud. Besides removing the rock cuttings, this mud also acts as a coolant for the drill string components. The drilling fluid could be water, oil or synthetic based. A fluid circulating system is composed of a high pressure mud pump, drill string, return annulus, mud pit, mud treatment and storage unit.

The rotary system transmits rotation to the drill string and rotates the bit. The rotary system consists of swivel, kelly, rotary drive, rotary table, drill pipe, drill collar and drill bit. The drill bit is connected to the drill string at the bottom and rotates along with the drill string rotation. Mainly drill bit crushes the rock and penetrates the rock formation when it rotates at a high speed. There are different types of bits but two types of bit are used mostly during drilling – Roller Cone (RC) bit and Polycrystalline Diamond Compact (PDC) bit. Most RC bits have three rotating cones with teeth. RC bits are the most commonly used drill bit in rotary drilling operations. RC bit crushes the rock by rolling its cones and teeth when the bit comes in contact with the rock surface. PDC bits don't have any rolling parts. The cutters are installed on its body and cuts the rock by shear action. This type of bits are usually used for soft to medium hard rock formation for their faster rate of penetration. RC and PDC bit are shown in Figure 1.2.

Well control system prevents the uncontrolled flow of formation fluids into the wellbore. A well control system is needed for safe drilling operation. Failure of the well control system results an uncontrolled flow of formation fluids which can be disastrous. A Blowout Preventer (BOP) is used to prevent that.



Figure 1.2 (a) PDC bit and (b) RC bit [6]

To operate drilling operation safely and efficiently it is necessary to monitor the well and the drilling operation to detect any problems. It is also necessary to monitor downhole condition to prevent any kind of failure downhole. Analyzing the recorded data will help preventing those unwanted occurrence which may cost several hundred thousand dollars.

1.3 Research Objectives

The main objective of this investigation is to develop a downhole vibration monitoring tool and developing an interpretation method of downhole vibration data to learn about the downhole dynamics condition. Downhole dynamics conditions are very important to protect the expensive downhole tools from the violent vibration induced during drilling operation. This investigation is a part of a research project in Advanced Drilling Laboratory at Memorial University of Newfoundland. In industries different types of downhole vibration monitoring tools already exist but these tools are too expensive and have

limitations such as low sampling rate, small data storage, location of the data recorder etc. This is why this investigation has been initiated to overcome these drawbacks and develop a low cost downhole sensor sub as a research project in Advanced Drilling Laboratory. The tool developed in the Advanced Drilling Laboratory is used in a field experiment as a part of the research work and the data interpretation method is developed using the data recorded from the downhole vibration monitoring sensor sub. Another objective is to develop a 2D model coupling axial and lateral vibration together which can be used to predict field vibration after proper tuning.

1.4 Thesis Outline

The complete investigation by the author is presented in this thesis which consists of six chapters in total.

Chapter 1 addresses the general background, objectives and a brief introduction of this thesis work.

Chapter 2 involves a brief review of major downhole vibration modes, their detection criteria, reasons for induced vibration and their solution to give an overall idea to the readers about downhole vibration. Also, the background of some downhole vibration monitoring tools and their positive sides and drawbacks are discussed.

Chapter 3 gives a brief description of the downhole vibration monitoring tool developed in Advanced Drilling Laboratory at Memorial University of Newfoundland. A brief

description of the mechanical design, electrical circuit design and the electronics used in the monitoring tool is provided in this chapter.

Chapter 4 gives an interpretation method for the data recorded by the downhole monitoring tool. A description of signal processing and how the data are processed is discussed in this chapter along with the results obtained after processing.

Chapter 5 provides the basic concept of natural frequency, a brief description of bond graph and construction of a 2D bond graph model to predict vibration which can be used to validate the field data from the developed tool. A comparison between theoretical natural frequency and the natural frequency obtained from the 2D model is also provided to validate the model in this chapter.

Chapter 6 presents a summary and limitation of this work. This chapter also provides some recommendations for future work.

2 CHAPTER 2:

LITERATURE REVIEW

2.1 Introduction

Drillstring vibration is a major contributor to downhole tool failure. Drillstring damage, downhole measurement tools damage, and bit failure from the vibration induced while drilling is a major concern in the oil and gas drilling industry. The damage caused by this vibration costs the drilling industry with time and money. Study shows that this bad vibration can increase the drilling cost significantly. An estimated increase of 2% to 10% of well costs can rise from vibration related problems [7]. Understanding the drillstring dynamics is very important for effective and efficient drilling. Drilling dynamics is a very complex problem and performing detailed analyses of this, is an intensive engineering

process. Drilling vibration is divided into three different types or modes – axial, torsional and lateral [7, 8].

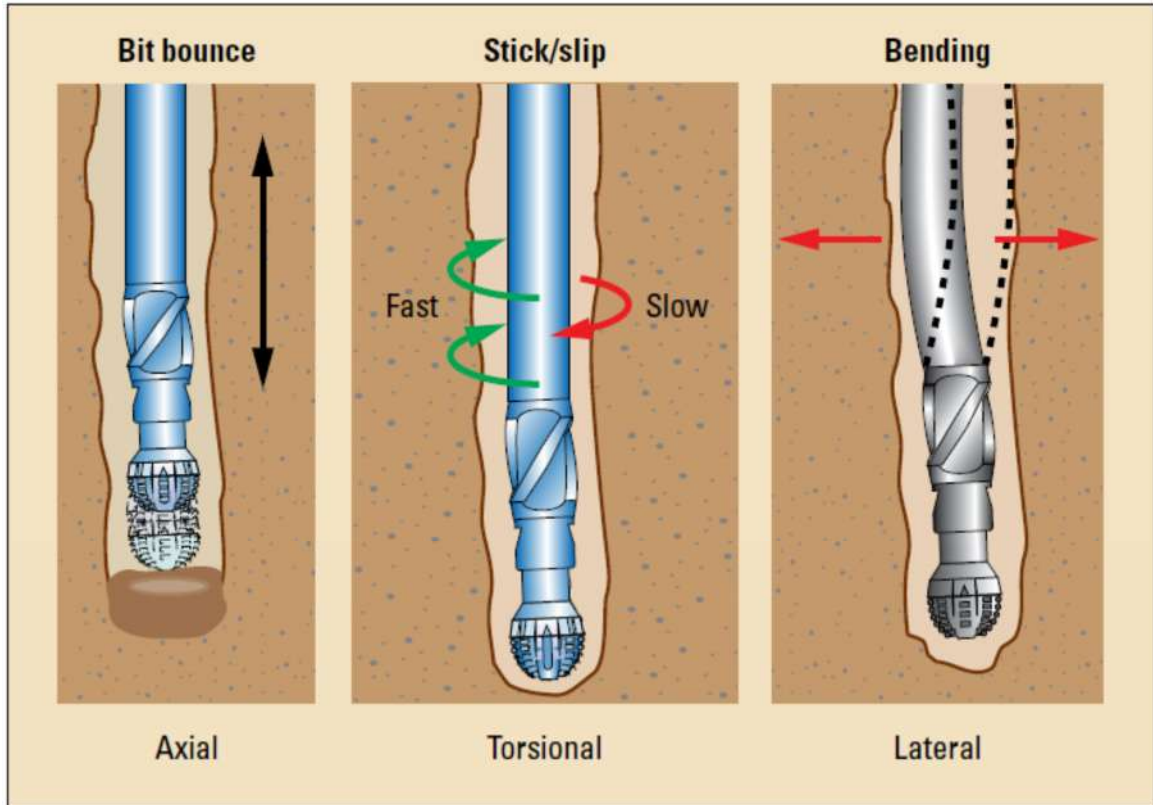


Figure 2.1 Different mode of drillstring vibration [9]

2.2 Axial Vibration (Bit Bounce)

Axial vibration of a drillstring involves the motion of the drillstring along its longitudinal direction. Axial vibration causes the drill string and the tools/components attached to it to vibrate or bounce on the rock formation. This phenomena is known as “bit bounce”. Variation in weight on bit (WOB), changes in mud pressure and the interaction of the bit cutting structure on the formation are the main reasons for axial vibration [10]. Axial

vibration/ bit bounce is normally developed when large diameter roller cone (RC) bits are used in hard formations. Roller cone bits usually exhibit an unstable bottom hole pattern. Due to erratic interaction of the bit with the bottom of the well i.e. rock surface, the bit loses contact with the rock formation. As a result severe longitudinal motion develops in the drillstring which results in axial vibration in the surface, top drive or rotary table. At that time fluctuation of WOB can be seen on the WOB indicator. This mechanism can result in premature bit failure, BHA component failure and reduced rate of penetration (ROP). Potential cures include reducing WOB and increasing RPM. The range of frequency for bit bounce is 1 – 10Hz [11]. The bit bounce phenomena is shown in Figure 2.1.

2.2.1 Bit Bounce Detection Criteria

Bit bounce can be detected by large surface vibration, axial movement of drill pipe at surface. If bit bounce occurs there will be a large fluctuation in weight on bit (WOB). High level of axial vibration can be seen from Measurement While Drilling (MWD) tools and the penetration rate will be reduced significantly. [11]

2.2.2 Reasons

Bit bounce occurs due to axial harmonic resonance of drillstring, excessive RPM, hard formation with high compression strength. It can also take place if large diameter roller cone bit is used and/or excessive WOB is applied with high RPM. [12]

2.2.3 Solutions

Bit bounce can be resolved by changing RPM and WOB combinations to get a stable drilling situation, by changing the drill bit to PDC bit or by using shock sub in the BHA. [12]



Figure 2.2 Bit failure due to bit bounce [13]

2.3 Torsional Vibration (Stick Slip)

Torsional vibration is the result of the periodic rotational acceleration and deceleration of the drillstring in a drilling assembly. It is caused by irregular downhole rotation. It happens when the rotation of the drill string is slowed down or stopped at the bottom and released when the torque overcomes the static friction resisting string rotation. If torsional vibration

is severe, stick slip can occur. Stick-slip is the phenomena where the drillstring stops or slows down rotation to a point where the drillstring torque increases and then rapidly releases the energy once the BHA and bit becomes free and starts rotating again. In the slip or release phase, the drillstring spins dangerously at high speed which causes destructive vibrations in the drilling assembly. During this time often the downhole rotary speed goes 2 – 3 times higher than the nominal rotary speed, but this can go as high as 15 times [12]. Stick slip can take place in the downhole regardless of having a constant surface RPM. Stick slip is caused largely by interaction with the formation. The frictional forces between the drillstring, BHA, drill bit and the wellbore cause stick slip to take place. Stick slip frequency range is below 1 Hz [11]. As the rotary system in the surface acts as clamp, most of the torsional vibration attenuates and is not physically visible in the surface. It can be identified from torque indicator or MWD tools data. It causes serious failure in drillstring connections, MWD tools and bit, and slows down the drilling process. Extensive analysis of downhole vibration data shows that slick slip occurs in 50% of drilling time [15]. The stick slip phenomena is shown in Figure 2.1.

2.3.1 Stick Slip Detection Criteria

Stick slip can be detected by large variation in surface torque and downhole RPM, reduced penetration rate, increased MWD shock counts, MWD tool failure, bit impact damage, cutting structure damage (generally seen over the nose of the bit), over torqued connections, washouts and twist-offs etc. Stick slip can be also detected by analyzing downhole memory data. [11]

2.3.2 Reasons:

Stick slip can occur due to incorrect bit selection. Stick slip takes place if overly aggressive PDC bit is used. It can also happen due to improper BHA stabilization, excessive bend in mud motor, high WOB with low RPM, insufficient mass of drill collar and drill pipe, abrasive formation (with high friction coefficient). [12]

2.3.3 Solutions

Stick slip occurs at a rotary speed below a certain threshold value. This threshold value depends on system parameters such as design of the drill-string, mud, bit type, BHA and Weight on Bit (WOB). Stick slip can be reduced by changing drilling parameters such as increasing RPM and reducing WOB, by increasing flow rate for increased motor RPM, increasing mud lubricity. Rotary drive system (rotary table or top drive) in higher gear also can reduce stick slip. Other ways to reduce stick slip are lifting off bottom and attempt to restart drilling without initiating stick-slip, increasing RPM and lowering WOB. [11]

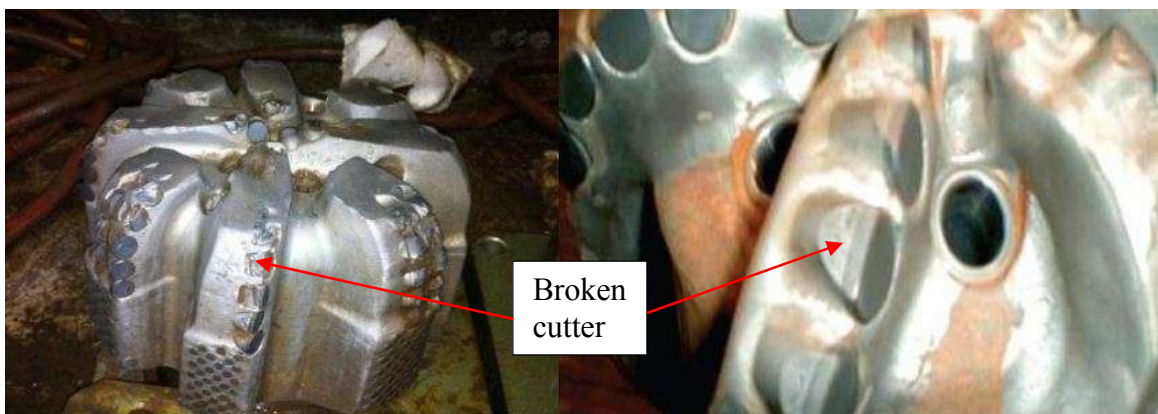


Figure 2.3 Bit failure due to stick slip [13]

2.4 Lateral Vibration (Bit/BHA Whirl)

Lateral vibration is the most destructive type of vibration among all three types of vibration (axial, torsional, and lateral) [16]. Most of the downhole tool failure and drillstring failure occurs due to the presence of lateral vibration while drilling. It occurs when the drillstring or the stabilizers rotate eccentrically from the geometric center of the wellbore. The cause of lateral vibrations is often hard to pinpoint. Typically, the lateral vibration is caused by high bending stress in the BHA and drillstring resulting in the assembly impacting on the wellbore wall. Lateral vibration can cause extreme damage to the drillstring and downhole tools as they collide with the wellbore wall at a very high velocity. Lateral vibrations are commonly referenced as ‘Bit Whirl’ or ‘BHA Whirl’.

2.4.1 Bit Whirl

Bit whirl is the eccentric rotation of the bit about a point other than its geometric center [11]. Bit whirl is mostly visible in PDC bits. RC bit penetrates the bottom of the hole more and does not allow sideway movements around the face of the bit. Bit whirl can be classified as forward whirl and backward whirl. During the forward whirl, the center of rotation rotates in the same direction as the drillstring. Backward whirl is where the vibration causes the center of the rotation to rotate in the opposite direction to the drillstring. Backward whirl is more complex and more violent. Backward whirl causes significant damage to the bit due to high and irregular impact loads on the bit. The high shocks induced by bit whirl can cause premature bit and/or BHA failure [17]. Bit whirl is basically generated by two major factors [18]:

1. Center of the rotation, which does not stay as the center of the bit or drillstring.
2. High rotary speed, which generates high centrifugal force that pushes the bit towards the wall of the wellbore.

Bit whirl is not possible to detect from the surface but bit will have noticeable damage at the end of the run. Bit whirl is usually identified by the downhole measurement tool when high lateral shock is recorded. Bit whirl frequency is between 10 – 100 Hz [10].

2.4.2 BHA Whirl

BHA whirl is the eccentric rotation of the BHA about a point other than its geometric center [11]. This rotation can be either in the same direction as the drillstring rotation, in reverse, or chaotic. If the rotation is in the same direction as drillstring, it is forward BHA whirl and if the rotation is in the opposite direction of the drillstring rotation, it is backward BHA whirl. The rotational walk mechanism is the characteristic of the section of the BHA that are touching the wall of the wellbore and tend to walk backwards due to rubbing contact with the borehole. The high shocks generated from the BHA whirl cause premature bit failure and BHA component failure. Drillstring components are subjected to extreme fatigue and flattened on one side [17]. Whirl frequency for BHA whirl is 5 – 20 Hz [10]. Forward BHA whirl and backward BHA whirl is shown in Figure 2.4. The best way to identify the BHA whirl is by monitoring downhole acceleration [19].

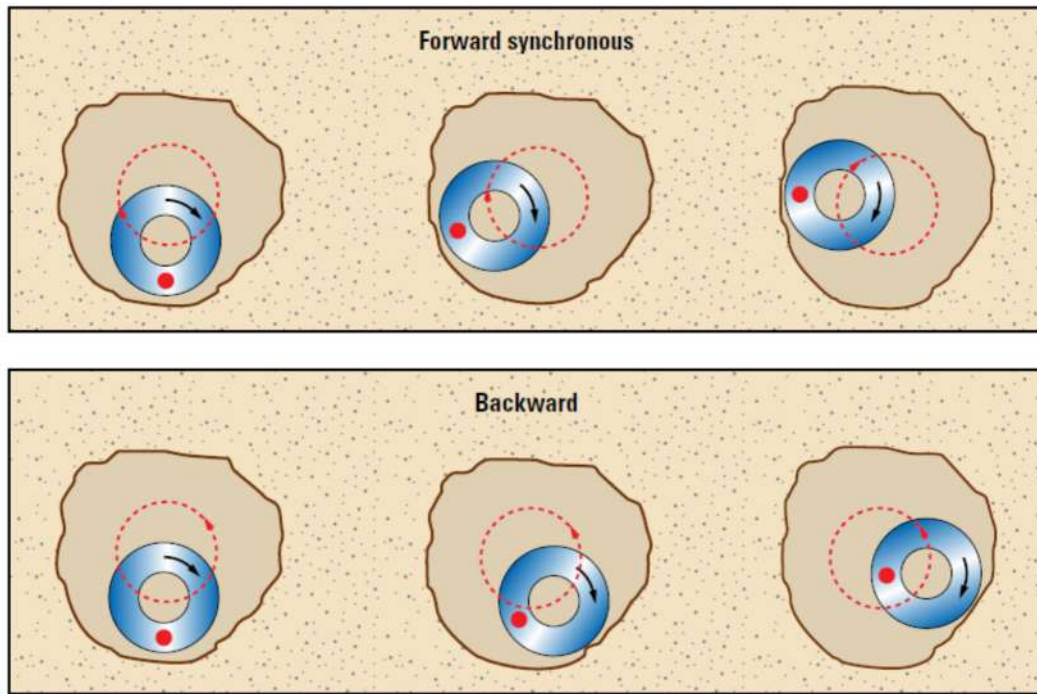


Figure 2.4 BHA whirl [9]

2.4.3 Detection Criteria

Bit/BHA whirl can be identified from high RPM and low WOB, increased surface and downhole torque, high frequency downhole lateral vibration, increased MWD shock counts. The ROP will be reduced due to BHA whirl. It also causes connection fatigue crack on BHA components, localized wear on stabilizers and tool joints, damage to stabilizer blades etc. [11].

2.4.4 Reasons

Bit/BHA whirl can occur due to several reasons such as incorrect bit selection, lack of lubrication in mud, lack of BHA stabilization, low WOB with high RPM, excessive heavy BHA in a high angle hole, formation with high friction coefficient etc. [12].

2.4.5 Solutions

Bit/BHA whirl can be reduced by increasing WOB and reducing RPM, increasing the diameter of the drill pipe to provide more torque, monitoring MWD tool data, using stabilizer or roller reamer to improve borehole quality etc. A proper bit selection with high Lateral Stability Index (LSI) can also reduce bit/BHA whirl [12].



Figure 2.5 PDC bit damage from backward whirl [10]

2.5 Coupling

Drillstring vibrations are generally quite complex in nature. Coupling is the process where one vibration mode initiates another, to the extent of all three modes (axial, lateral and torsional) occurring in drillstring at the same time. All three modes of vibration may occur at the same time and coupled intimately. High downhole RPM caused by stick slip can excite severe axial and lateral vibrations in the BHA, which may cause bit bounce, bit wear and low ROP [20]. Stick slip is a self-induced vibration and generally disappears if the surface RPM is increased beyond threshold value. However, increasing RPM may introduce lateral vibration such as backward and forward whirling [21].

2.6 Downhole Sensor Sub Background

Downhole vibration monitoring is very important in oil well drilling operation to avoid drill bit, drillstring, MWD tools failure from induced vibration. Downhole vibration has brought the attention of researches in industry and academia to analyze and mitigate the unwanted downhole vibration occurring in different modes since long time back. Since then many researchers focused their investigation to develop downhole vibration monitoring tool.

Martin *et al.* [22] presented an interim report on design, modeling and laboratory testing of the Drilling Vibration Monitoring & Control System (DVMCS), which has the ability to measure and monitor downhole drilling environments. In the report they claimed a method was developed to quantify the various vibration modes directly. The sensor sub consists of four accelerometers and a magnetometer. Three of the accelerometers are mounted radially 120 degrees from each other. The fourth accelerometer is mounted in the

axial direction to measure the axial vibration only. A magnetometer is also mounted in one of the pockets in the sensor sub. As the accelerometer is mounted radially, it measures the centripetal acceleration which is directly related to the rotary speed. Stick slip, whirl, lateral vibration are also calculated from this centripetal acceleration. However, in drillstring all three mode of vibration (axial, lateral, and torsional) may occur at the same time. So measuring lateral and torsional vibration from the centripetal acceleration is not reliable. Figure 2.6 and 2.7 shows the sensor configuration and schematic of the DVMCS tool respectively.

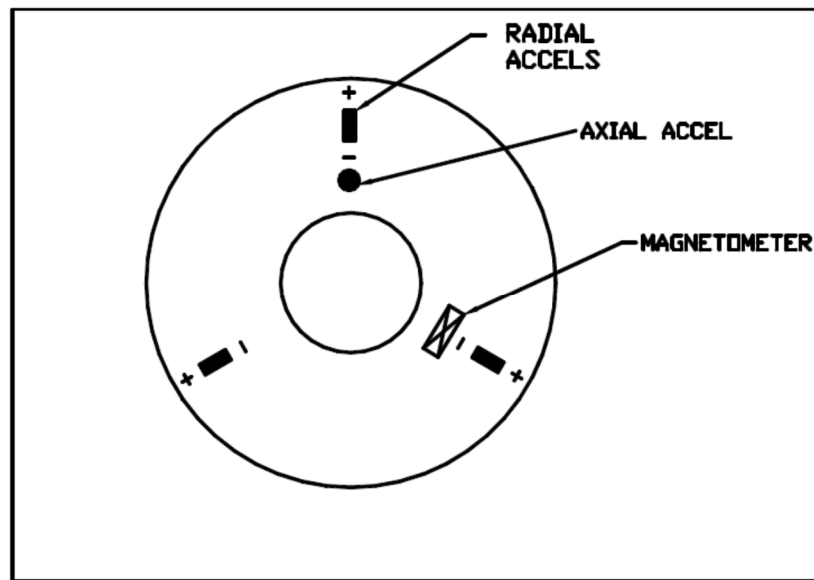


Figure 2.6 Sensor mounting configuration of DVMCS tool [22]

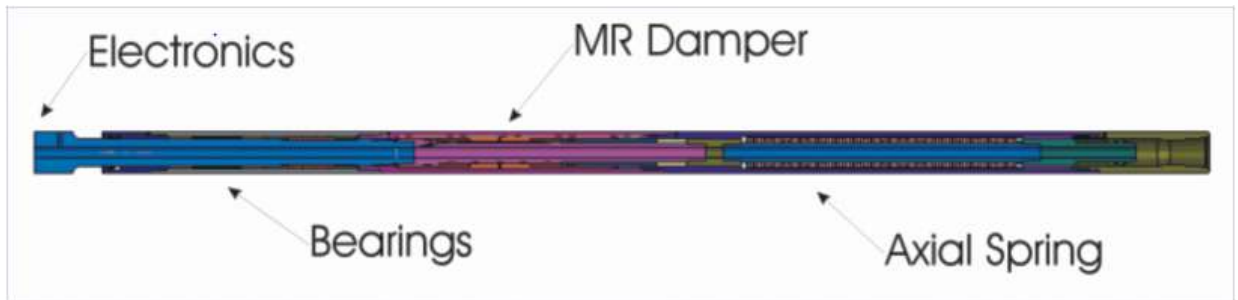


Figure 2.7 Schematic of DVMCS tool [22]

APS Technology's Vibration Memory Sub (VMS) [23] is a standalone downhole tool that measures and records axial, lateral and torsional downhole vibrations for post analysis when the tool is pulled out to the surface. The severity of downhole drilling shock and vibration, including stick slip and whirl can be assessed by using VMS tool and the data can be correlated to drilling events and equipment performance or failure. Two accelerometers and one magnetometer are used in this tool to measure the vibration and rotation. Measurements are recorded by date and time for correlation with other data. The obtained data from VMS tool is used to characterize downhole conditions for future BHA planning, post well analysis of equipment failures. However, the sampling rate of this tool is very low. It can record the data every 4 seconds at the maximum processor speed. At the same time, this tool can store maximum 32MB of data. A VMS tool is shown in Figure 2.8.



Figure 2.8 VMS tool [23]

Paul *et al.* [24] developed a bit based data acquisition system which is an integrated battery powered dynamic behavior sensor and data acquisition module. This module is located in the shank of a hard rock PDC bit. The sensor or data acquisition system is designed in such a way that it can be implanted within an annular recess machined between the outer diameter and inner diameter of the bit shank. Three orthogonal accelerometers and three orthogonal magnetometers are used in this module. The electronics are implemented in a flex circuit board to reduce the number of wire connection failures. The flex-circuit board includes a high strength reinforced backbone which provides acceptable transmissibility of acceleration effects to the accelerometers. If needed this module can be programmed to monitor the accelerometer readings and record downhole data in a burst mode if threshold vibration condition is met. This in-bit module can record data at a high frequency of 250 Hz in the burst mode. However, this bit based data acquisition system can be used only in the bit shank. So this system module can capture data of in-bit or near bit vibration only but can't capture vibration in other part of the drillstring. Moreover, this module is designed for selected applications.

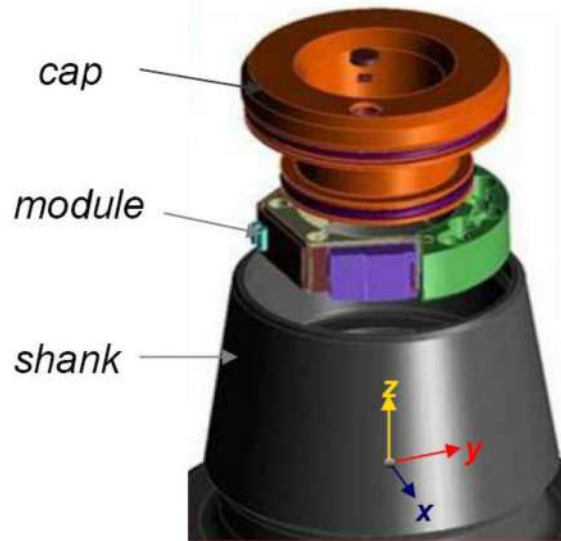


Figure 2.9 Assembly drawing of bit based data acquisition system [24]

Close *et al.* [25] used Exlog's (now part of Baker Hughes INTEQ) Down Hole Vibration Monitor (DHVM) to obtain accurate BHA vibration data while drilling. DHVM is an eight channel data acquisition digital recorder. It can store a maximum of 1 MB of downhole data. This downhole vibration measuring tool has three accelerometers placed orthogonally and one transverse magnetometer in the host collar. This tool has a real time clock which correlates time/depth with other parameters measured in the surface. The microprocessor is programmed to collect data one frame at a time. A pre-set time delay is defined in the program to store one frame of data into the storage device. This tool can be programmed to store data at a higher sampling rate. However, this DHVM tool is not a standalone tool, it is designed to be embodied within a MWD multi-sensor tool which acts

as a host of the DVHM system. Moreover, the storage capacity of this tool is very low which is not desirable for a long run drilling operation.

Zannoni *et al.* [26] developed a Drillstring Dynamics Sensor (DDS) tool to detect downhole dynamic behavior of drillstring such as bit bounce, whirl, stick slip and lateral BHA shocks. Drillstring Dynamics Sensor is designed to reduce harmful downhole vibration through more optimum bit selection, BHA design, well profile and operating parameters. The electronics and sensors of this tool are mounted on the insert of a MWD gamma ray detector. Total three accelerometers are used in the DDS tool and are located at a distance of 21.6 inches from the pin end connection of Gamma Ray Sub. The accelerometers can measure up to ± 200 g acceleration with a frequency response of 0 – 2300 Hz and resolution of 0.2 g. Signals from each accelerometer are conditioned using three different methods – average, peak and instantaneous. Average measurement has a range of 0 – 45 g with resolution of 0.2 g and data can be recorded at a variable sample period of 4 – 120 seconds. Peak measurement has a range of 0 – 200 g with resolution of 1g and data can be recorded at a variable sample period of 4 – 120 seconds. And instantaneous measurement has a range from ± 20 g to ± 200 g with a corresponding resolution from 0.2 g to 1 g and the data can be sampled at 500 Hz to 2000 Hz. However, this DDS tool has a memory storage capacity of 512KB which is cannot store data for a long operation. This tool didn't use any magnetometer to measure the rotary speed. They used the acceleration data to calculate rotary speed which could be inaccurate. Finally, the resolution of the accelerometers are very low for downhole vibration measurement.

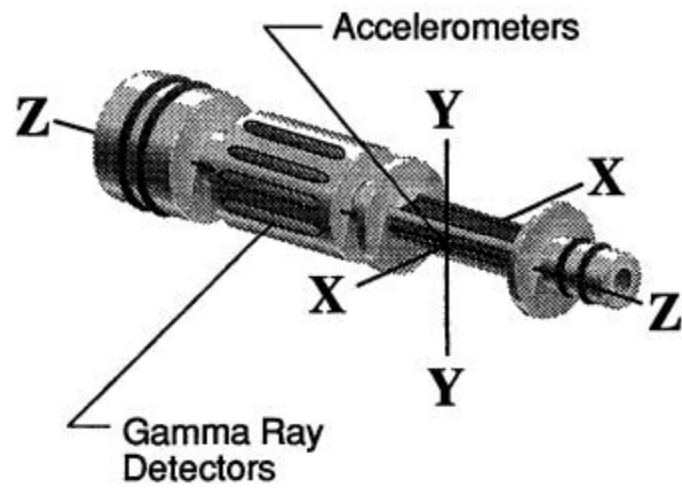


Figure 2.10 Downhole Dynamics Sensor layout [26]

3 CHAPTER 3:

DOWNHOLE SENSOR SUB

3.1 Introduction

It is very important to study downhole vibration in oil-well drilling operations. Vibration is a dominant factor for downhole tool failure. Uncontrolled drillstring vibration causes hole damage, bit damage and other downhole tool failure used in the drilling operations. To prevent downhole drilling equipment damage, it is important to know downhole dynamic conditions so drilling parameters can be modified to mitigate any harmful downhole vibration. A vibration monitoring downhole sensor sub is developed in Advanced Drilling Laboratory to study the downhole dynamics for field trial.

3.2 Mechanical Design

The downhole vibration measurement tool which is also known as downhole sensor sub is designed and developed in Advanced Drilling Laboratory at the Memorial University of Newfoundland. The mechanical part of the sensor sub is designed by Rana [27] using SolidWorks and fabricated in the machine shop of Memorial University. The sensor sub consists of one central hub, one outer shell, one sensor part, two API connections – one at the bottom and another on top of the central hub. Figure 3.1 shows different components of the downhole sensor sub.

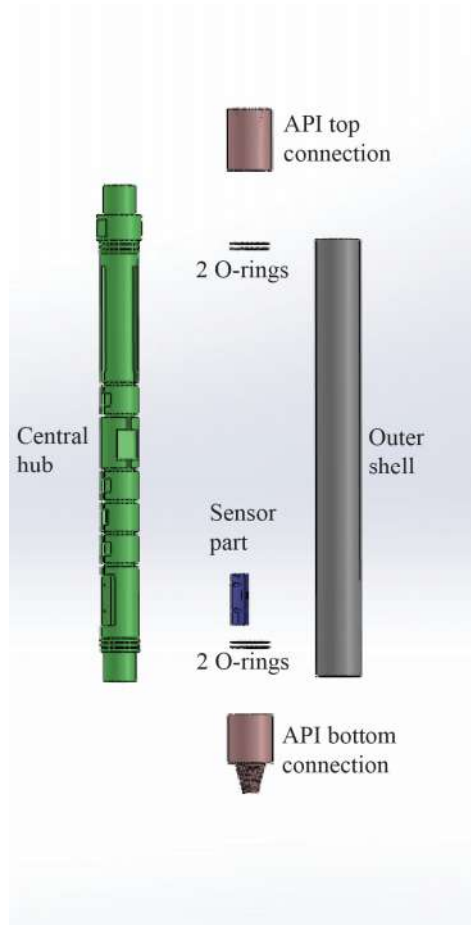


Figure 3.1 Mechanical design of downhole sensor sub [27]

The central hub has the groove for power supply, connections, microcontrollers, sensor part. This central hub is made of aluminium alloy 7075, which is a very high strength material used for highly stressed structural parts. Aluminium alloy 7075 is used as one magnetic sensor is used in the sensor part which is attached to the central hub and the tool had to withstand a large weight on bit (WOB) when heavy drill pipes are used. The sensor part is also made of aluminium alloy 7075 which contains the accelerometers and magnetometer. This sensor part is connected to the central hub with screws. All the sensors and electronics are covered in a non-conductive silicone to keep the sensors and electronics in place and reduce the effect from vibration as well. The outer shell protects the central hub and all the electronics and their connections. This outer shell is made of aluminium alloy 6061. There are 2 O-rings on each end of the central hub. These O-rings help to seal the gap between central hub and outer shell. The size of the O-rings is 70 BUNA, Size-240. Two API connections – one at bottom and other on top both has $\frac{3}{4}$ IF (Internal Flush) fitting. Once all the electronics go operational, the central hub is inserted in the outer shell and then the API connections are screwed and sensor sub is ready to be attached with the drill pipes for drilling operation. A detailed view of the central hub is shown in Figure 3.2. The author has contributed in developing the downhole sensor sub by designing the electrical circuit, power supply unit and selecting the proper electronics which are described in section 3.3 and 3.4.

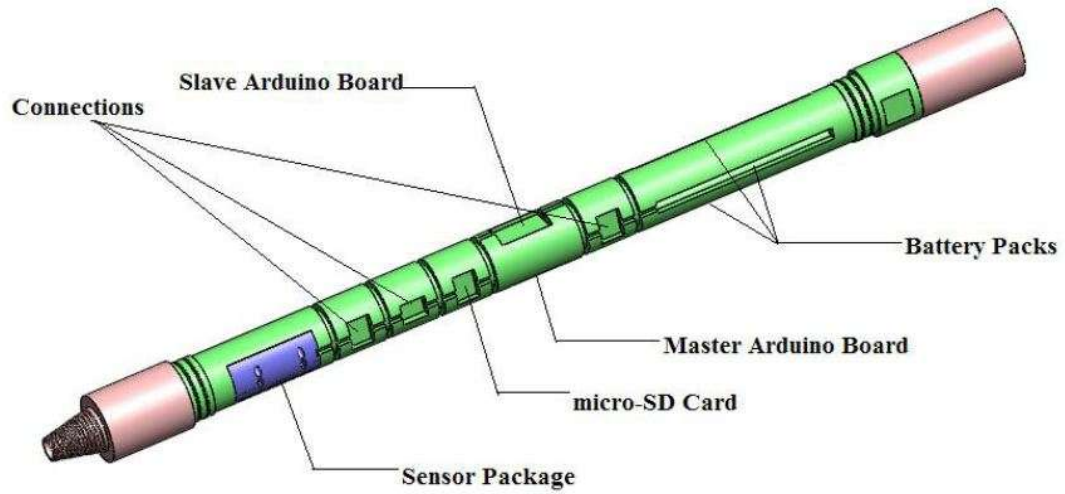


Figure 3.2 Detail view of the central hub [27]

3.3 Electrical Design

Electrical connection design for the downhole sensor sub is quite compact due to the space limitation in central hub. At the same time, the circuit is designed in such a way that any electrical component can be replaced easily if the component is broken. Considering the space limitation and easy replacement, the developed electronics connection diagram is shown in Figure 3.3. In this figure A1, A2, A3 are the accelerometers, M is the magnetometer, SD is data storage device (microSD memory card), Arduino M represents the master microcontroller, Arduino S represents the slave microcontroller and C1, C2, C3, C4, C5, C6, C7 are different connectors. Power is supplied to the slave microcontroller. All the sensors are connected with the master microcontroller and the data storage device is connected to the slave microcontroller.

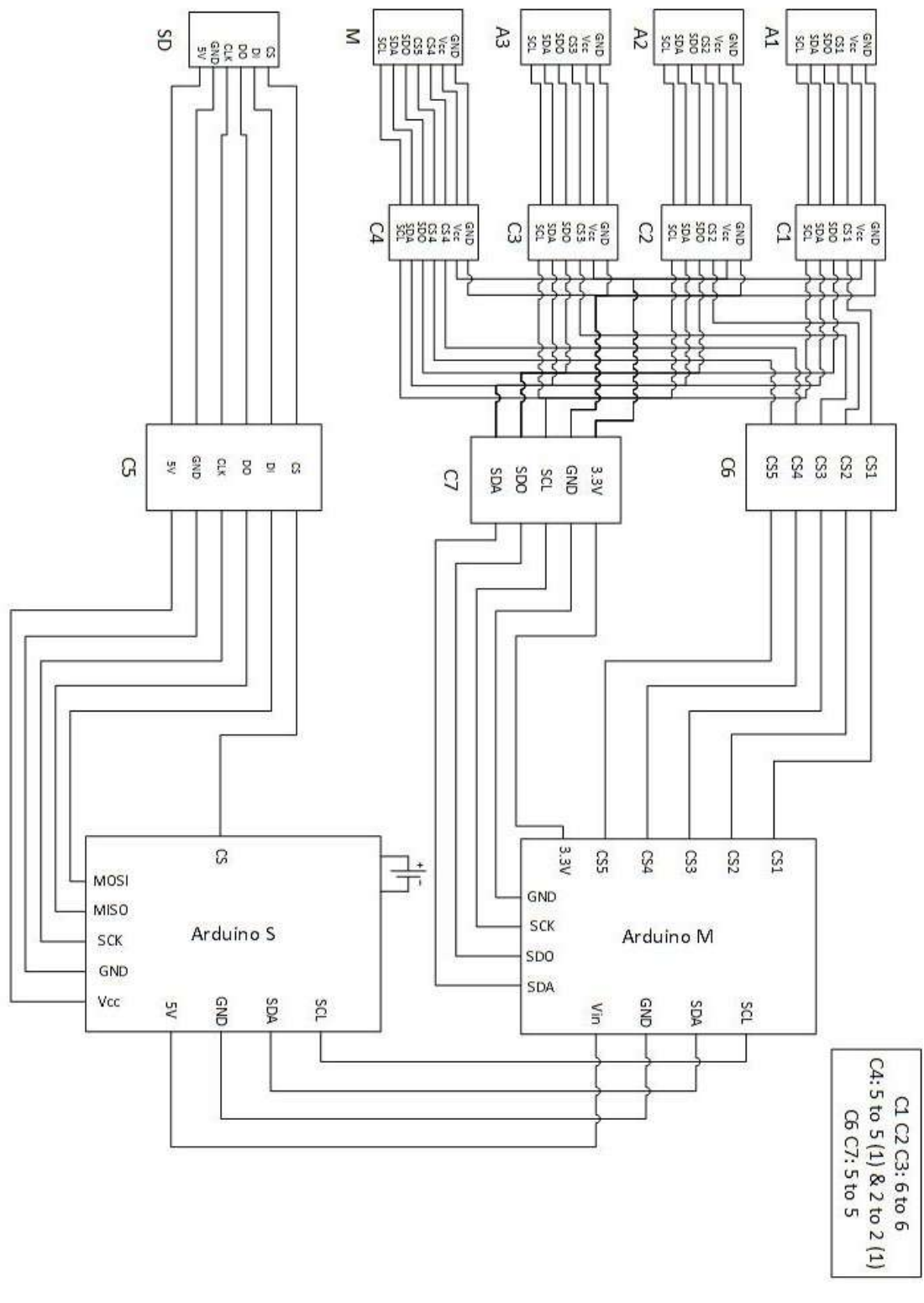


Figure 3.3 Circuit diagram of the electronics

As the sensor sub is going downhole for a long time during drilling operation, a reliable power supply is needed to provide continuous power to the system. The sensor sub is designed to accommodate three battery packs. Each battery pack can provide $9V$ and three of them are connected in parallel as shown in Figure 3.4. In each battery pack six $1.5V$ AA batteries (in series connection) with high density core which has a capacity of 2600 mAh (x6) each are used to provide uninterrupted power to the microcontrollers, sensors and data storage unit. Electrically conductive epoxy is used in between the batteries to avoid any kind of loss of contact among them during severe downhole vibration. Each battery pack is encapsulated in a heat shrink tube to increase the rigidity of the battery pack. Finally, foam is used in the power supply slots in central hub of the sensor sub, so that it can act as a damper to the battery packs and absorb the vibration during drilling operation.

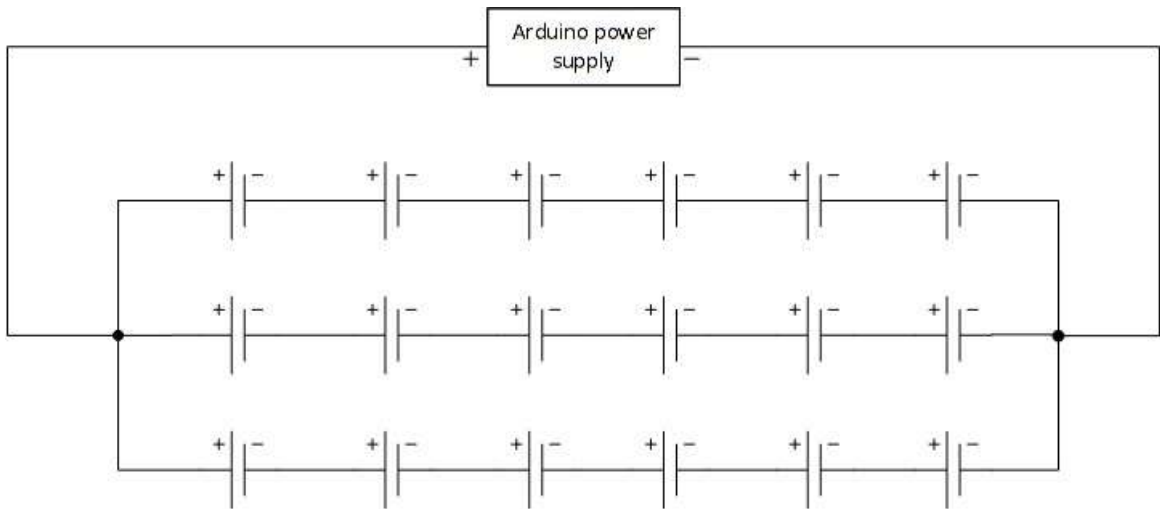


Figure 3.4 Electrical power supply to the electronics

3.4 Electronics

Electronics used in the downhole sensor sub are –

- Three ADXL345 accelerometers with breakout board
- One HMC5983 magnetometer with evaluation board
- Two Arduino Leonardo microcontroller board
- One microSD card breakout board with microSD card

3.4.1 ADXL345 Accelerometers

ADXL345 is a small, thin, low power, 3-axis MEMS accelerometer with high resolution measurement. It can measure acceleration from $\pm 2\text{ g}$ to $\pm 16\text{ g}$ with very high resolution of 3.9 mg . This sensor is accessible through either a SPI (3- or 4-wire) or I2C digital interface. It can measure static acceleration of gravity in tilt-sensing applications, as well as dynamic acceleration resulting from motion or shock. This accelerometer consumes very low power– $40\text{ }\mu\text{A}$ in measurement mode and $0.1\text{ }\mu\text{A}$ in standby mode at supply voltage of 2.5 V . The supply voltage for this accelerometer is $2.0\text{ V} - 3.6\text{ V}$. [28]

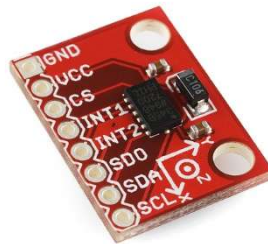


Figure 3.5 ADXL345 accelerometer [28]

3.4.2 HMC5983 Magnetometer

Honeywell HMC5983 is a three-axis integrated circuit magnetometer. It is designed for low-field magnetic sensing for applications with high-resolution measurement. With a 12-bit ADC this sensor can measure 1° to 2° compass heading accurately. This high accuracy sensor is accessible through either a SPI (3- or 4-wire) or I2C digital interface. This sensor can measure both the direction and the magnitude of magnetic fields, from milli-gauss to 8 gauss. This sensor consumes $2\ \mu A$ in standby mode and $100\ \mu A$ in measurement mode at supply voltage of $2.5V$. Typical supply voltage for this magnetometer is $2.5V$ but its operating range is $2.16V - 3.6V$. [29]



Figure 3.6 HMC5893 magnetometer [30]

3.4.3 Arduino Leonardo Microcontroller Board

Arduino Leonardo is a microcontroller board based on the ATmega32u4. It has 20 digital input/output pins. 7 of them can be used as PWM outputs and 12 as analog inputs. It has a micro USB connection, a power jack, an ICSP header, and a reset button. It contains everything needed to support the microcontroller. The Arduino Leonardo can be powered via the micro USB connection or with an external power supply. The board can operate on an external supply of $6V$ to $20V$. If supplied voltage is less than $7V$, the $5V$ pin will not be

able to supply $5V$ and the board may become unstable. If more than $12V$ is supplied, the voltage regulator may overheat and damage the board. The recommended range is $7V$ to $12V$. It can provide upto 50 mA DC current. Arduino Leonardo supports both I2C and SPI communication. [31]

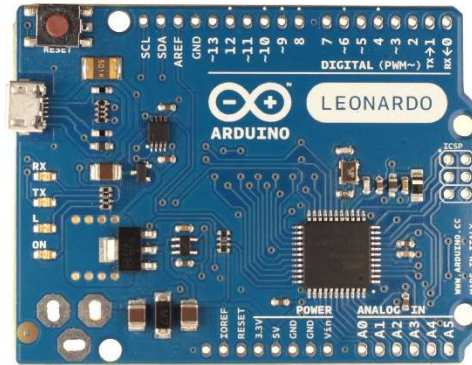


Figure 3.7 Arduino leonardo [31]

3.4.4 MicroSD Card Breakout Board

This microSD breakout board from adafruit has onboard $5V$ to $3V$ regulator so both $3V$ and $5V$ system can be used and it can provide 150 mA current to microSD cards. This breakout board can read and write faster into and from the microSD card. It has an easy push-push socket to lock the microSD card. [32]

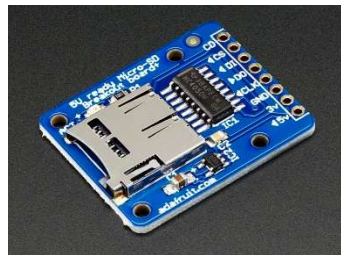


Figure 3.8 MicroSD breakout board [32]

The downhole sensor sub developed by Advanced Drilling Laboratory was used in a field trial. Data obtained from the field trial is processed and analyzed which is presented in the next chapter.

4 CHAPTER 4:

FIELD TRIAL DATA INTERPRETATION

4.1 Introduction

In this chapter a method has been developed to interpret the field data which has been collected using the Downhole Measurement Tool (Sensor Sub) [33] developed in Advanced Drilling Laboratory. A description of the Sensor Sub has been given in Chapter 3.

4.2 Field Trial

The field trial was conducted under Advanced Drilling Laboratory during fall 2014. The location of the field trial was Greenslades Construction Quarry B site [34] on Red Bridge Road, Kelligrews, CBS, NL, Canada. An aerial view of the drilling site is shown in Figure 4.1. Both PDC and RC bits were used during the drilling operation.

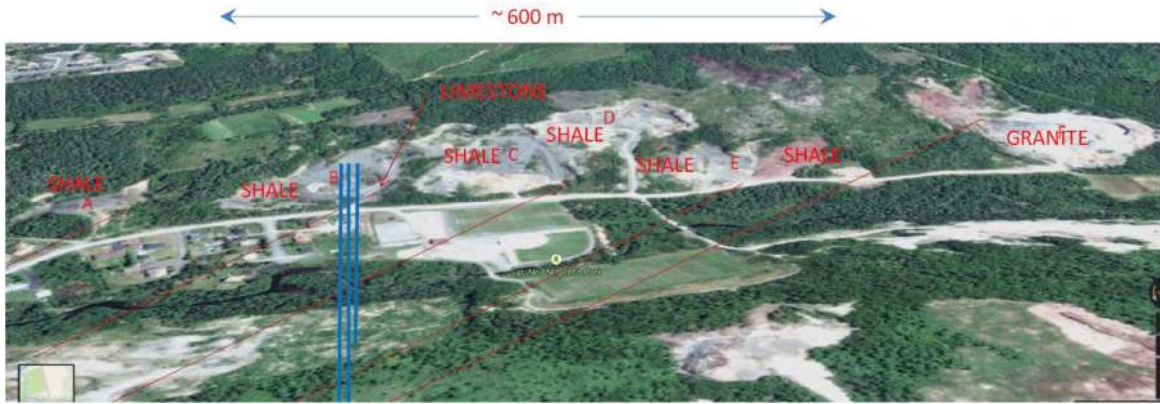


Figure 4.1 Aerial view of Greenslades Construction Quarry B site [34]

4.3 Data Calculation

The vibration monitoring sensor sub is capable of capturing downhole vibration and rotation data. Captured data are then adjusted according to the sensor location and their axes. The accelerometers gives acceleration data in “g” and the magnetic sensor’s rotation data is in radians. The equations for acceleration developed by Gao [35] are corrected according to sensor mounting in the sensor sub. The sensor part and the location of the sensors in the sensor part are shown in Figure 4.2. Each accelerometer has three different axis – x, y and z. These acceleration values in different axes are used to calculate three different modes of vibration – axial, torsional and lateral. Adjusted equations for axial, torsional and lateral vibration are given from equation 4.1 to 4.9. For the axial vibration 1 g is added or subtracted from the recorded data for gravitational acceleration adjustment according to the sensor location shown in Figure 4.2. For lateral and torsional vibration the acceleration components are adjusted according to the direction of the accelerometer components which are presented in the equation 4.6 to 4.9.

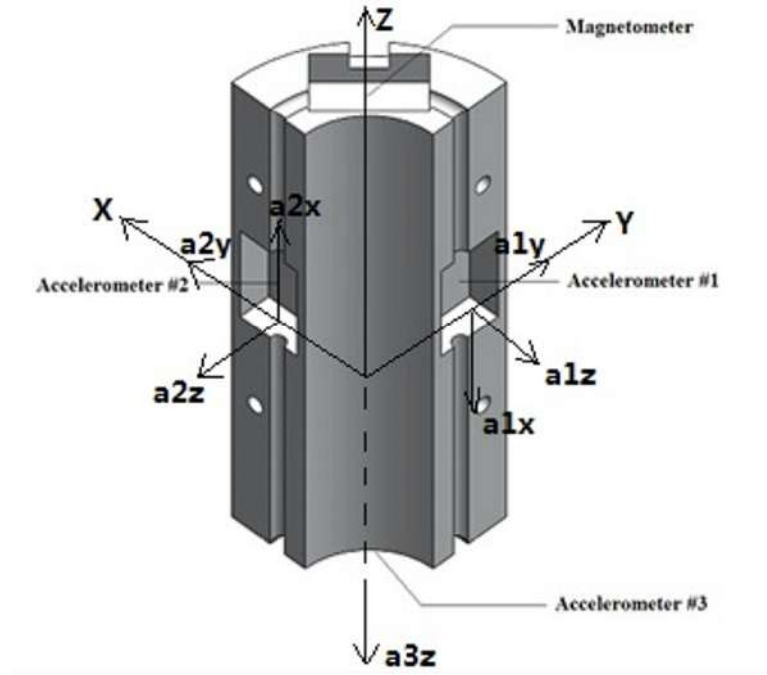


Figure 4.2 Sensor package layout

Axial

$$a1_{x'} = a1_x + 1g \quad (4.1)$$

$$a2_{x'} = a2_x - 1g \quad (4.2)$$

$$a3_{z'} = a3_z + 1g \quad (4.3)$$

$$A_{axial} = \frac{a1_{x'} + a2_{x'}}{2} \quad (4.4)$$

$$A_{shock} = a3_{z'} \quad (4.5)$$

In the equations the numbers 1, 2, 3 represents the accelerometer 1, accelerometer 2 and accelerometer 3 respectively. Among these accelerometer 1 and 2 are the low range

accelerometer and accelerometer 3 is the high range accelerometer. The low range accelerometer can capture up to 4 g acceleration in three different axes while the high range accelerometer can capture 16 g acceleration. 1 g is the correction factor and that has been added or subtracted according to the sensor location in the downhole measurement tool. Axial acceleration can be calculated by equation 4.1-4.4. While doing the data processing for axial acceleration the data acquired from 4 g range accelerometer has been used in the first place. If the acquired data exceeds 4 g acceleration then data recorded by 16 g accelerometer has been used for calculation. If any shock exists in the captured data, equation 4.5 can be used to measure the shock where the high range accelerometer data is used [35]. Lateral acceleration is calculated following equation 4.6 to 4.8. Alx and Aly are the components of lateral acceleration $A_{lateral}$ in x-axis and y-axis respectively which are calculated from the accelerometer components according to sensor orientation shown in Fig 4.2. Torsional acceleration is calculated following equation 4.9. Lateral and torsional acceleration can be calculated using the low range accelerometer data only [35].

Lateral

$$Alx = \frac{-a1_z - a2_z + a2_y - a1_y}{2} \quad (4.6)$$

$$Aly = \frac{-a1_z - a2_z - a2_y + a1_y}{2} \quad (4.7)$$

$$A_{lateral} = \sqrt{Alx^2 + Aly^2} \quad (4.8)$$

Torsional

$$A_{torsional} = \frac{-a1_z - a2_y + a2_z + a1_y}{2} \quad (4.9)$$

The magnetometer gives the data in radians. Rotary speed of the drillstring can be calculated using magnetometer data. RPM is calculated from the magnetic sensor data following equations 4.10 and 4.11 where ω is the angular velocity in *rad/s*.

RPM (magnetometer)

$$\omega = \frac{\Delta\theta}{\Delta t} \quad (4.10)$$

$$rpm = \frac{\omega * 60}{2\pi} \quad (4.11)$$

4.4 Signal Processing

Signal processing accomplishes the transformation between the time domain and the frequency domain. Therefore, time-based data from a transducer can be converted to the frequency domain. This allows for the identification of the natural frequencies from the system data. There are three types of signals – periodic, aperiodic and random. A random signal is neither periodic nor deterministic, but it does have statistical property.

4.4.1 Filtering

Filtering out the noise from any sensor data is an important first step while working with any real time monitoring system. It is one of the important roles in data acquisition systems. Filters are used to remove unwanted frequencies from a signal and minimize artifacts or noise. There are two basic use of filter: one is signal separation and the other one is signal restoration. Signal separation is needed when another signal or noise interferes the main signal. Signal restoration is used when a signal is distorted in some way. There are some important terms which are important to understand the basics of filtering. These terms apply to all types of filters.

Cut-Off Frequency (f_c): The frequency which defines the limits of the filter range is known as cut off frequency. It is the desirable cut off point for the filter. It is also known as corner frequency.

Stop Band: The range of frequencies that is filtered out.

Pass Band: The range of frequencies which is let through and recorded.

Transition Band: The range of frequencies between the pass band and the stop band where the gain of the filter varies with frequency.

Figure 4.3 demonstrates the filter bands for a low pass filter.

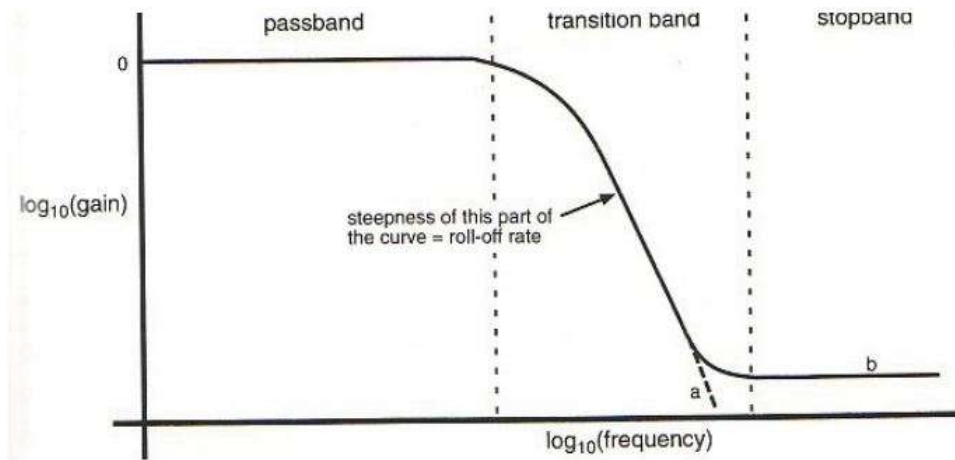


Figure 4.3 Filter bands [37]

High Pass Filter (HPF) and Low Pass Filter (LPF) are the most commonly used filters in signal processing.

Low Pass Filter: A low-pass filter allows signal frequencies below the cut-off frequency to pass and eliminates the frequencies above the cut-off frequency.

High Pass Filters: A high-pass filter allows frequencies higher than the cut-off frequency to pass and filter outs the low frequency contents from the signal.

There is another filter called *Band Pass Filter* (BPF), which is a combination high and low pass filter. A Band Pass Filter is used to pass a larger range of frequencies. Frequencies on either side of this band are not allowed to pass. The other type of filter is *Band Stop Filter* (BSP). This is the complement of Band Pass Filter. This type of filter blocks a certain range of frequencies and allows frequencies either side of this range to be passed.

A useful comparison between different types of filter effect is shown in Figure 4.4.

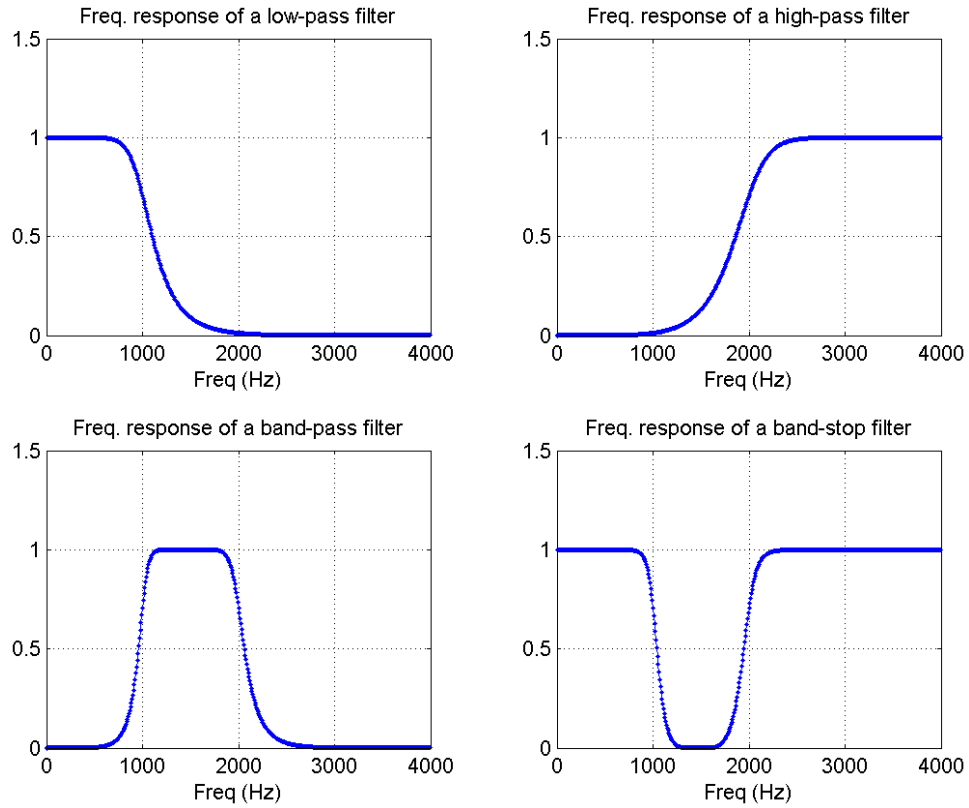


Figure 4.4 Different types of filter response [38]

In this thesis work a low pass filter with a cut off frequency of 10 Hz is used to filter out the high frequency noise from the processed data and the results are presented later in this chapter.

4.4.1.1 Moving Average Filter

In signal processing the moving average is one of the most commonly used filters [39]. It is very simple and easy to understand and use. Beside its simplicity, the moving average filter is optimal for a common task, which is- reducing random noise while retaining a sharp

step response. This characteristic of this filter makes it the premier filter for time domain encoded signals. Gaussian, Blackman, and multiple pass moving average filter are quite similar to the moving average filter. Performance of these filters are slightly better in case of the frequency domain but these need increased amount of computation time than the moving average filter [39]. The moving average filter is very good for many applications. It can reduce random noise while keeping the sharpest step response. An example of moving average filter is shown in Figures 4.5 – 4.7. The original signal in Figure 4.5 is filtered with 11 and 51 point moving average filters, and the results are shown in Figure 4.6 and 4.7 respectively. As the number of points in the filter increases, the noise becomes lower. In this thesis work moving average filter is used in 20-sim software environment to take out the mean value of the acceleration, velocity and displacement.

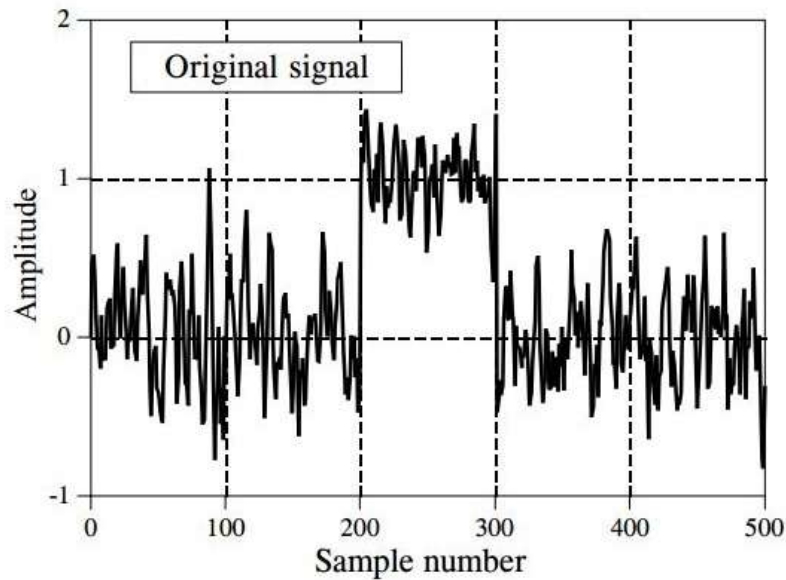


Figure 4.5 Example of a moving average filter (original signal) [39]

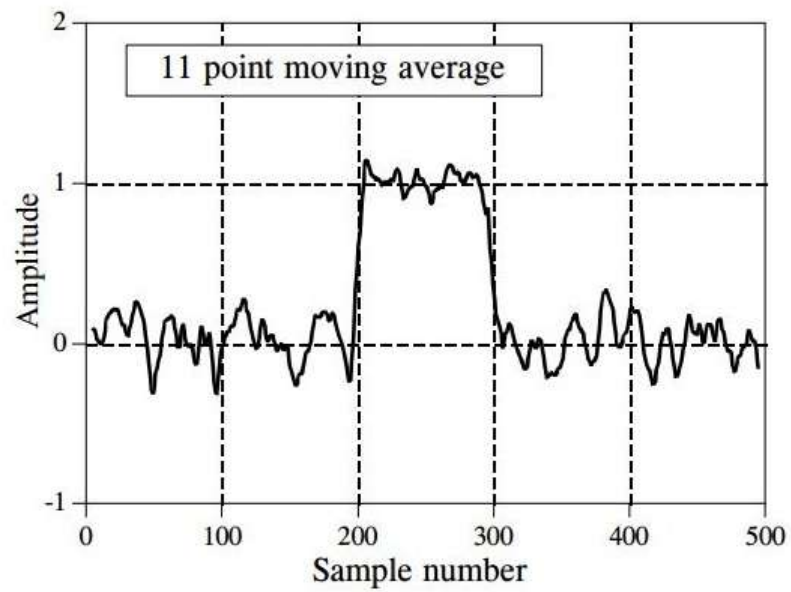


Figure 4.6 Example of a moving average filter (after noise reduction) [39]

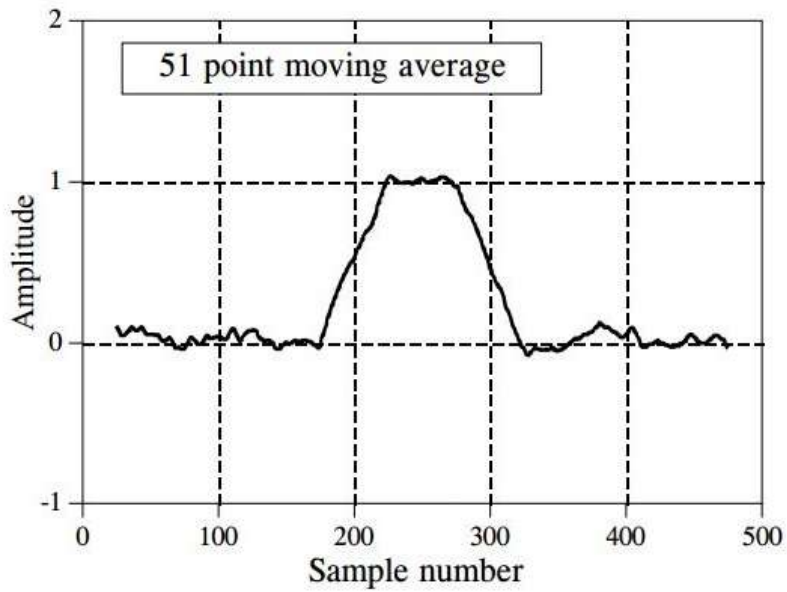


Figure 4.7 Example of a moving average filter (after noise reduction) [39]

4.4.1.1.1 Procedure

Data recorded from the field trial [34] are the raw data. These data are transformed into useable and understandable data by using the adjusted equations from the formulas developed by Gao [35] and the moving average filters. Moving average submodel is used in 20-sim from 20-sim signal processing library. In this simulation environment acceleration data file is given as input and the submodel has integrated time interval variable. Different time interval is used to run the simulation and from the simulation results it has been found that for the time interval of 0.06 s (3 times of the 50 Hz sampling frequency) gives the best result. With a bigger time interval the signal stays noisy (as same as the raw data) and with a smaller time interval the resultant after demeaning becomes close to zero. Following the trial and error method it has been found that 0.06 s gives the best result. First, from the source acceleration file the moving average is demeaned and then after integrating, the resultant gives the corresponding velocity. Same procedure is done for the velocity component and the resultant gives the corresponding displacement after integrating again. In calculation for the axial part there is only one acceleration, velocity and displacement component which is in the axial direction. But for the calculation for lateral part there are two components for each from which lateral motion or whirl can be identified.

i. Calculation Model for Axial Vibration

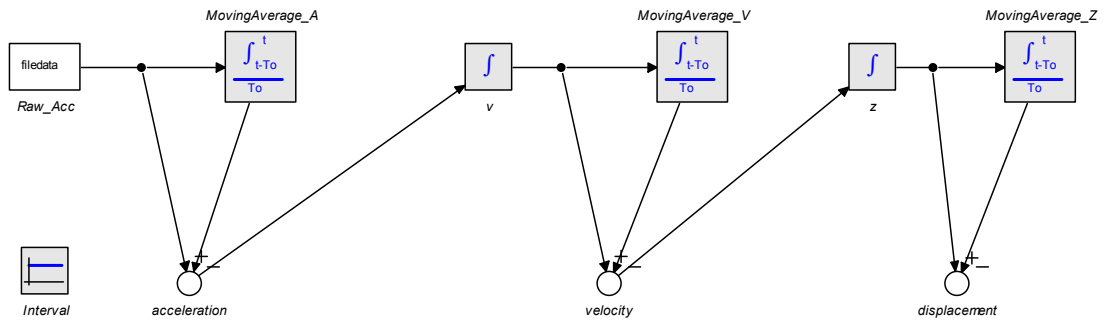


Figure 4.8 20-sim model for axial displacement calculation

ii. Calculation Model for Lateral Vibration

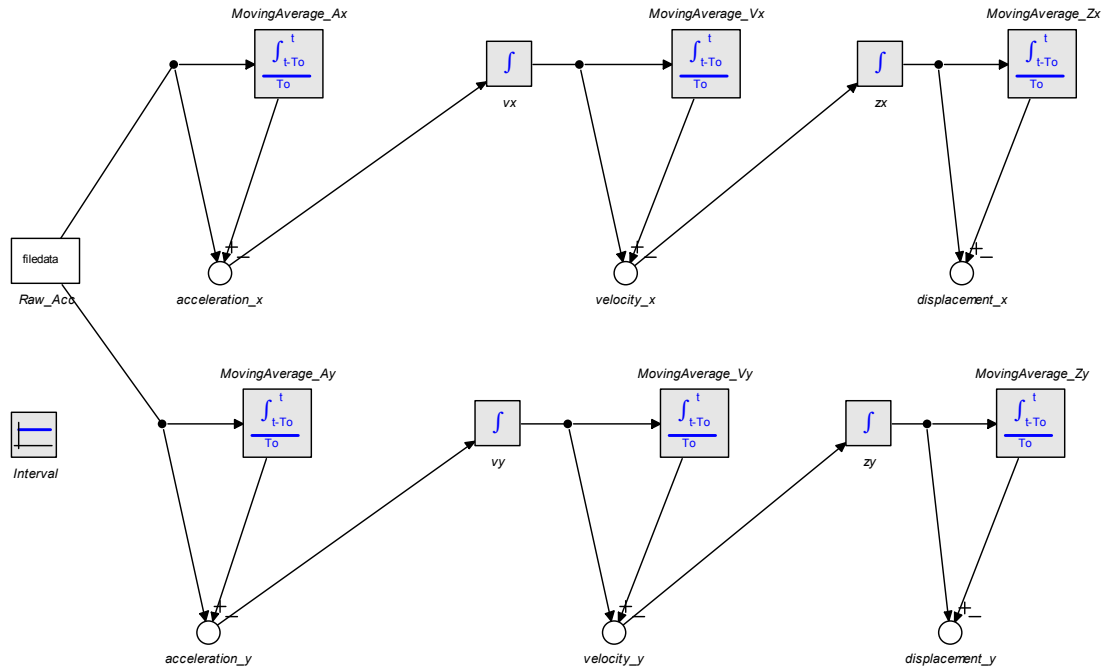


Figure 4.9 20-sim model for lateral displacement (whirl) calculation

iii. Calculation Model for Torsional Vibration

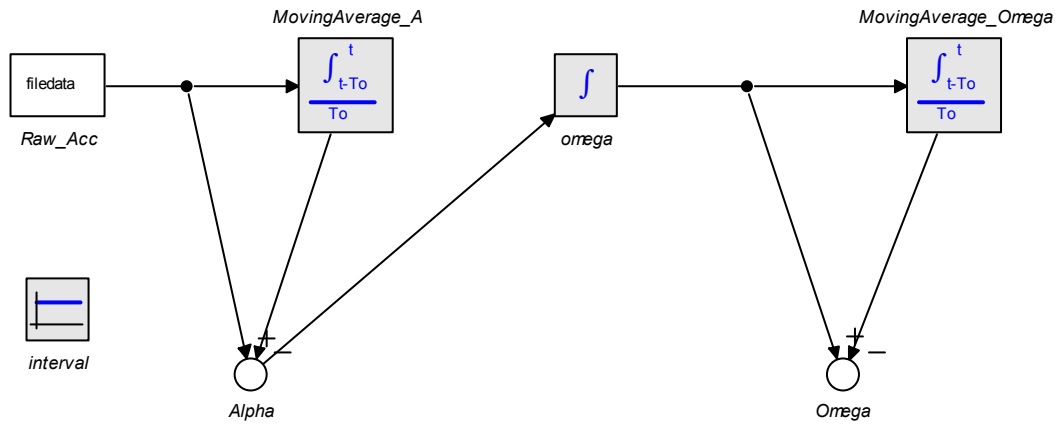


Figure 4.10 20-sim model for torsional acceleration calculation

In the torsional calculation model the acceleration is demeaned to find out the actual torsional acceleration of the system. Then angular acceleration is calculated by using the distance of the sensors from the center of the sensor sub which is 35.60 mm. Finally angular velocity is calculated by integrating the angular acceleration. While integrating an integration constant is used which is the rotary speed of corresponding depth measured in the field trial. Stick slip can be identified from the calculated angular velocity. Figure 4.8 – 4.10 shows the calculation model for axial, lateral and torsional using moving average filter.

4.4.1.1.2 Results

i. Axial Acceleration and Displacement

The results from axial displacement calculation model for different drilling depth with different bit type are shown from Figure 4.11 to Figure 4.18. Figure 4.11 – 4.14 represents the demeaned acceleration and displacement due to axial vibration where roller cone (RC) bit is used. For the RC bit when low weight on bit (WOB) is applied at drilling depth of 117-127 *ft*, axial displacement is found up to 6 *mm*. The applied WOB in this case is 35 *kN*, rate of penetration (ROP) is 0.85 *ft/min*. The formation in this depth is grey shale.

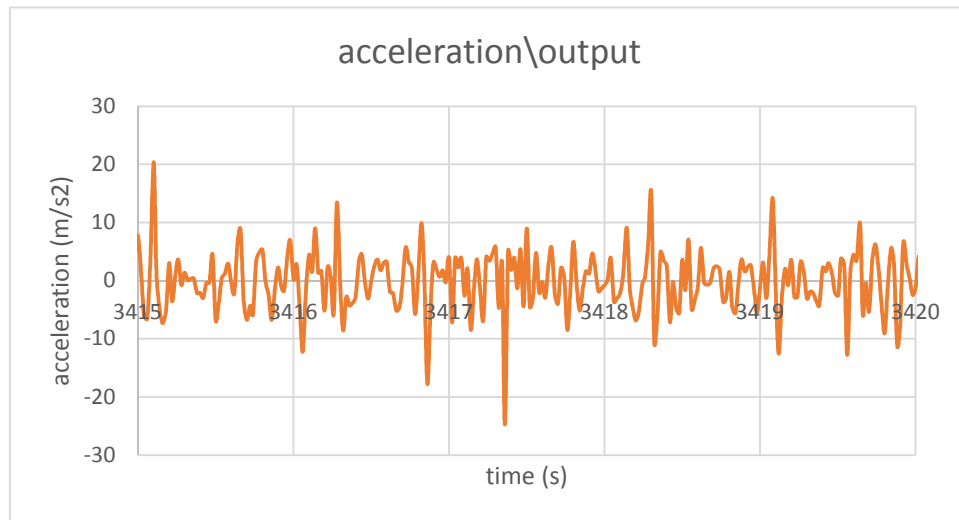


Figure 4.11 Demeaned axial acceleration using moving average filter

Depth: 117-127ft

WOB: 35kN

Bit type: RC

Formation: Grey shale

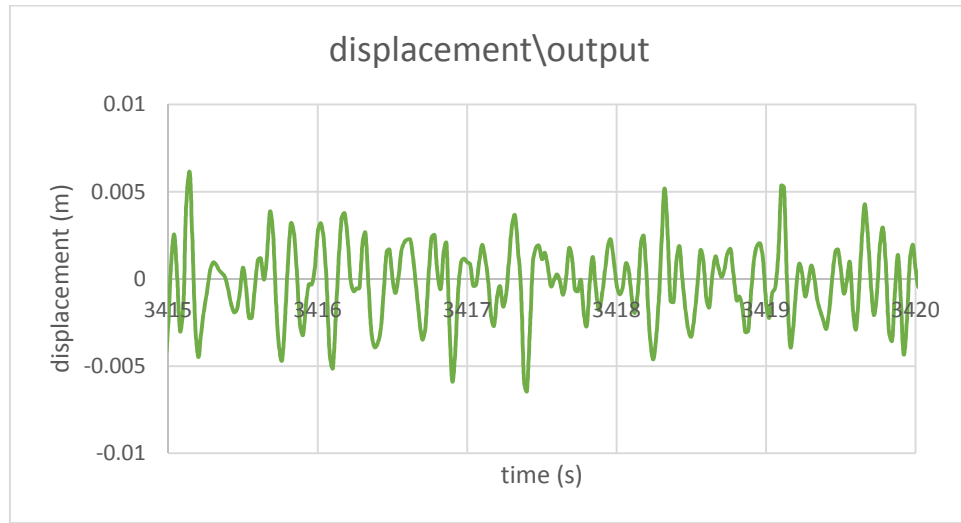


Figure 4.12 Demeaned axial displacement using moving average filter

Depth: 117-127ft

WOB: 35kN

Bit type: RC

Formation: Grey shale

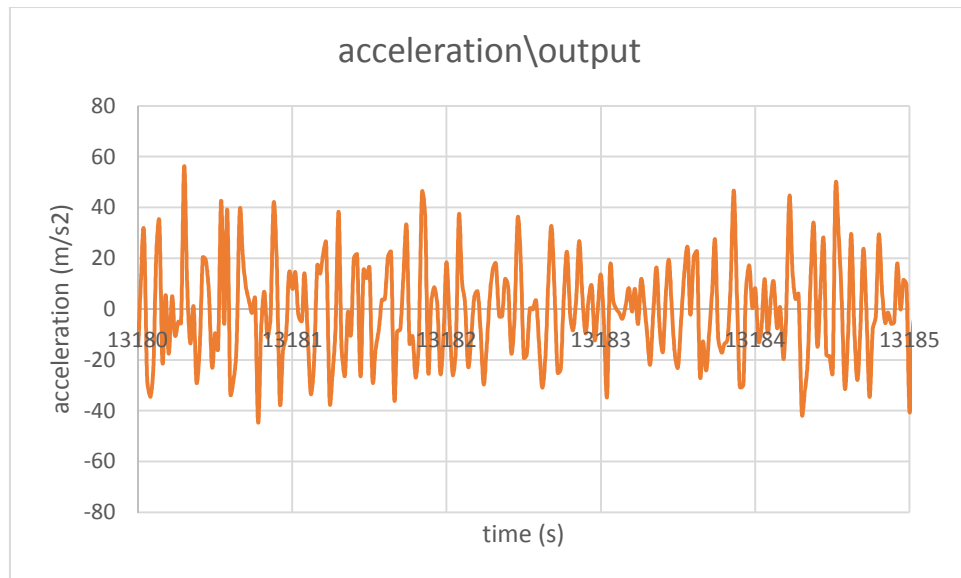


Figure 4.13 Demeaned axial acceleration using moving average filter

Depth: 217-227ft

WOB: 143kN

Bit type: RC

Formation: Red & Grey shale

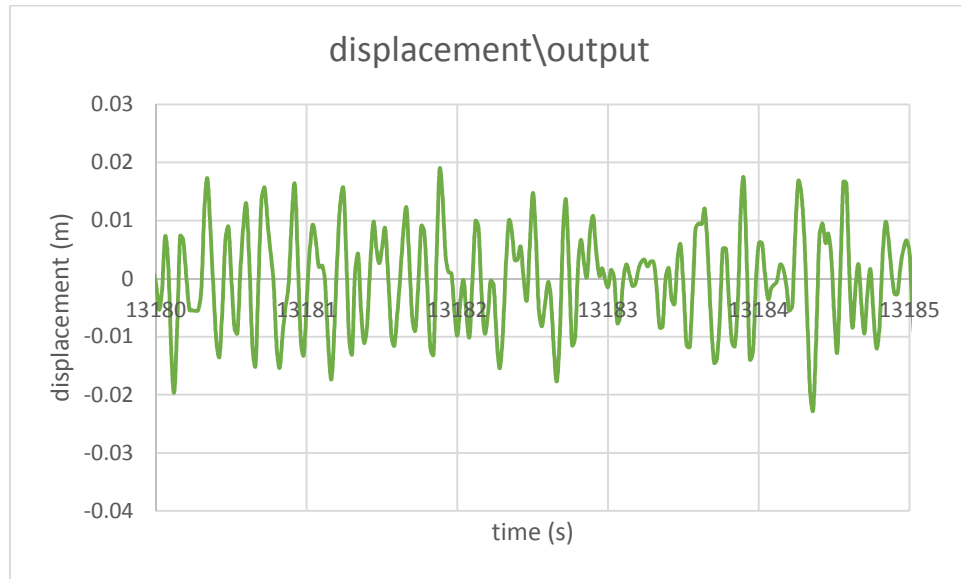


Figure 4.14 Demeaned axial displacement using moving average filter

Depth: 217-227ft WOB: 143kN Bit type: RC Formation: Red & Grey shale

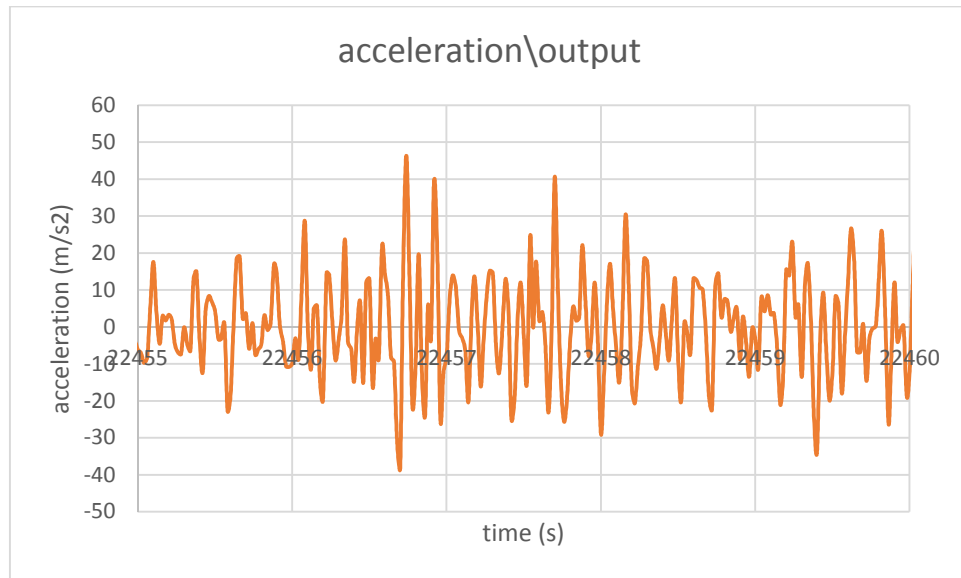


Figure 4.15 Demeaned axial acceleration using moving average filter

Depth: 227-237ft WOB: 137kN Bit type: PDC Formation: Red shale

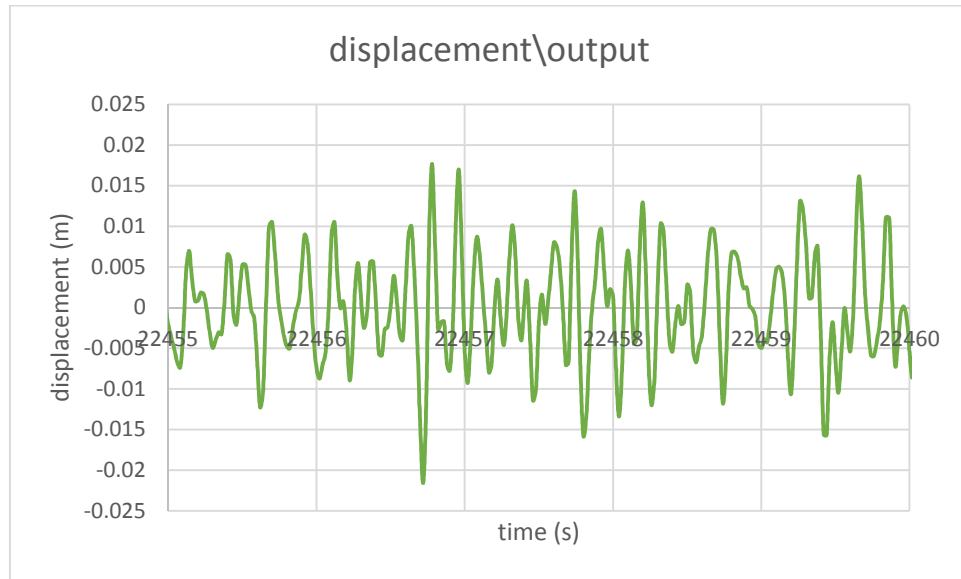


Figure 4.16 Demeaned axial displacement using moving average filter

Depth: 227-237ft

WOB: 137kN

Bit type: PDC

Formation: Red shale

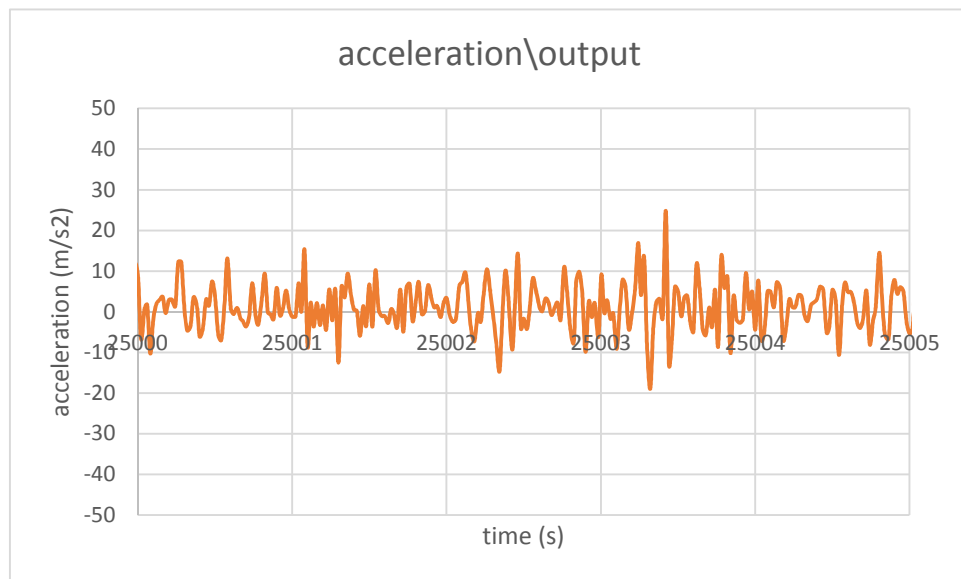


Figure 4.17 Demeaned axial acceleration using moving average filter

Depth: 257-267ft

WOB: 58kN

Bit type: PDC

Formation: Red shale

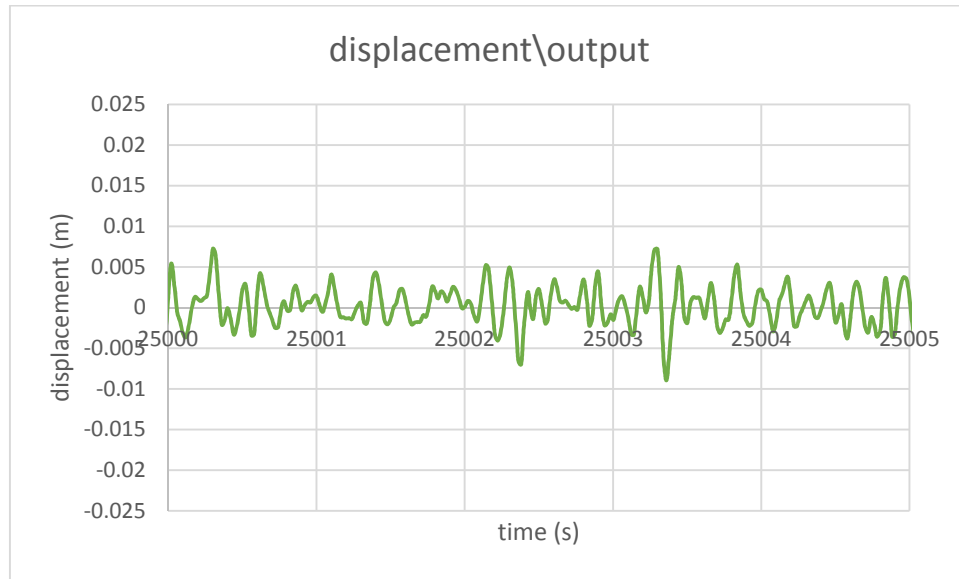


Figure 4.18 Demeaned axial displacement using moving average filter

Depth: 257-267ft

WOB: 58kN

Bit type: PDC

Formation: Red shale

At depth 217-227 *ft* where high WOB of 143 *kN* is applied, axial displacement is found up to 20mm and the ROP is 1.97 *ft/min*. Calculated acceleration and displacement for Polycrystalline Diamond Compact (PDC) bit is shown in Figure 4.15 – 4.18. At 227-237 *ft* depth when 137 *kN* WOB is applied, the displacement is found up to 20 *mm* and ROP is 1.58 *ft/min*. The formation in this depth is red shale. While low WOB is applied in depth of 257-267 *ft*, the axial displacement is found up to 8 *mm*. The ROP for this depth is 0.28 *ft/min* and the formation is red shale. For both cases while RC and PDC bits are used axial displacement is found higher when high WOB is applied and axial displacement is found lower when low WOB is applied.

ii. Lateral Acceleration

Lateral acceleration is calculated following the formulas explained in section 4.3 in this chapter and the results after using moving average filter are shown from Figure 4.19 to Figure 4.22. Analysis shows that when lower WOB is applied the lateral acceleration is lower and when higher WOB is applied the lateral acceleration is higher. This phenomena can be seen while using RC bit and PDC bit separately. When RC bit is used, the lateral acceleration is found up to 21.7 m/s^2 with 35 kN of WOB. With a higher WOB of 143 kN the lateral acceleration is found up to 61 m/s^2 . Similarly, when PDC bit is used with 58 kN and 148 kN WOB, the lateral acceleration is found 30.3 m/s^2 and 39 m/s^2 respectively.

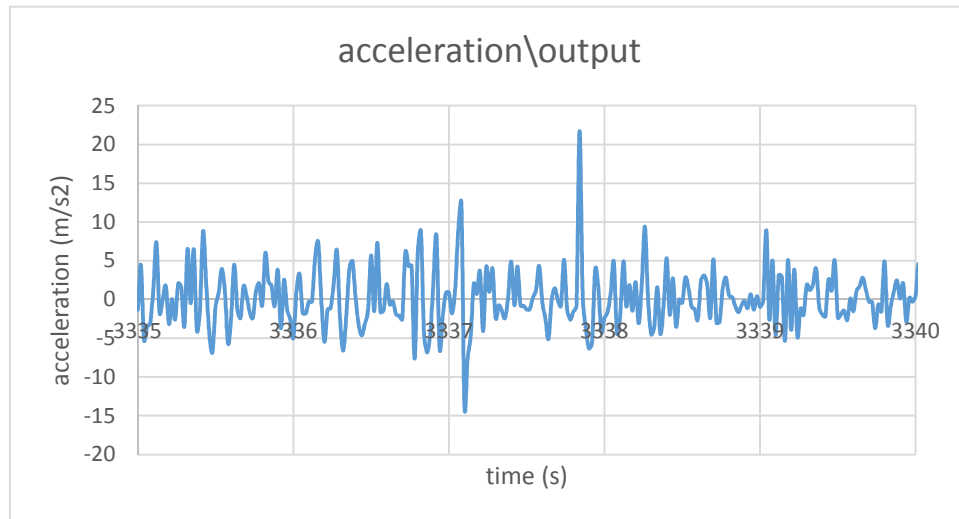


Figure 4.19 Demeaned lateral acceleration using moving average filter

Depth: 117-127ft WOB: 35kN Bit type: RC Formation: Grey shale

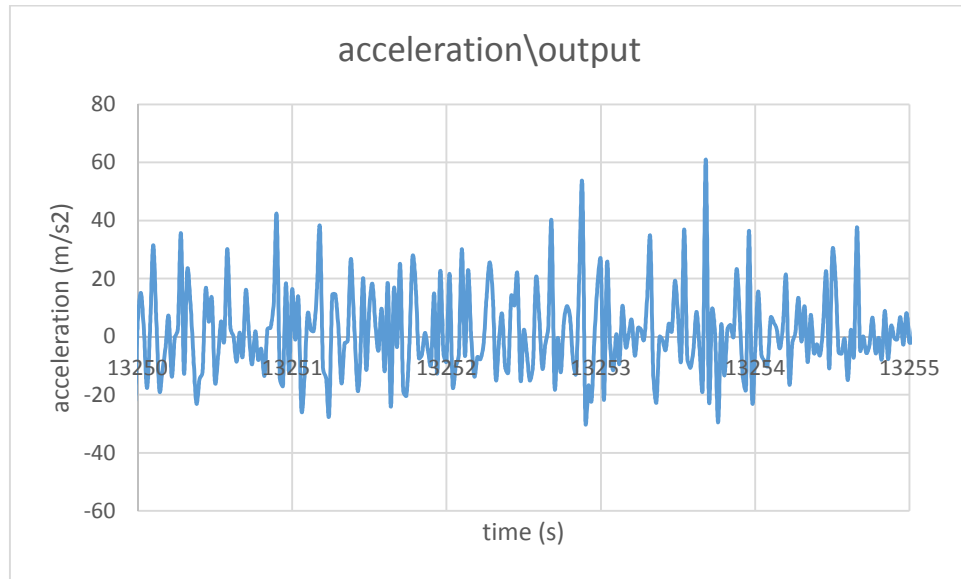


Figure 4.20 Demeaned lateral acceleration using moving average filter

Depth: 217-227ft WOB: 143kN Bit type: RC Formation: Red & few Grey shale

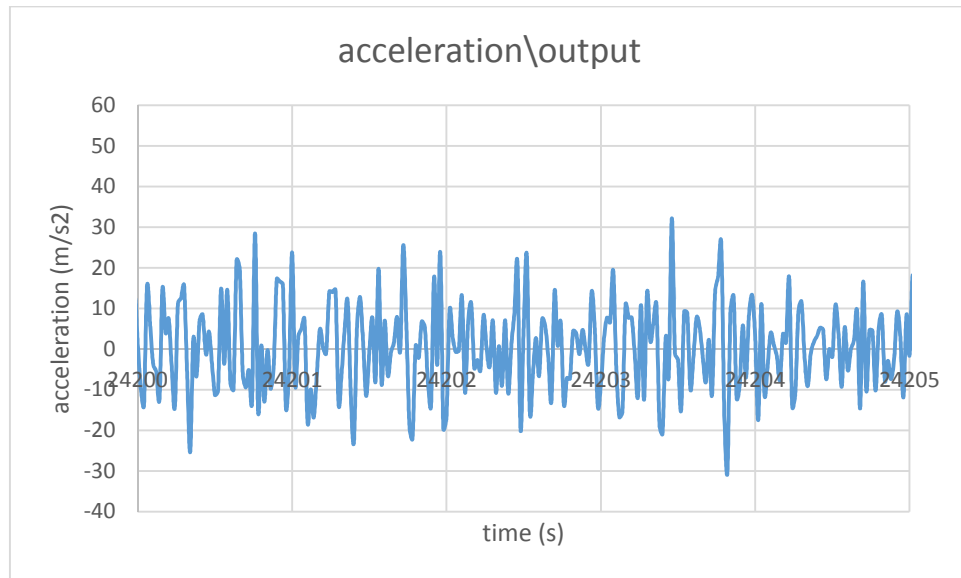


Figure 4.21 Demeaned lateral acceleration using moving average filter

Depth: 257-267ft WOB: 58kN Bit type: PDC Formation: Red shale

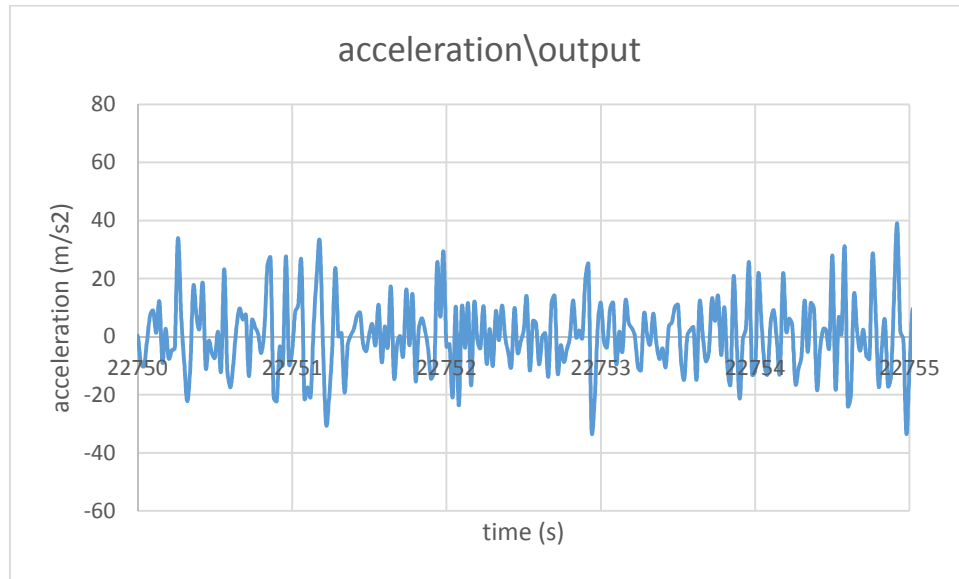


Figure 4.22 Demeaned lateral acceleration using moving average filter

Depth: 237-247ft WOB: 148kN Bit type: PDC Formation: Red shale

iii. Whirl

Whirl is calculated by integrating the lateral acceleration components twice. But before integrating the acceleration data coordinate transformation is needed. The acceleration data recorded from the accelerometers are in a reference frame which is rotating. To find out the whirl this data is transformed into a fixed coordinate frame by using the magnetometer data. Finally the transformed data is used to calculate the drillstring whirl. Figure 4.23 – 4.26 shows the drillstring whirl at different depth with different WOB. The diameter of the drill bit used is 6 inches and the diameter of the drillstring used is 4.5 inches. So the clearance between the wellbore and drillstring is 0.75 inch (19.05 mm). In the Figures 4.23 – 4.26 it can be seen that the displacement due to lateral acceleration is within the clearance value.

It can also be seen that with a lower WOB for both PDC and RC bits drillstring whirl is less than with higher WOB.

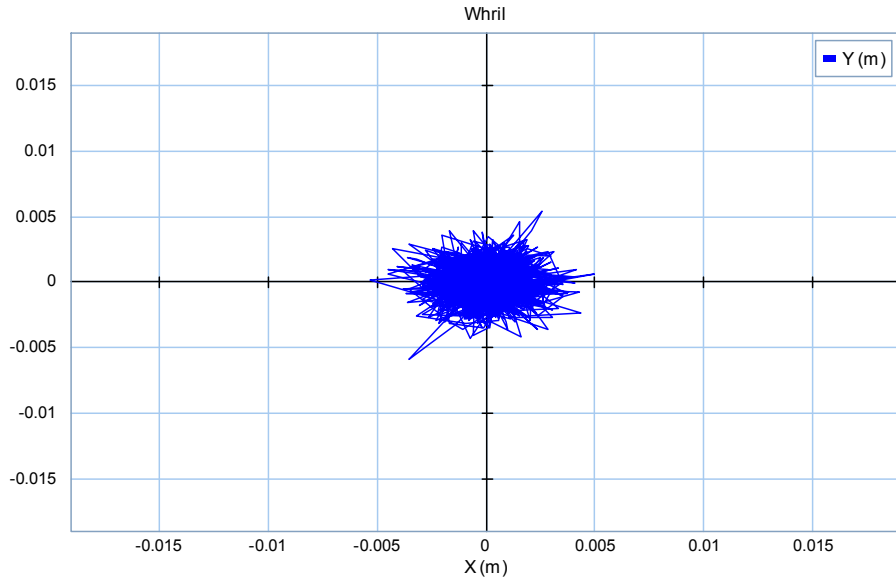


Figure 4.23 Drillstring whirl

Bit type: RC

Depth: 117-127ft

WOB: 35kN

Time: 3450-3500s

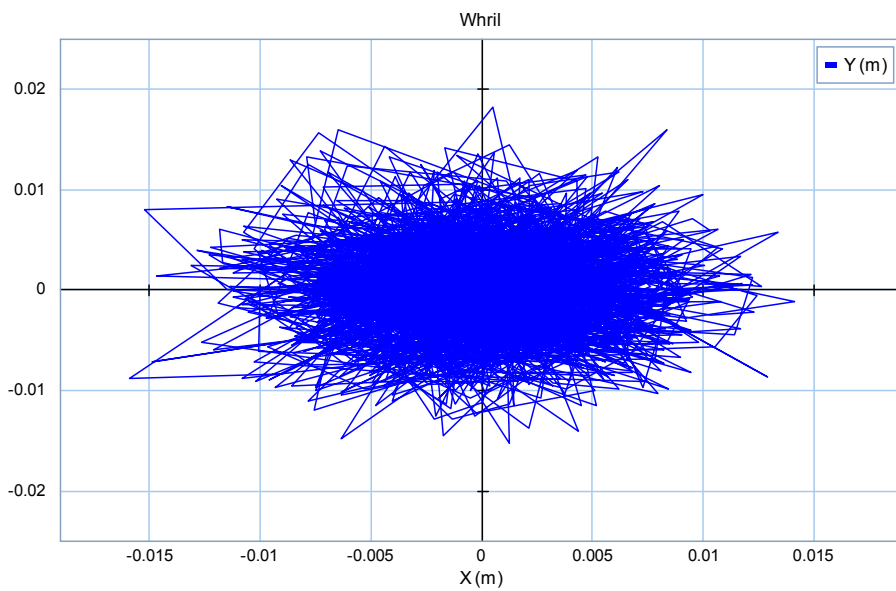


Figure 4.24 Drillstring whirl

Bit type: RC

Depth: 217-227ft

WOB: 143kN

Time: 13250-13300s

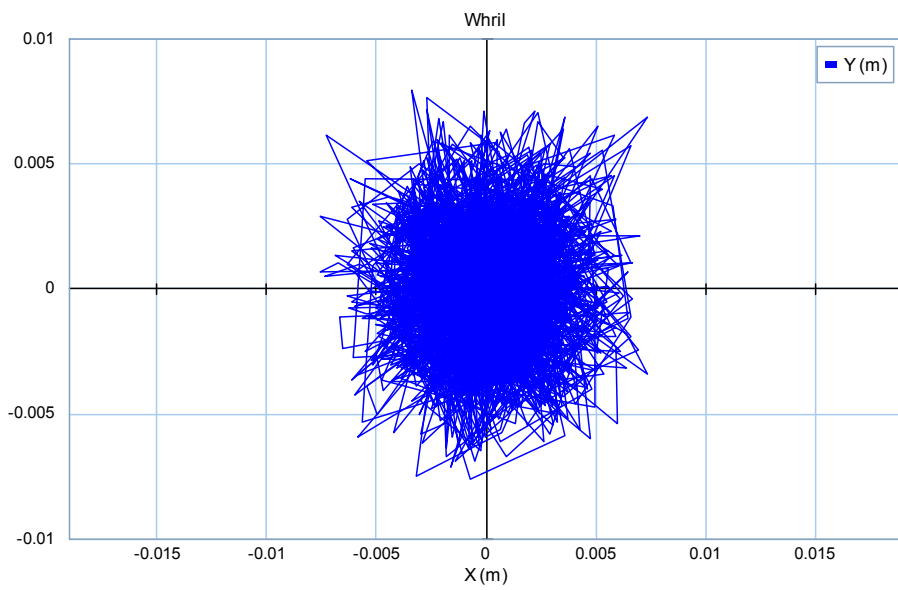


Figure 4.25 Drillstring whirl

Bit type: PDC

Depth: 257-267ft

WOB: 58kN

Time: 24900-24950s

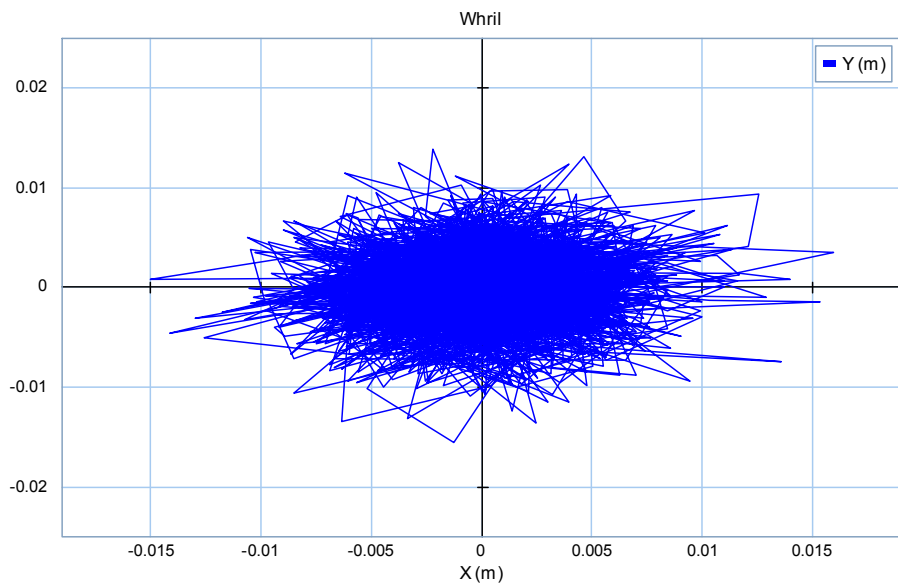


Figure 4.26 Drillstring whirl

Bit type: PDC

Depth: 237-247ft

WOB: 148kN

Time: 22900-22950s

iv. Torsional Acceleration

Torsional acceleration is calculated by using the equation 4.9 explained earlier in the section 4.3 of this chapter. The calculation model for torsional acceleration calculation is presented in Figure 4.10. Angular velocity is calculated from this model and the results are presented from Figure 4.27 to 4.30. Stick slip will take place if the angular velocity goes below *zero*. When low Weight on Bit (WOB) is applied for both PDC and RC bits the angular velocity never goes below *zero*, which confirms that there was no stick slip while low WOB was applied during the drilling operation in the field trial. This phenomena can be seen clearly in Figure 4.27 and 4.29. But in Figure 4.28 and 4.30 it can be seen sometime the angular velocity reaches *zero* or goes below *zero*. Initially it can be seen as stick slip. But the time period of this phenomena is very small i.e. in milliseconds. So this cannot be considered as stick slip as well. So for both PDC and RC bits there was no stick slip during the drilling operation.

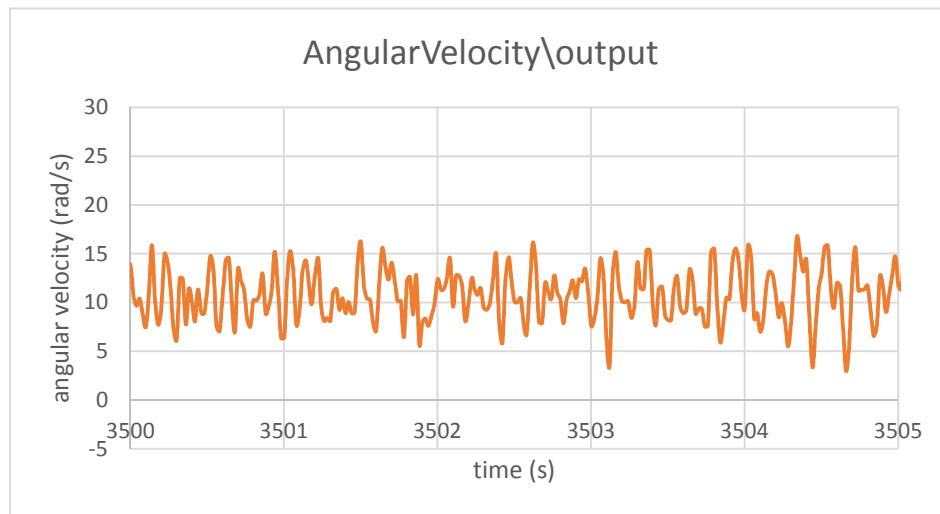


Figure 4.27 Demeaned angular velocity using moving average filter

Depth: 117-127ft WOB: 35kN Bit type: RC Formation: Grey shale

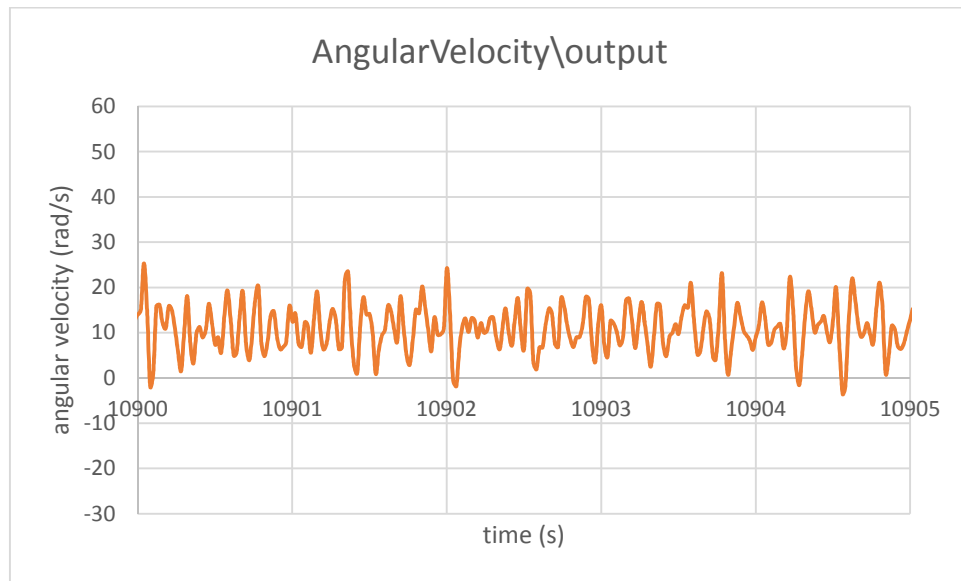


Figure 4.28 Demeaned angular velocity using moving average filter

Depth: 187-197ft WOB: 118kN Bit type: RC Formation: Grey shale + Red

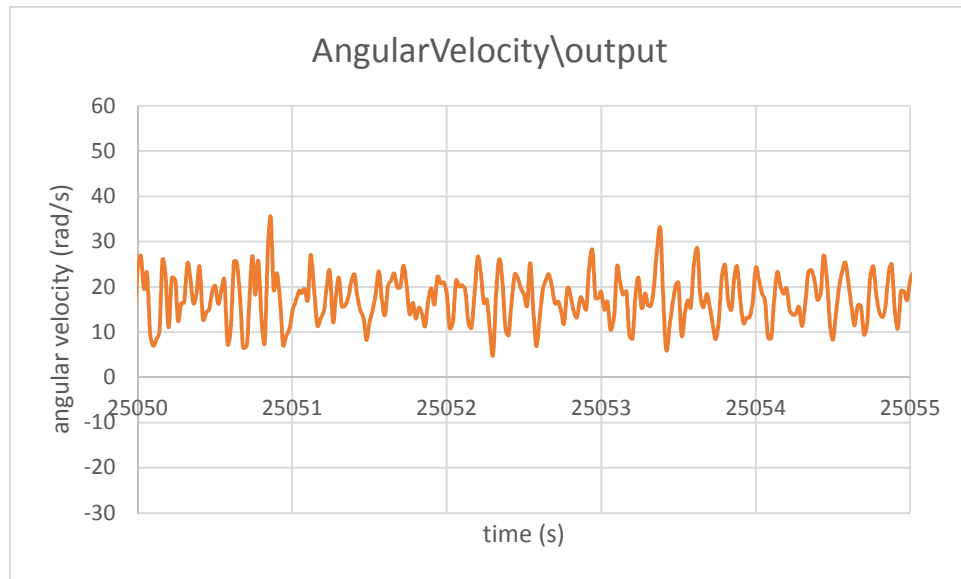


Figure 4.29 Demeaned angular velocity using moving average filter

Depth: 257-267 ft WOB: 58 kN Bit type: PDC Formation: Red shale

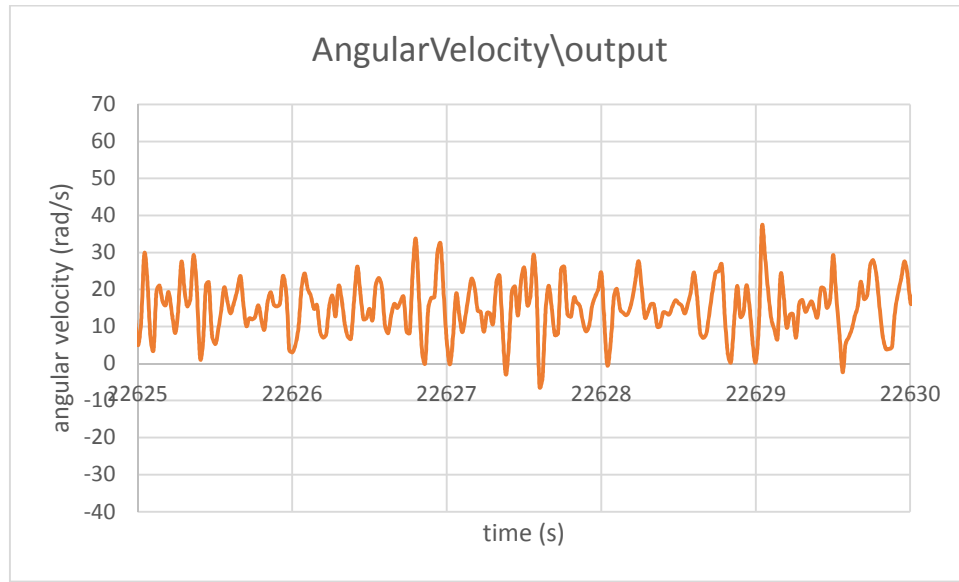


Figure 4.30 Demeaned angular velocity using moving average filter

Depth: 227-237ft WOB: 137kN Bit type: PDC Formation: Red shale

4.4.2 Fast Fourier Transform (FFT)

The Fast Fourier Transform (FFT) is an algorithm for transforming data from the time domain to the frequency domain. Without a time to frequency transform it is not possible to compute the Fourier transform with a microprocessor or any DSP based system [36]. The FFT does not directly give the spectrum of a signal. It depends on the number of points of the FFT, and the number of periods of the signal that are represented. The FFT contains information between zero and sampling frequency. However, the sampling frequency (average number of samples obtained per second) must be at least twice the highest frequency component. Therefore, the signal's spectrum should be entirely below the Nyquist frequency (half of sampling frequency). In this thesis work FFT is used to find out the dominant frequency from the different vibration modes. According to the theory there

should be a dominant frequency at the rotary speed of the drillstring. Other dominant frequencies can be found at the natural frequencies of the system and their harmonics.

4.4.2.1 Test Signal

A test signal is developed to perform the FFT analysis. This test signal contains three waveforms with three different amplitudes and different frequencies. Then these separate signals are combined together and a noisy signal is made from which the data is extracted and then run with the frequency spectrum codes to justify the FFT code. This work is done completely using Matlab.

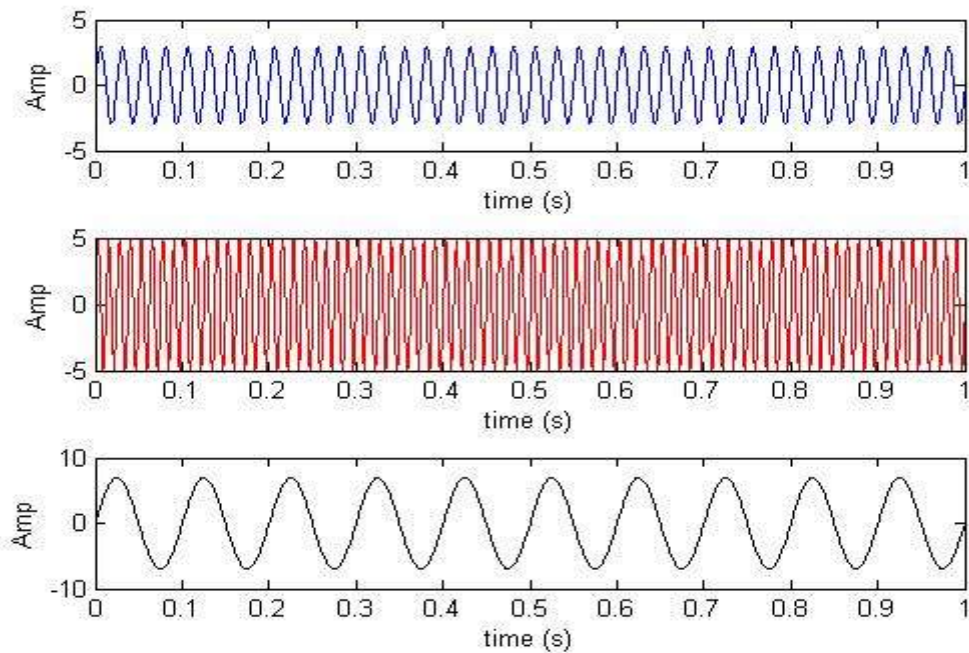


Figure 4.31 Separate test signals for FFT test

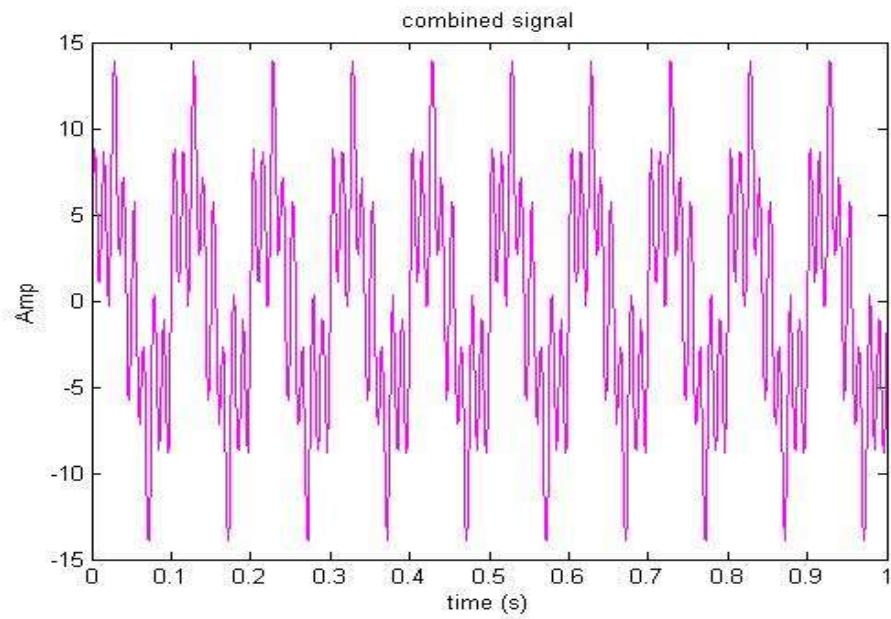


Figure 4.32 Combined test signals for FFT test

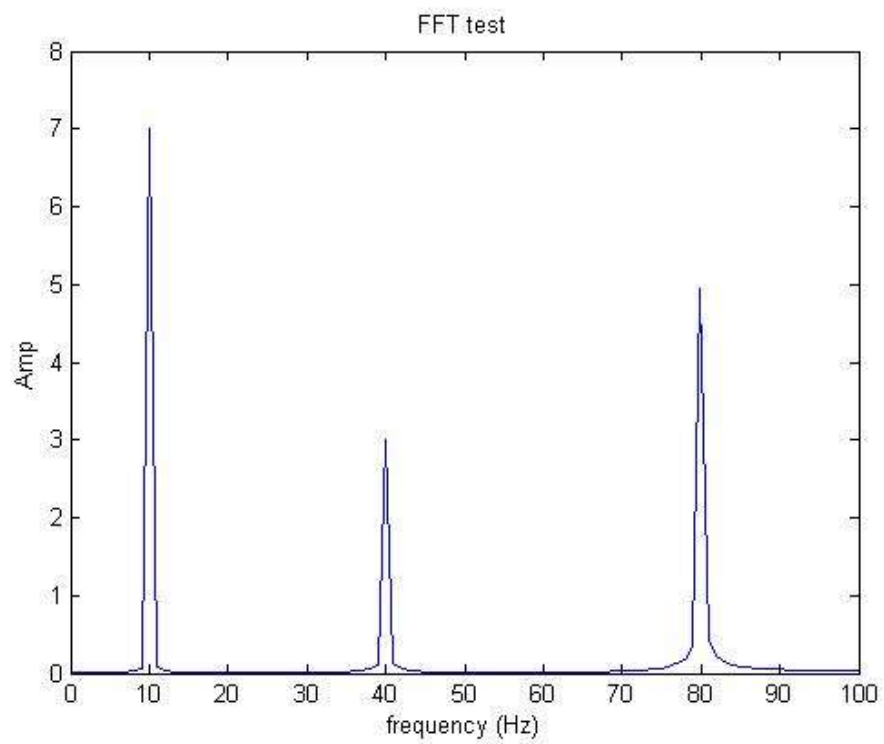


Figure 4.33 Frequency spectrum for FFT test

Figure 4.31 contains three separate signal with three different amplitudes of 3, 5, 7 respectively and corresponding frequency of 40Hz, 80Hz and 10Hz. These signals are combined together and the combined signal is shown in figure 4.32. The data has been extracted from this combined signal and then used in the FFT codes. The result of FFT spectrum test is presented in figure 4.33 where we can see there are three peaks at three different frequencies of 10Hz, 40Hz, 80Hz and corresponding magnitudes are 7, 3, 5. So the spectrum analysis justifies that the FFT codes are correct. This FFT codes will be used to do the spectrum analysis in this thesis work. This code is provided in Appendix B.

4.4.2.2 FFT Results

i. Axial Vibration

The FFT results of the axial vibration are shown in Figure 4.34 and 4.35 where RC and PDC bits are used respectively. When RC bit is used at a depth of 117 – 127 *ft* the surface RPM is 105 (1.75 Hz). So theoretically there should be one dominant frequency peak at the rotary speed but no dominant frequency peak is found from the FFT analysis. First natural frequency for the axial vibration is 32.6 Hz. No dominant frequency is visible at the natural frequency either. Two dominant peaks are found from the FFT analysis at 16.99 Hz and 18.58 Hz. The reason for these peaks are unknown. This could happen due to the rig vibration or from the pump used to circulate the mud. When PDC bit is used at a depth of 257 – 267 *ft* the surface RPM is 144 (2.4 Hz). A dominant frequency is visible at 2.45 Hz in Figure 4.35 but no dominant frequency is visible for the first natural frequency of 15.58 Hz.

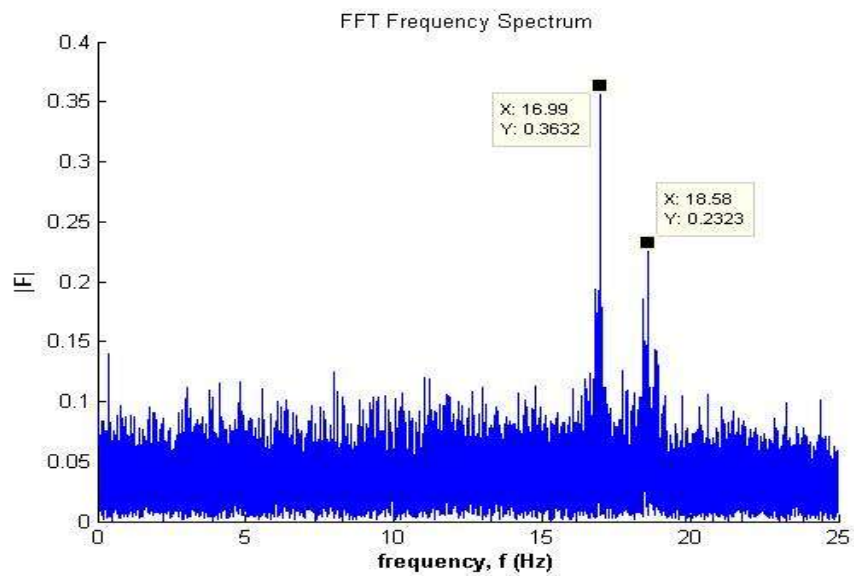


Figure 4.34 Frequency spectrum for axial vibration
 Depth: 117-127 ft WOB: 35 kN Bit type: RC
 ω_1 : 32.61 Hz Surface RPM: 105 (1.75 Hz)

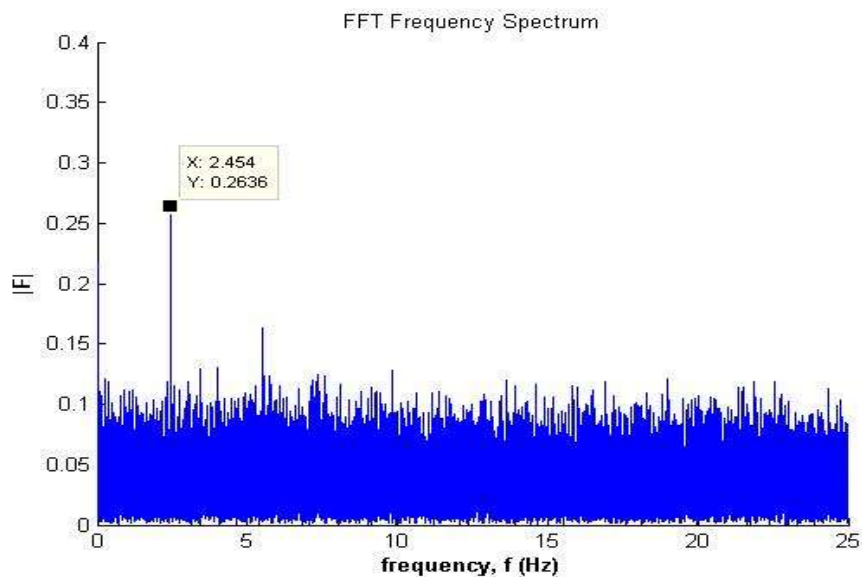


Figure 4.35 Frequency spectrum for axial vibration
 Depth: 257-267 ft WOB: 58 kN Bit type: PDC
 ω_1 : 15.58 Hz Surface RPM: 144 (2.4 Hz)

ii. Torsional Vibration

The results from FFT spectrum analysis of torsional vibration are presented from Figure 4.36 to Figure 4.39. From FFT analysis of torsional vibration data some peak has been found which represents the dominant frequency of the system. Likewise axial vibration there should be one dominant frequency peak at the rotary speed of the system for torsional vibration and at the natural frequency of the system. At a depth of 257 – 267 *ft* from the torsional vibration data a dominant frequency peak is identified at 2.45 Hz along with two other unknown peak at 15.43 Hz and 17.63 Hz. This dominant frequency at 2.45 Hz is also identified from axial vibration data analysis at the same depth. Theoretically, there should be one frequency peak due to first natural frequency of 9.85 Hz for 267 *ft* drillstring but such frequency peak is not identified in the FFT analysis. At a depth of 167 – 177 *ft* a peak is identified at 1.29Hz for the surface RPM of 80 (or 1.33Hz) which is shown in Figure 4.39. Few more dominant frequencies are identified at 14.46 Hz, 18.7 Hz and 18.92 Hz. Among them 14.46 Hz is the first natural frequency of the system but the frequency spikes at 18.7 Hz and 18.92 Hz are unknown. The reason for unknown frequency spikes could be self-vibration of the rig or pump vibration.

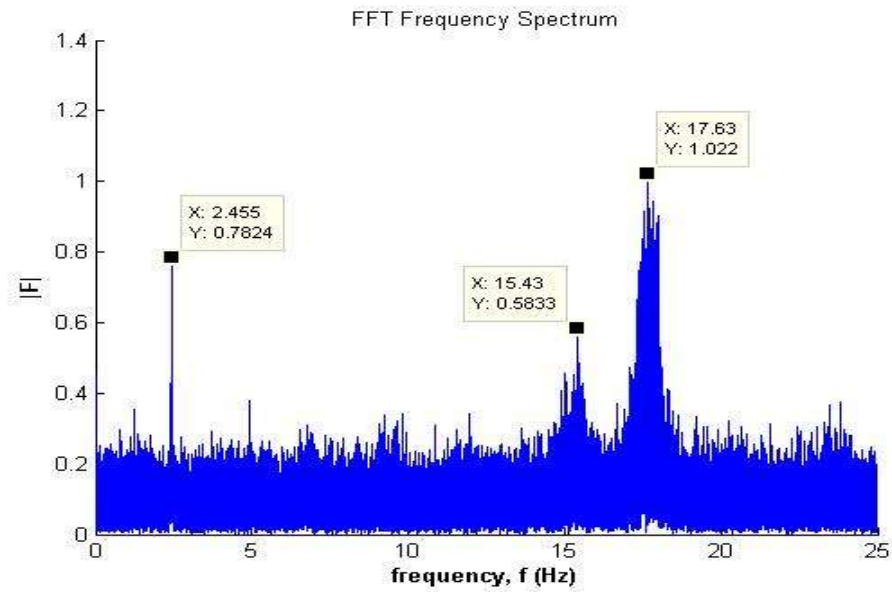


Figure 4.36 Frequency spectrum for torsional vibration
 Depth: 257-267ft WOB: 58kN Bit type: PDC
 ω_1 : 9.85Hz Surface RPM: 144 (2.4 Hz)

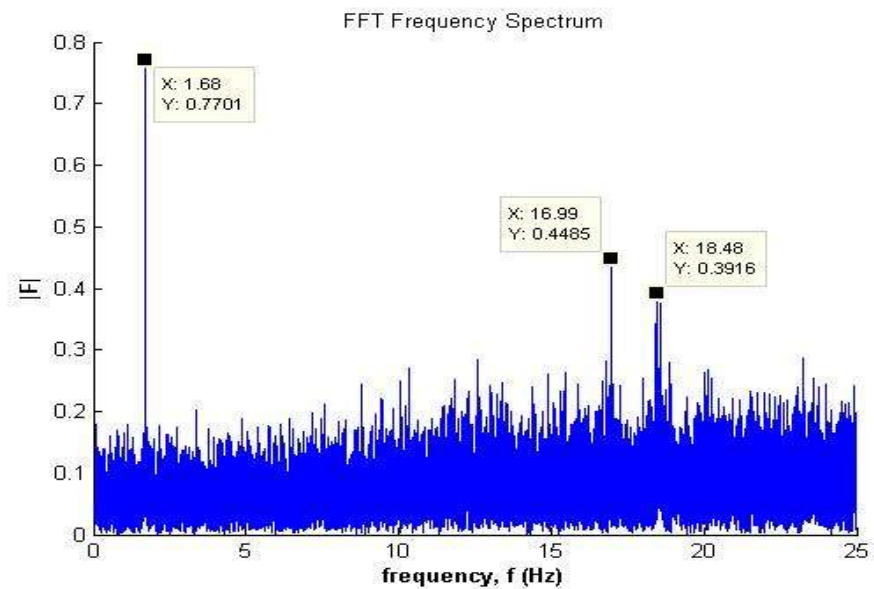


Figure 4.37 Frequency spectrum for torsional vibration
 Depth: 117-127ft WOB: 35kN Bit type: RC
 ω_1 : 20.62Hz Surface RPM: 105

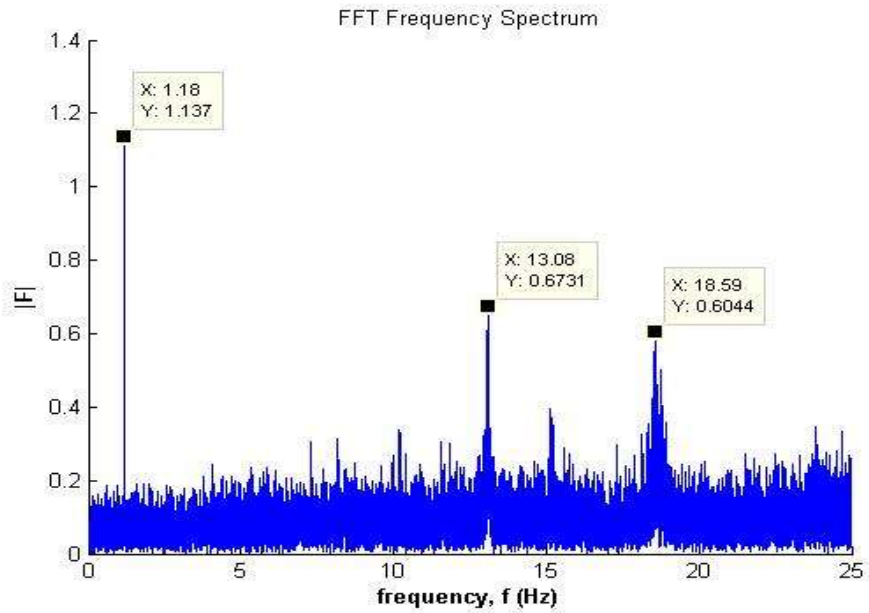


Figure 4.38 Frequency spectrum for torsional vibration

Depth: 137-147ft WOB: 59kN Bit type: RC

ω_1 : 17.81Hz Surface RPM: 70

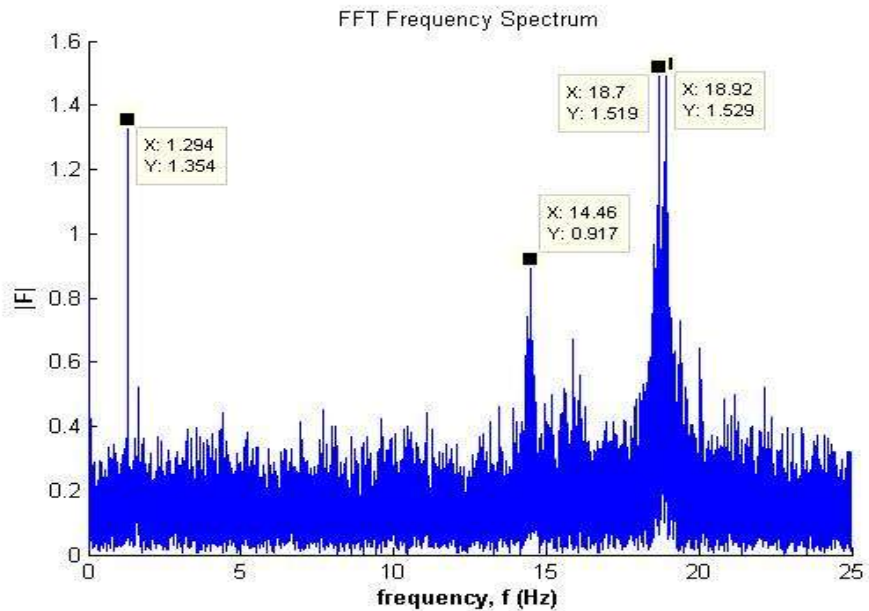


Figure 4.39 Frequency spectrum for torsional vibration

Depth: 167-177ft WOB: 95kN Bit type: RC

ω_1 : 14.79Hz Surface RPM: 80

iii. Lateral Vibration

From the lateral vibration data no significant frequency could be identified from the spectrum analysis. The reason for this is the applied WOB, which was much higher than the critical load. Both component of the lateral vibration are analyzed but no significant frequency peak is identified. Frequency analysis for the lateral vibration data are depicted in Figure 4.40 – 4.43.

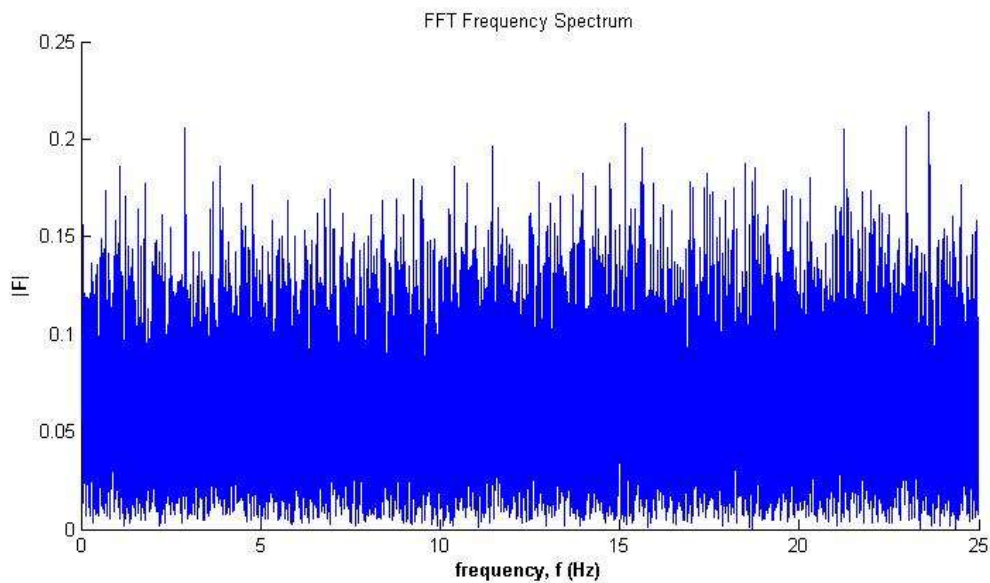


Figure 4.40 Frequency spectrum for lateral vibration (AlatX)

Depth: 127-137ft WOB: 47kN Bit type: RC

ω_{1-4} : 1.04Hz, 4.03Hz, 9.73Hz, 17.33Hz Critical load: 5.94kN Surface RPM: 80

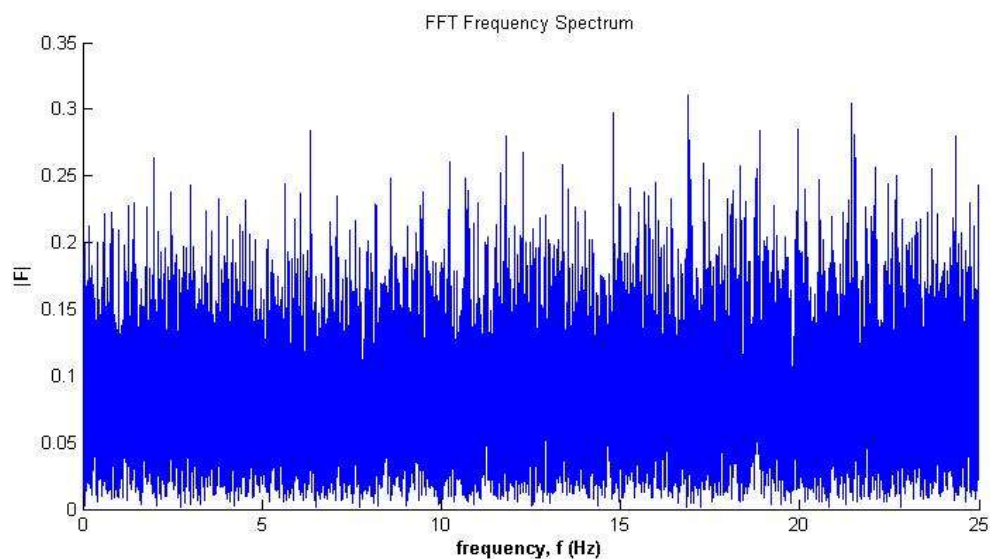


Figure 4.41 Frequency spectrum for lateral vibration (AlatY)
 Depth: 127-137ft WOB: 47kN Bit type: RC
 ω_{1-4} : 1.04Hz, 4.03Hz, 9.73Hz, 17.33Hz Critical load: 5.94kN Surface RPM: 80

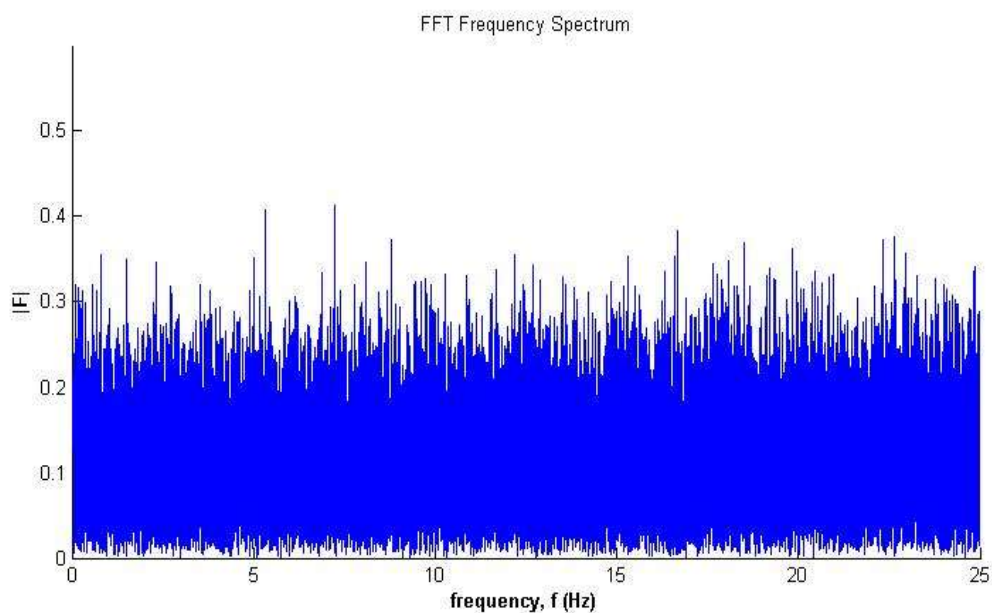


Figure 4.42 Frequency spectrum for lateral vibration (AlatX)
 Depth: 257-267ft WOB: 58kN Bit type: PDC
 ω_{1-4} : 0.2Hz, 0.95Hz, 2.2Hz, 3.95Hz Critical load: 1.59kN Surface RPM: 144

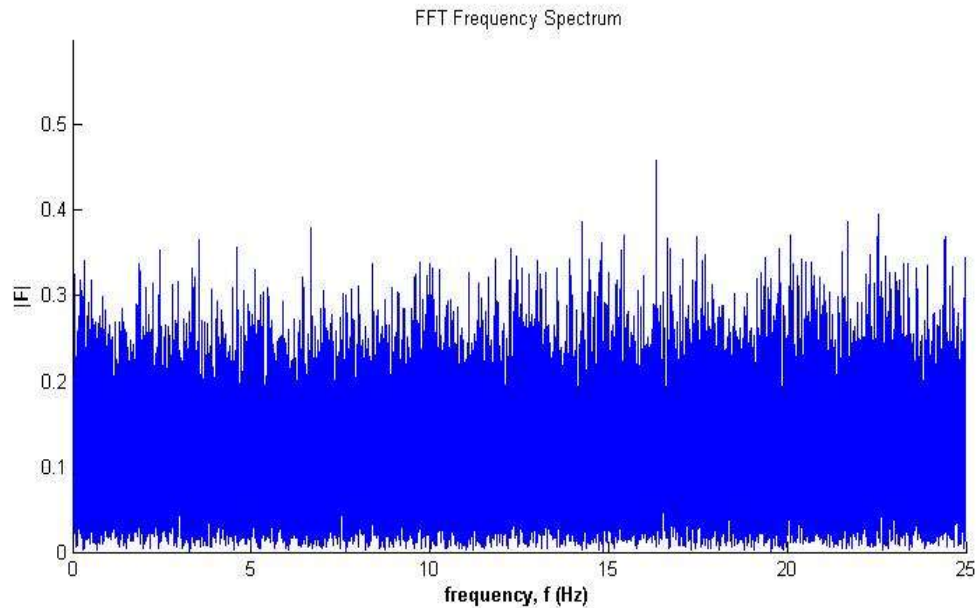


Figure 4.43 Frequency spectrum for lateral vibration (AlatY)
 Depth: 257-267ft WOB: 58kN Bit type: PDC
 ω_{1-4} : 0.2Hz, 0.95Hz, 2.2Hz, 3.95Hz Critical load: 1.59kN Surface RPM: 144

A low pass filter with a cut off frequency of 10 Hz has been used to remove the unknown frequencies found in the spectrum analysis. The FFT spectrum analysis results for torsional vibration data are shown in the figure 4.44 – 4.45. The low pass filter takes out all the high frequency contents while keeping any frequency below the cut of frequency.

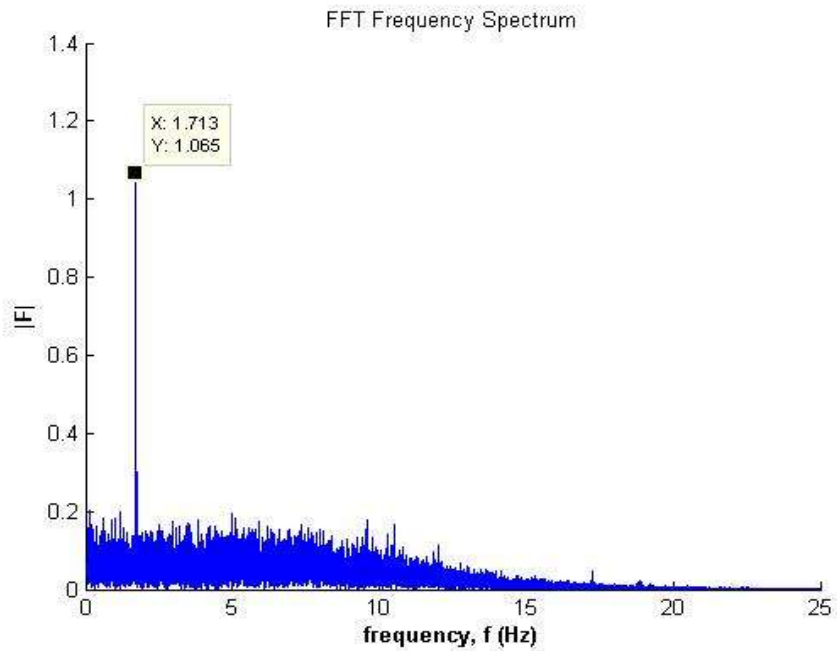


Figure 4.44 Frequency spectrum for torsional vibration with low pass filter
Depth: 117-127 ft WOB: 35 kN Bit type: RC RPM: 105 (1.75 Hz)

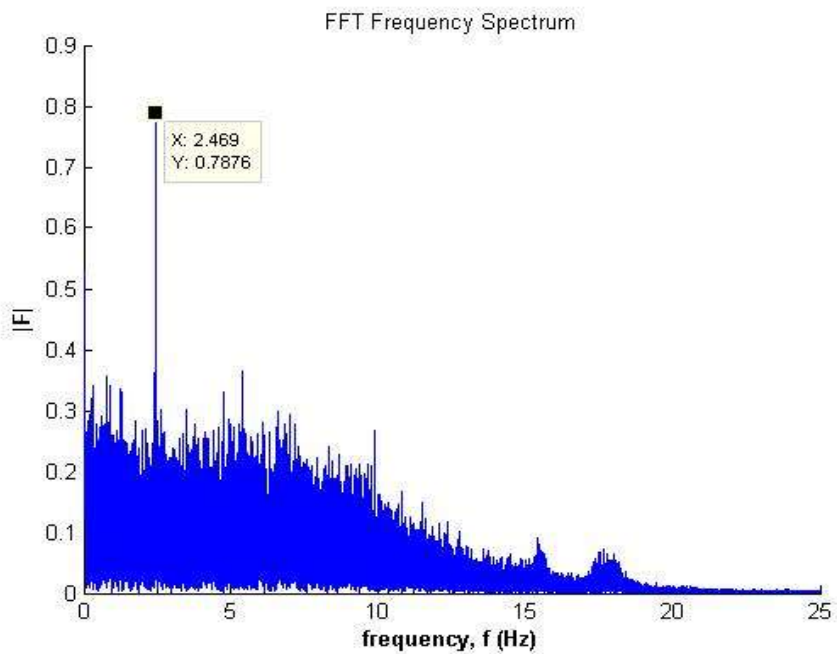


Figure 4.45 Frequency spectrum for torsional vibration with low pass filter
Depth: 257-267ft WOB: 58kN Bit type: PDC RPM: 144 (2.4 Hz)

4.5 RPM

Rotary speed of the drillstring is calculated from the data acquired from magnetometer using the equations provided in section 4.3 of this chapter. Magnetometer gives the data in radians and from this recorded data the rotary speed is calculated by differentiating the magnetometer data against the recorded time. As the sampling rate of the downhole sensor sub is quite low (20 ms), when the RPM is calculated it is found that RPM becomes “zero” for 2 or 3 intervals. Primarily, looking into this it seems that this is happening as a result of the presence of stick-slip in the system. But this is not stick-slip. The reason for this is the system is recoding data 2 or 3 times when the drillstring is in the same position as the sampling rate is low. Stick-slip could be identified if the drillstring remains in the same position for a longer period e.g. RPM remains zero for a long period of time. So the data was smoothed out using MATLAB and the average rotary speed and instantaneous rotary speed is calculated. The MATLAB code for magnetometer data smoothing is provided in Appendix B.

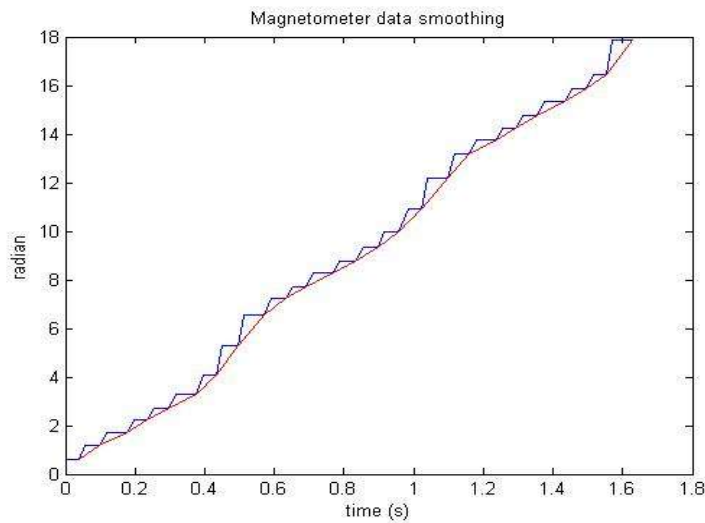


Figure 4.46 Magnetometer data smoothing for RPM calculation

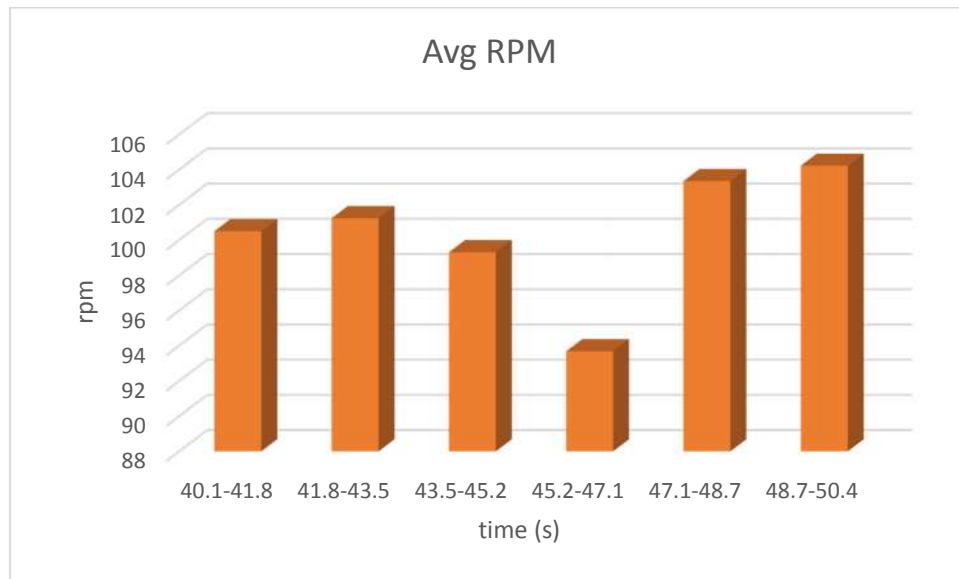


Figure 4.47 Average rotary speed of drillstring

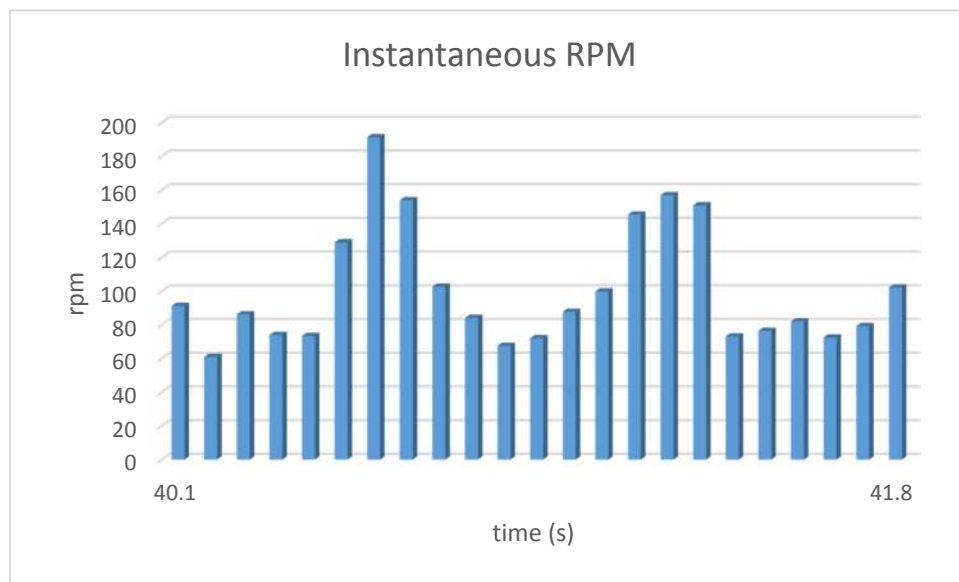


Figure 4.48 Instantaneous rotary speed of drillstring

Depth: 217-227ft Bit type: RC Surface RPM: 105 Formation: Red & grey shale

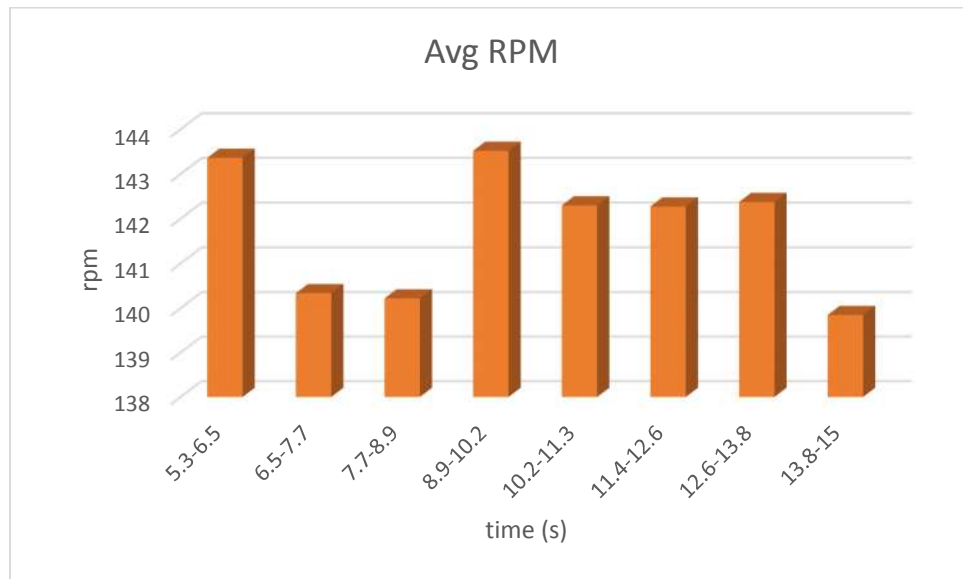


Figure 4.49 Average rotary speed of drillstring

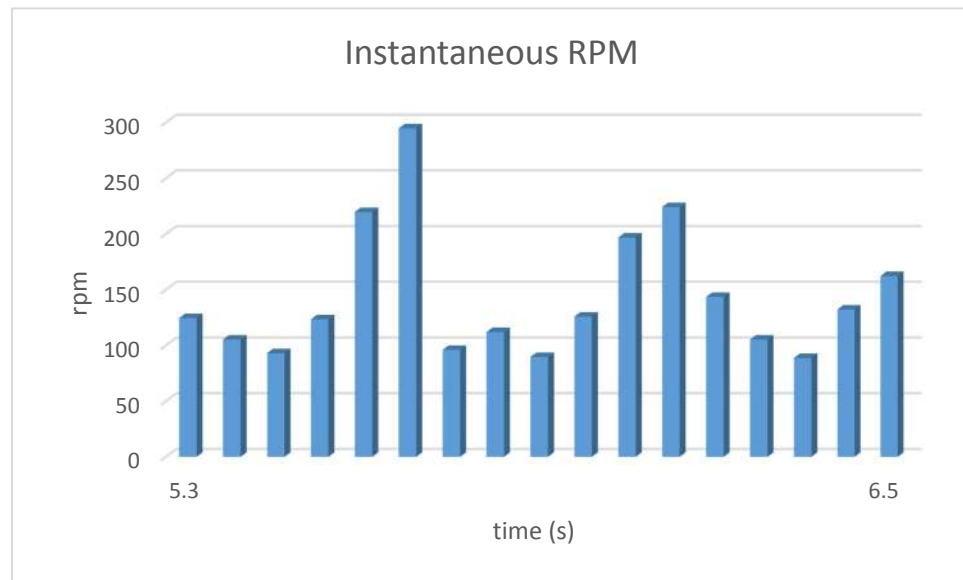


Figure 4.50 Instantaneous rotary speed of drillstring

Depth: 257-267ft Bit type: PDC Surface RPM: 144 Formation: Red shale

Figure 4.47 – 4.50 shows the average RPM and the instantaneous RPM of the rotating drillstring calculated from the magnetometer data. While RC bit is used at a depth of 217 – 227 *ft*, the average RPM calculated from magnetometer data for the selected time interval is about 100. The surface RPM measured at that time is 105. Similarly, for the while PDC bit is used the surface RPM is measured 144 and average RPM calculated from the magnetometer data is about 142.

This chapter provides an interpretation method for the data recorded by the downhole vibration monitoring tool. Data processing procedure and results from the post processed data are discussed in this chapter. Severity of the downhole vibration can be determined from the analyzed data and the information can be used for other wells during drilling operation.

5 CHAPTER 5:

FIELD VIBRATION PREDICTION

5.1 Introduction

It is very important to validate the data recorded by the tool with a numerical model. In this chapter, a 2D model is developed to predict the natural frequency of the drillstring, which also can be used to determine the severity of vibration. The natural frequency of a uniform drillstring is calculated for three different types of vibration mode- axial, torsional and lateral. Bond graph [40] method is used in 20-sim software package to develop the model.

5.2 Natural Frequency

If a system undergoes an initial disturbance and after the initial disturbance the system vibrates on its own, the frequency with which it oscillates without any external forces is

known as its natural frequency of that system. Figure 5.1 shows a mass-spring system with a single degree of freedom.

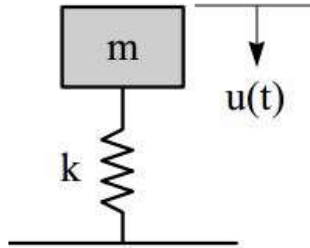


Figure 5.1 Mass spring system [47]

The natural frequency of this system can be determined using the mass of the system and its stiffness. This is the simplest type of system and its natural frequency can be expressed using the following equation:

$$\omega_n = \sqrt{\frac{k}{m}} \quad (5.1)$$

Where,

m = mass

k = stiffness of the spring

ω_n = natural frequency of the system in rad/s

The natural frequency can be converted into Hertz (Hz) using the following equation:

$$f_n = \frac{\omega_n}{2\pi} \quad (5.2)$$

5.3 Theory of Vibration

5.3.1 Axial Vibration

Figure 5.2 shows a non-uniform bar with varying cross sectional area which is subjected to an external force. The equation of motion for the forced axial vibration of this bar is obtained from Rao [41] as follows:

$$\frac{\partial}{\partial x} \left[EA(x) \frac{\partial u(x, t)}{\partial x} \right] + f(x, t) = \rho(x)A(x) \frac{\partial^2 u}{\partial t^2}(x, t) \quad (5.3)$$

Where,

E = Young's modulus

$A(x)$ = Varying cross sectional area

$f(x, t)$ = External force per unit length

$\rho(x)$ = Mass density of the bar section

$\frac{\partial u(x, t)}{\partial x}$ = Axial strain of the small element

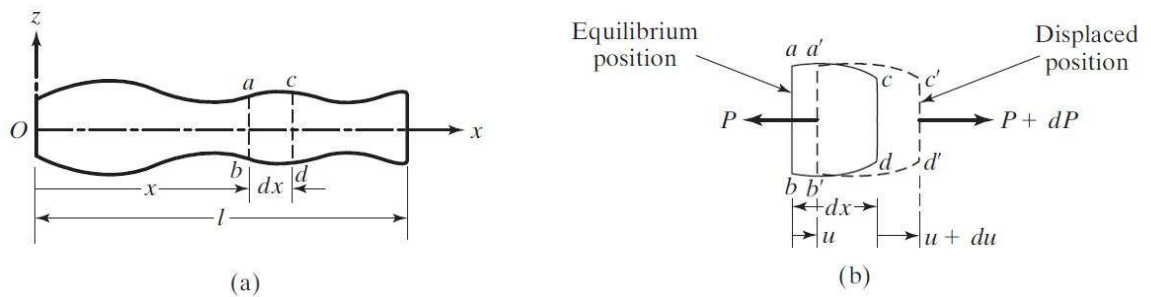


Figure 5.2 Longitudinal vibration of a bar [41]

For uniform cross section of the drillstring, considering free vibration and fixed free boundary condition, the theoretical natural frequency is calculated using the following equation [41]

$$\omega_n = \frac{(2n - 1)\pi}{2l} \sqrt{\frac{E}{\rho}} ; \quad n = 1, 2, 3, \dots \quad (5.4)$$

where,

ω_n = Natural frequency (rad/s) = $2\pi f$

E = Young's modulus

ρ = Density of the material

l = Length of the drillstring

n = n^{th} natural frequency

Table 5.1 shows the first four natural frequencies for axial vibration calculated from the equation 5.4. Three different lengths were chosen to calculate natural frequency for the dynamic test in field trial and compare the natural frequency if better data was obtained from the field trial. Unfortunately, no sensor sub data was recorded during the dynamic test as the tool's sealing and electrical connections broke down due to vibration. Figure 5.3 shows the axial natural frequency for different lengths. If the data could be recorded it would show that axial natural frequency decreases with the increase of length which would verify the theory of axial vibration.

Table 5.1 Theoretical natural frequency for axial vibration

Length, L (m)	Density, ρ (kg/m ³)	Elastic modulus, E (Pa)	Natural Frequency (Hz)			
			1st	2nd	3rd	4th
50	7850	2.00E+11	25.24	75.71	126.19	176.66
100	7850	2.00E+11	12.62	37.86	63.09	88.33
140	7850	2.00E+11	9.01	27.04	45.07	63.09

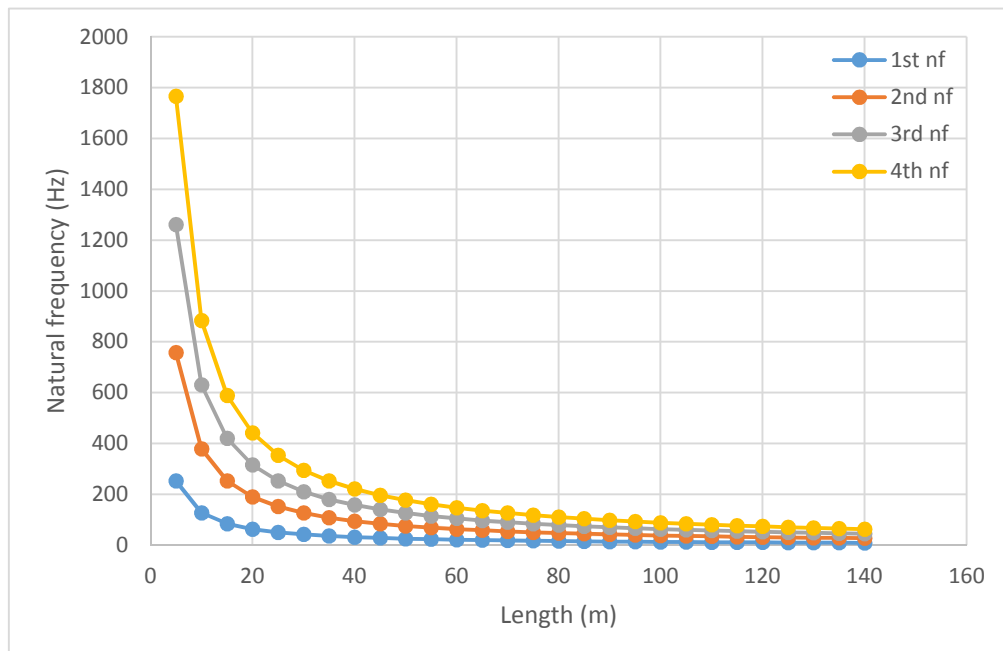


Figure 5.3 Natural frequency (axial) vs length graph

5.3.2 Torsional Vibration

Figure 5.4 shows a non-uniform shaft with varying cross sectional area which is subjected to an external torque. The equation of motion for the forced torsional vibration of this shaft is obtained from Rao [41] as follows:

$$\frac{\partial}{\partial x} \left[GJ(x) \frac{\partial \theta(x, t)}{\partial x} \right] + f(x, t) = I_0(x) \frac{\partial^2 \theta}{\partial t^2}(x, t) \quad (5.5)$$

Where,

G = Shear modulus

$J(x)$ = Polar moment of inertia of the cross section for a circular section

$GJ(x)$ = Torsional stiffness of the cross section

$\frac{\partial \theta(x, t)}{\partial x}$ = Change of angle of twist of the cross section

$f(x, t)$ = External torque per unit length

$I_0(x)$ = Mass polar moment of inertia per unit length

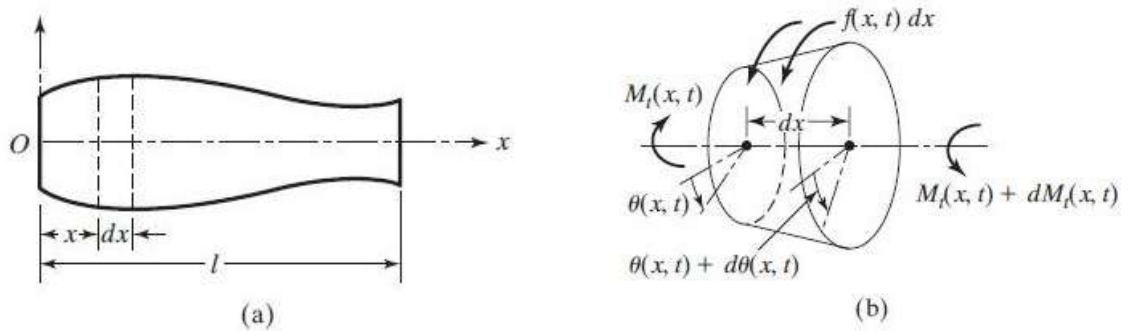


Figure 5.4 Torsional vibration of a shaft [41]

For uniform cross section of the drillstring, considering free vibration and fixed free boundary condition, the theoretical natural frequency is calculated using the following equation [41]

$$\omega_n = \frac{(2n - 1)\pi}{2l} \sqrt{\frac{G}{\rho}} ; \quad n = 1, 2, 3 \dots \quad (5.6)$$

where,

ω_n = Natural frequency (rad/s) = $2\pi f$

G = Shear modulus

ρ = Density of the material

l = Length of the drillstring

n = n^{th} natural frequency

Table 5.2 shows the first four natural frequencies for torsional vibration calculated from the equation 5.6. Similar to axial vibration, three different lengths were chosen to calculate natural frequency for the dynamic test in field trial and compare the natural frequency if better data was obtained from the field trial. But unfortunately no sensor sub data was recorded during the dynamic test as the tool's sealing and electrical connections broke down due to vibration. Figure 5.5 shows the torsional natural frequency for different lengths. If the data could be recorded it would show that axial natural frequency decreases with the increase of length which would verify the theory of torsional vibration.

Table 5.2 Theoretical natural frequency for torsional vibration

Length, L (m)	Density, ρ (kg/m ³)	Shear modulus, G (Pa)	Natural Frequency (Hz)			
			1st	2nd	3rd	4th
50	7850	8.00E+10	15.96	47.89	79.81	111.73
100	7850	8.00E+10	7.98	23.94	39.90	55.87
140	7850	8.00E+10	5.70	17.10	28.50	39.90

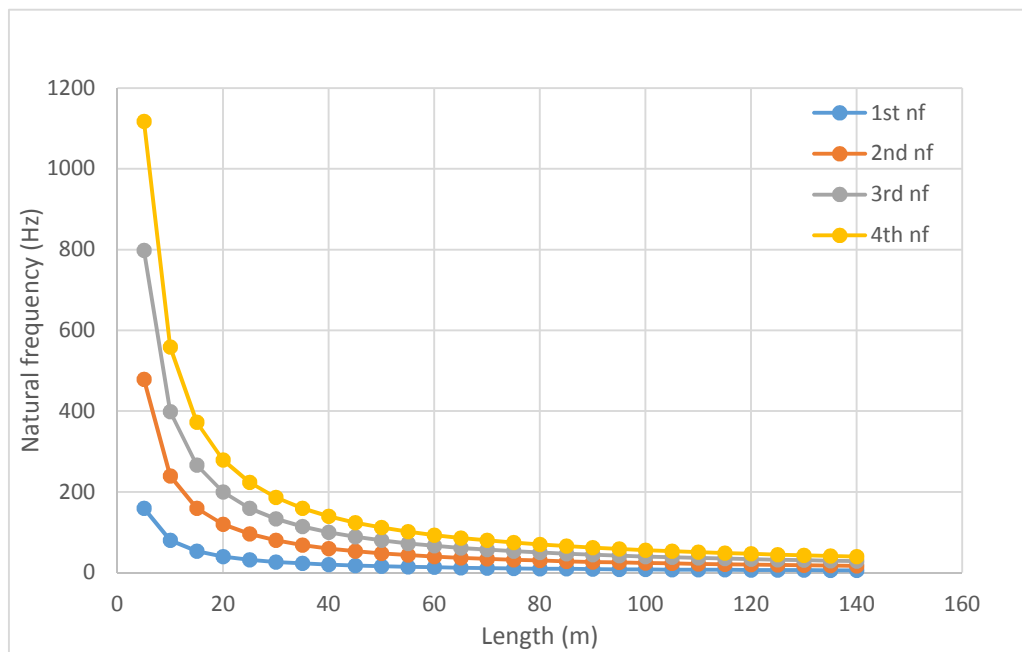


Figure 5.5 Natural frequency (torsional) vs length graph

5.3.3 Lateral Vibration

For lateral vibration both shear force and bending moment is taken into consideration.

Figure 5.6 (a) shows a beam subjected to an external force $f(x, t)$. The free body diagram of an element of this beam is shown in Figure 5.6 (b). The equation of motion for the forced lateral vibration of a non-uniform beam is obtained from Rao [41] which is expressed as follows:

$$\frac{\partial^2}{\partial x^2} \left[EI(x) \frac{\partial^2 w}{\partial x^2}(x, t) \right] + \rho A(x) \frac{\partial^2 w}{\partial t^2}(x, t) = f(x, t) \quad (5.7)$$

Where,

E = Young's modulus

I = Moment of inertia of the beam

$\frac{\partial w}{\partial x}$ = Deflection of the beam

ρ = Density of the material

$A(x)$ = Cross sectional area of the beam

$f(x, t)$ = External force on the beam

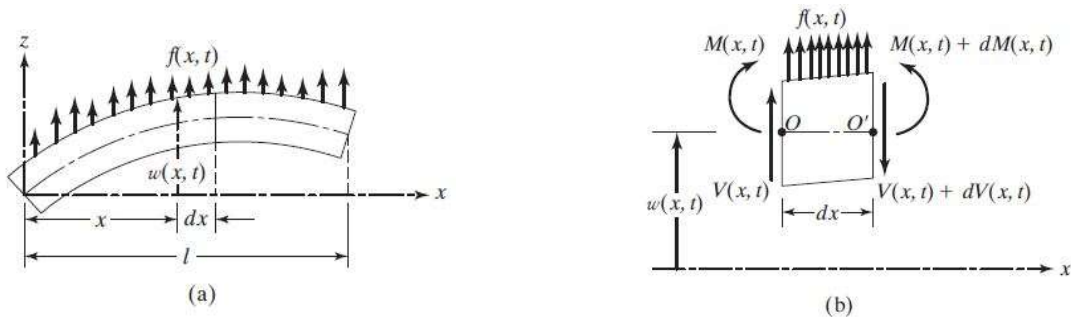


Figure 5.6 Lateral vibration of a beam [41]

For uniform cross section of the drillstring, considering free vibration and fixed free boundary condition, the theoretical natural frequency is calculated using the following equation [41]

$$\omega_n = (\beta l_n)^2 \sqrt{\frac{EI}{\rho A l^4}} ; \quad n = 1, 2, 3 \dots \quad (5.8)$$

Where,

ω_n = Natural frequency (rad/s) = $2\pi f$

E = Young's modulus

ρ = Density of the material

l = Length of the drillstring

A = Cross sectional area of drillstring

I = Area moment of inertia

n = n^{th} natural frequency

$\beta l_1 = 1.875104$ (constant)

$\beta l_2 = 4.694091$ (constant)

$\beta l_3 = 7.854757$ (constant)

$\beta l_4 = 10.995541$ (constant)

Similar to axial and torsional vibration, lateral vibration is calculated and Table 5.3 represents the calculated natural frequency for different lengths which were chosen for dynamic test in the field trial. The natural frequencies represented in the Table 5.3 is

calculated using a 4.5 inches OD and 3.5 inches ID which are the diameter of the drillpipe used in field trial. The natural frequencies calculated are also shown in Figure 5.7 which shows that natural frequency decreases with increasing of drillpipe length.

Table 5.3 Theoretical natural frequency for lateral vibration

Length, L (m)	Area A (m ²)	Moment of Inertia, I (m ⁴)	Density ρ (kg/m ³)	Elastic Modulus E (Pa)	Natural Frequency (rad/s)			
					1st	2nd	3rd	4th
50	0.0041	5.3123E-06	7850	2.00E+11	0.25	1.61	4.51	8.84
100	0.0041	5.3123E-06	7850	2.00E+11	0.06	0.40	1.13	2.21
140	0.0041	5.3123E-06	7850	2.00E+11	0.03	0.21	0.58	1.13

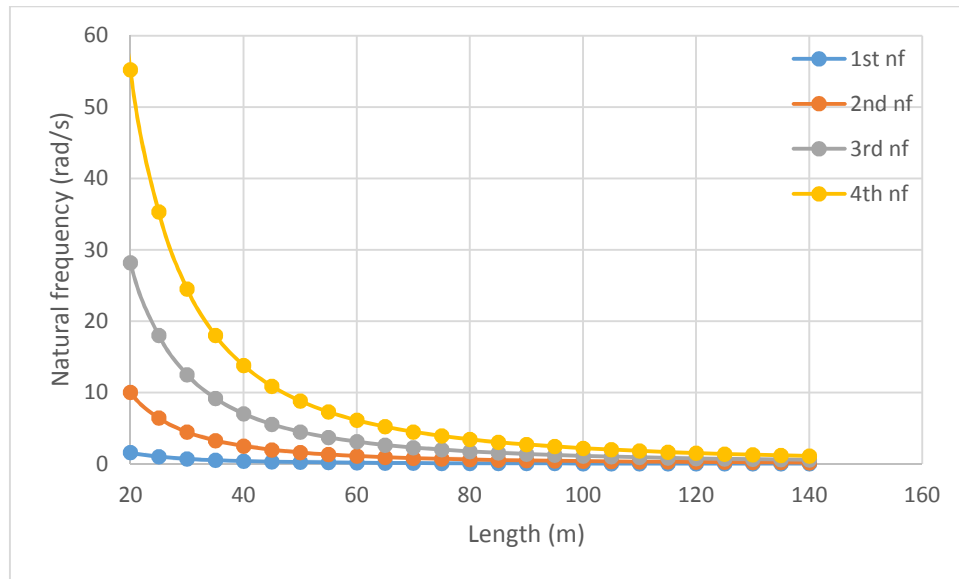


Figure 5.7 Natural frequency (lateral) vs length graph

5.4 Simulation

5.4.1 Bond Graph Background

Bond graph is a domain independent graphical description of dynamic behavior of physical systems. In a simpler way, it means the systems from different domains such as electrical, mechanical, hydraulic, acoustical, thermodynamic, chemical are described in the same way. The basis of bond graphs are based on energy and energy exchange. Bond graphs are used to study different kinds of dynamic systems. This is a powerful graphical modelling tool in which different physical systems can be modelled, especially when different physical domains are involved. The concept of bond graphs was invented by Professor Henry M. Paynter, MIT in 1959. Later bond graphs were developed by various researchers like Dean C. Karnopp, Ronald C. Rosenberg, Peter Breedveld, Jean Thoma etc. [42]. By this approach, a physical system can be represented by symbols and lines, identifying the power flow paths. Power flows from one component to another. The elements are interconnected in an energy conserving domain by bonds and junctions resulting a network structure. From the pictorial representation of the bond graph, the derivation of system equations is so systematic that it can be algorithmized. The whole procedure of modeling and simulation of the system may be performed by some of the existing software e.g., ENPORT, Camp-G, SYMBOLS, COSMO, LorSim, 20-sim etc. [40, 42]. In this thesis work 20-sim [43] is used to model and simulate the systems.

The elements of the bond graphs are connected with power bonds, each of which contains a pair of signals generally known as “effort” and “flow”. The product of this “effort” and

“flows” gives the instantaneous power of the bond. Table 5.4 shows the effort and flow variables in some physical domains.

Table 5.4 Effort and flow variables in different physical domain

Domain	Effort (e)	Flow (f)
Mechanical translation	Force (F)	Velocity (v)
Mechanical rotation	Torque (τ)	Angular velocity (ω)
Electrical	Voltage (V)	Current (i)
Hydraulic	Pressure (P)	Volume flow rate (Q)
Thermal	Temperature (T)	Entropy change rate (ds/dt)
Magnetic	Magneto-motive force (e_m)	Magnetic flux (ϕ)

5.4.2 Bond Graph Basic Elements

5.4.2.1 Basic 1-Port Elements

1-port element is addressed through a single power port, and at the port a single pair of effort and flow variables exists. Bond graphs use five types of idealized 1-port elements. Among these elements two are active and three are passive. The active ports give reaction to the source but the passive ports are idealized elements because they contain no sources of power. The two active 1-port elements are the effort source and the flow source. [42] Figure 5.8 shows the active ports of basic 1-port elements.

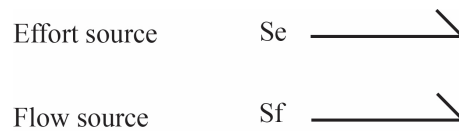


Figure 5.8 Bond graph representation ideal sources

The passive 1-port elements exchange power from one to another in their own unique way. They are called passive elements because they don't contain any source of power. Among three passive elements two are energy storage elements and the other one is dissipative element. The two energy storage elements are inductive and capacitive elements represented by I and C respectively. The dissipative element is the resistance which is represented by R . Depending on the domain the resistive element represents mechanical friction, electrical resistance, thermal resistance etc. The inductive element represents mechanical mass for translational motion, mass moment of inertia for rotary motion for mechanical domain, electrical resistance for electrical domain. The capacitive element represents the mechanical compliance, electrical capacitance for mechanical domain and electrical domain respectively. Figure 5.9 shows the passive ports for basic 1-port elements. [40]

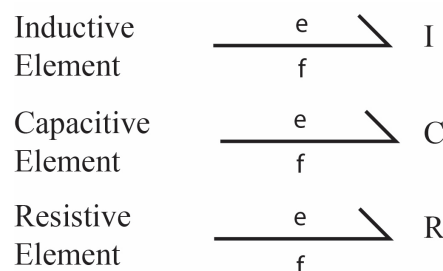


Figure 5.9 Bond graph representation of inductive, capacitive and inductive element

Equations for I element:

If the mechanics of a point mass is examined by considering the impulse-momentum equation, then the relationship can be expressed as:

$$P = \int_{-\infty}^t e \, dt \quad (5.9)$$

$$f = \frac{1}{m} \int_{-\infty}^t e \, dt \quad (5.10)$$

Here, effort is effort is the cause and velocity (and hence momentum) is the consequence.

Equations for C element:

In a spring, the deformation (Q) and the effort (e) at any moment is given by,

$$Q = \int_{-\infty}^t f \, dt \quad (5.11)$$

$$e = k \int_{-\infty}^t f \, dt \quad (5.12)$$

Here, flow is the cause and deformation (and hence effort) is the consequence.

Equations for R element:

The half arrow pointing towards R means that the power i.e. product of F and V (or $e * f$) is positive and flowing into R , where e represents effort or force, and f represents flow or velocity. The constitutive relationship between e, f and R is given by:

$$e = R * f \quad (5.13)$$

$$Power = e * f = R * f^2 \quad (5.14)$$

5.4.2.2 Basic 2-Port Elements

There are two types of 2-port elements exist in bond graph modeling. One is “Transformer” and the other one is “Gyrator”. An ideal transformer is represented by “TF” and an ideal gyrator is represented by “GY”. Likewise passive 1-port elements, the 2-port elements do not contain power sources. They also don’t store or dissipate power from the system. For both “Transformer” and “Gyrator”, power-in equals power-out. Figure 5.10 shows the bond graph representation of transformer and gyrator.

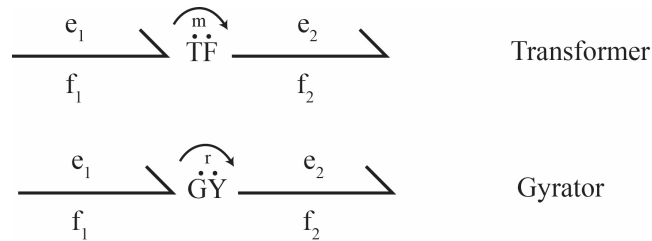


Figure 5.10 Bond graph representation of basic 2-port elements

The transformer relates the effort on one side of the transformer to the effort on the other side, and the flow on one side to the flow on the other. The gyrator relates the effort on one side of the gyrator to the flow on the other.

The constitutive laws of the ideal 2-port transformer are-

$$e_1 = m * e_2 \quad (5.15)$$

$$m * f_1 = f_2 \quad (5.16)$$

where the parameter m is called the transformer modulus and number 1 and 2 correspond to two ports.

The constitutive laws of the ideal 2-port gyrator are-

$$e_1 = r * f_2 \quad (5.17)$$

$$r * f_1 = e_2 \quad (5.18)$$

where the parameter r is called the gyrator modulus and number 1 and 2 correspond to two ports.

Nonlinear transformer and gyrator uses the same relationships as linear transformer and gyrator described above. The difference is- in case of nonlinear transformer and gyrator the modulus is not constant. These elements are called modulated transformer represented by MTF and modulated gyrator represented by MGY. [40, 44]

5.4.2.3 Basic 3-Port Junction Elements

In bond graph two basic 3-port elements exist. These 3-ports are called junctions as they connect other multiport into the system. They allow all energy domains to be assembled into overall system models. They conserve power and are reversible. No energy is stored or dissipated in the junctions. The two basic 3-port elements are- the 0-junction and the 1-junction.

The 0-junction represents a node at which all efforts of the connecting bonds are equal and flows algebraically sum to zero. The 0-junction is also known as flow junction or common effort junction. Figure 5.11 shows the basic 0-junction used in bond graph.

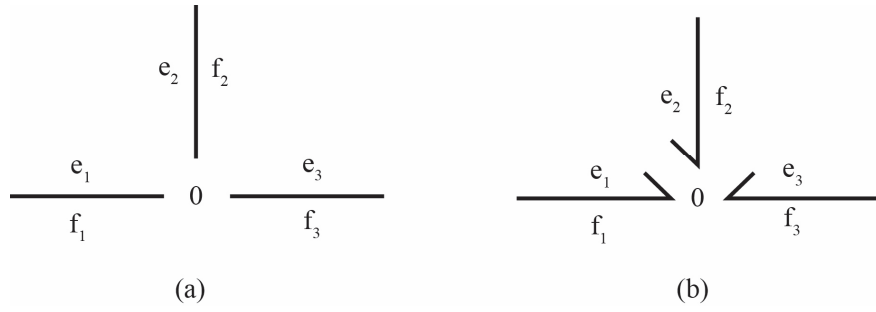


Figure 5.11 Bond graph representation of 0-junction

Using the inward power sign convention showed in Figure 5.11(b), the constitutive relation can be written as follows:

$$e_1 f_1 + e_2 f_2 + e_3 f_3 = 0 \quad (5.19)$$

In the 0-junction all efforts are same, thus,

$$e_1(t) = e_2(t) = e_3(t) \quad (5.20)$$

$$f_1(t) + f_2(t) + f_3(t) = 0 \quad (5.21)$$

In the 0-junction the efforts in all bonds are always identical and the algebraic sum of the flows always vanishes. In other words, if power is flowing in two ports of three, then it must be flowing out of the third port. The signs in the algebraic sum are determined by the half-arrow directions in a bond graph. All inward pointing bonds get a plus and all outward pointing bonds get a minus. [40, 45]

The 1-junction represents a node at which all flows of the connecting bonds are equal and efforts algebraically sum to zero. The 1-junction is also known as effort junction or common flow junction. Figure 5.12 shows the basic 1-junction used in bond graph.

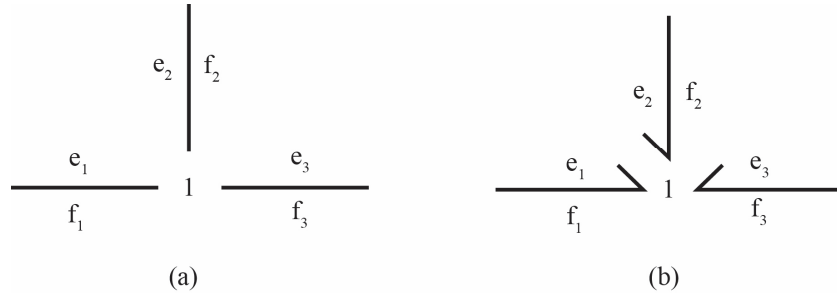


Figure 5.12 Bond graph representation of 1-junction

Using the inward power sign convention showed in Figure 5.12(b), the constitutive relation can be written as follows:

$$e_1 f_1 + e_2 f_2 + e_3 f_3 = 0 \quad (5.22)$$

In the 1-junction all flows are equal, thus,

$$f_1(t) = f_2(t) = f_3(t) \quad (5.23)$$

$$e_1(t) + e_2(t) + e_3(t) = 0 \quad (5.24)$$

In the 1-junction the flows in all bonds are always identical and the algebraic sum of the efforts always vanishes. The signs in the algebraic sum are determined from the half arrow directions following the same rule as the 0-junction. [40, 45]

5.4.2.4 Causality

Causal strokes indicate the direction of the efforts and flows in a bond graph model. The causal stroke is a short, perpendicular line made at one end of bond or port line. The half arrow sign convention for power flow and the causal stroke are completely independent. Figure 5.13 shows two power-bonds with bond graph causal marks with the direction of effort/flow information. The effort information moves toward the causal mark and the flow information moves away from the causal mark. [40, 45]

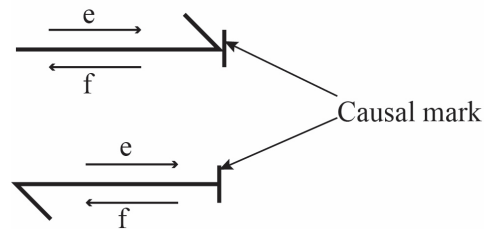


Figure 5.13 Causal marks

Figure 5.14 shows two generalized elements with constitutive laws expressed in a manner consistent with the causal stroke location.

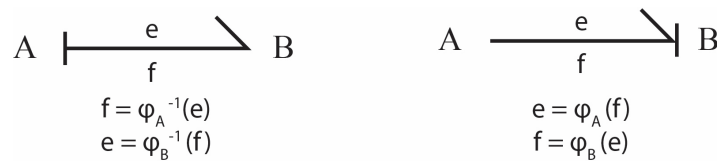


Figure 5.14 Different causality combination

The causality for different elements are shown in Table 5.5 - 5.7

Table 5.5 Causality for basic 1-port elements

Element	Acausal Form	Causal Form	Constitutive law (Linear)
Effort source	Se	Se	$e = e(t)$
Flow source	Sf	Sf	$f = f(t)$
Resistor	R	R	$e = rf$
		R	$f = \frac{1}{R} e$
Capacitor	C	C	$f = C \frac{de}{dt}$
		C	$e = \frac{1}{C} \int f dt$
Inertia	I	I	$f = \frac{1}{I} \int e dt$
		I	$e = I \frac{df}{dt}$

Table 5.6 Causality for basic 2-port elements


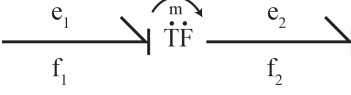

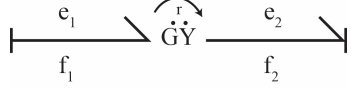
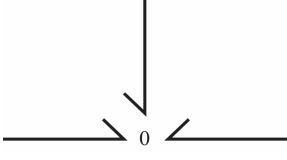
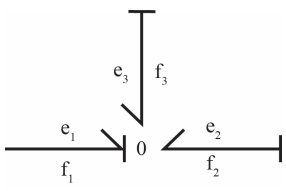
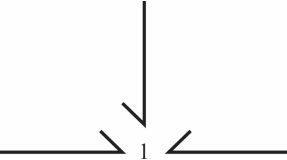
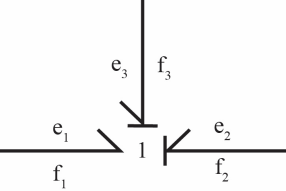
Element	Acausal Form	Causal Form	Constitutive law (Linear)
Transformer			$e_2 = m e_1$ $f_1 = m f_2$
Gyrator			$e_2 = r f_1$ $e_1 = r f_2$

Table 5.7 Causality for basic 3-port elements

Element	Acausal Form	Causal Form	Constitutive law (Linear)
0-junction			$e_1 = e_2 = e_3$ $f_1 = -f_2 - f_3$
1-junction			$f_1 = f_2 = f_3$ $e_1 = -e_2 - e_3$

This section provides the basic concept of bond graph method, its standard elements, power direction of bonds, causality etc. The next section consists of formulation of a 2D drillstring model using bond graph method.

5.4.3 Model & Simulation Results

5.4.3.1 Bond Graph Model

A 2D lumped segment model has been developed in 20-sim to predict the natural frequency of drillsting. This 2D model consists of a series of rigid body and joint sections. This model has been simulated with 20 segments to predict the natural frequency. In the simulation model a fixed-free boundary condition has been used. The schematic of the each rigid body is shown in Figure 5.15 with its velocity components. This rigid body can move along x-axis and y-axis and each rigid body is connected with another rigid body by joint at point p and q in the schematic.

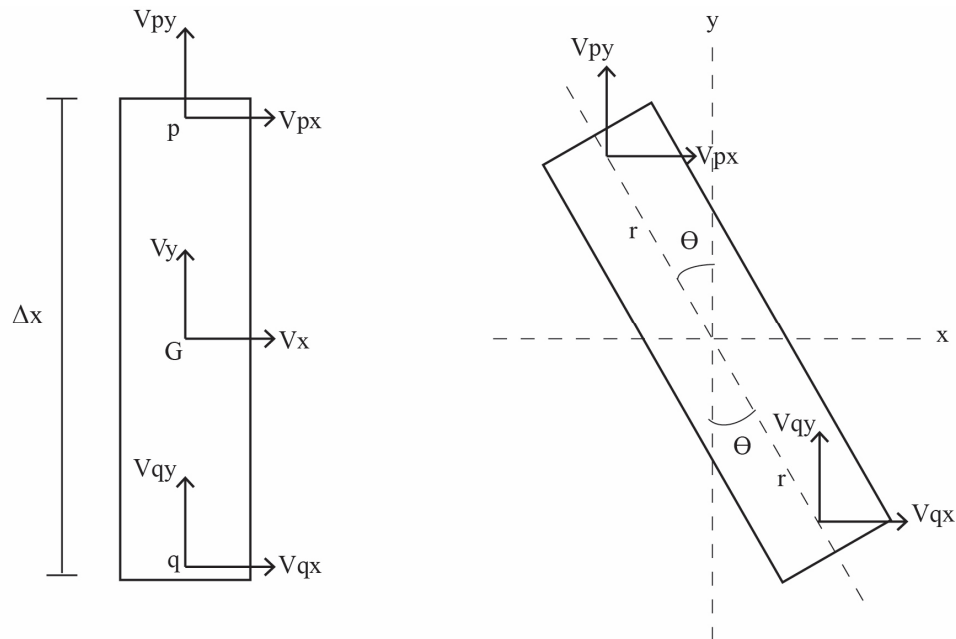


Figure 5.15 Schematic of rigid body segment

Velocity components are calculated as follows:

$$Vp_x = Vx - (r * \cos\theta) * \omega \quad (5.25)$$

$$Vp_y = Vy - (r * \sin\theta) * \omega \quad (5.26)$$

$$Vq_x = Vx + (r * \cos\theta) * \omega \quad (5.27)$$

$$Vq_y = Vy + (r * \sin\theta) * \omega \quad (5.28)$$

The schematic of a joint is shown in Figure 5.16.

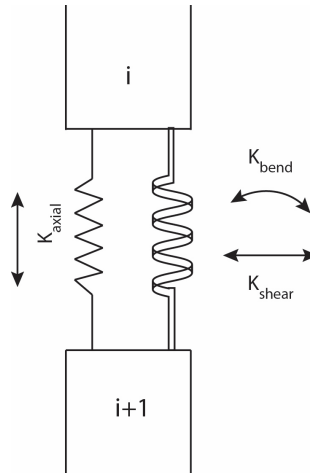


Figure 5.16 Schematic of a joint section

The compliance values (which is inverse of the stiffness values) for a segment of the drillstring are calculated following solid mechanics theory from Karnopp *et al.* [40] as follows:

$$C_{axial} = \frac{1}{K_{axial}} = \frac{\Delta x}{EA} \quad (5.29)$$

$$C_{bending} = \frac{1}{K_{bending}} = \frac{\Delta x}{EI} \quad (5.30)$$

$$C_{shear} = \frac{1}{K_{shear}} = \frac{\Delta x}{kAG} \quad (5.31)$$

Where, Δx is segment length, E is the modulus of elasticity, A is the cross-sectional area, I is the area moment, G is modulus of rigidity, k is the shear coefficient.

The shear coefficient used in the joint connection is obtained from Hutchinson [48] as follows:

$$k = \frac{6(a^2 + b^2)^2(1 + \nu)^2}{7a^4 + 34a^2b^2 + 7b^4 + \nu(12a^4 + 48a^2b^2 + 12b^4)} + \nu^2(4a^4 + 16a^2b^2 + 4b^4) \quad (5.32)$$

Where, ν is the Poisson's ratio, a is the inner radius and b is the outer radius.

The bond graph of the rigid body and the joint connection are shown in Figure 5.17 and 5.18 respectively. All relevant parameters, variables and equations used in the model are presented in Appendix A. Bond graph of the rigid body section in Figure 5.17 corresponds to the schematic of rigid body showed in Figure 5.15. Number 1, 2, 3 in the power input and output sections correspond to the lateral motion due to shear, angular motion due bending and axial motion respectively. Joints are connected to each input and output bond which are connected to another rigid body.

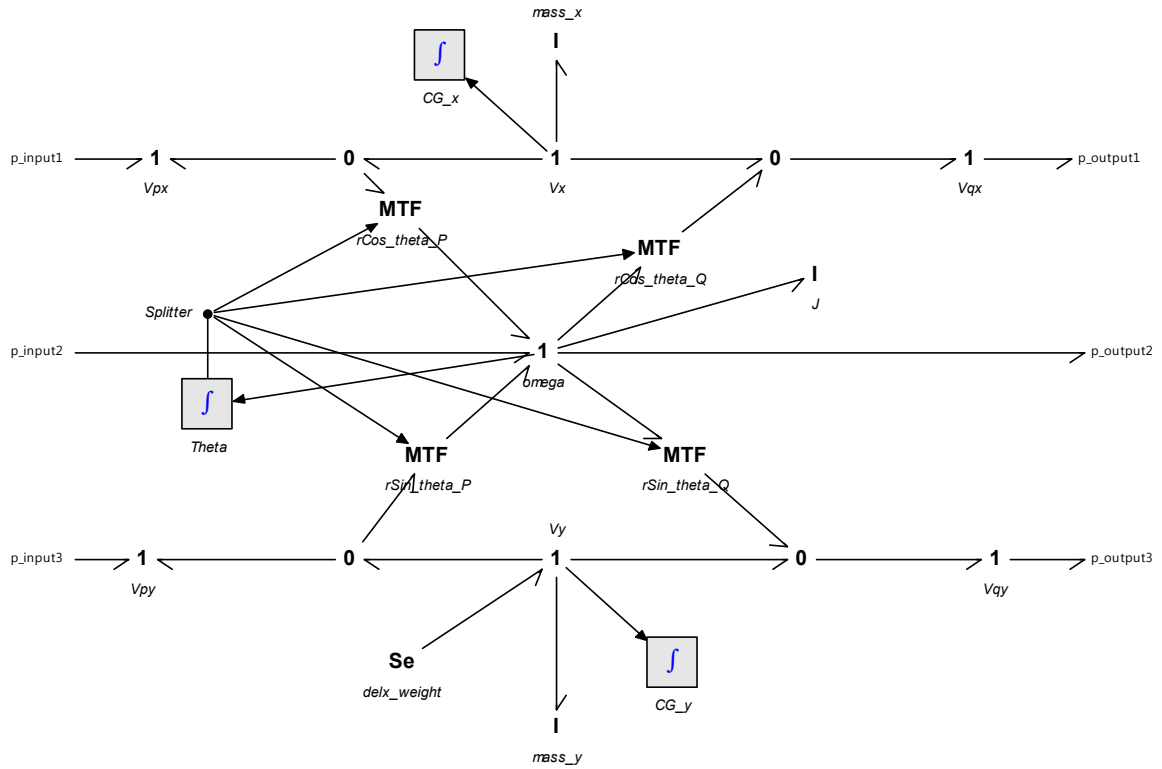


Figure 5.17 Bond graph model of a rigid body

The joint section consists of three compliances and three resistive elements, one each for lateral motion due to shear, angular motion due to bending and for axial motion. The power inputs and outputs are connected to the corresponding rigid body section. Bond graph model for joint section is shown in Figure 5.18 below.

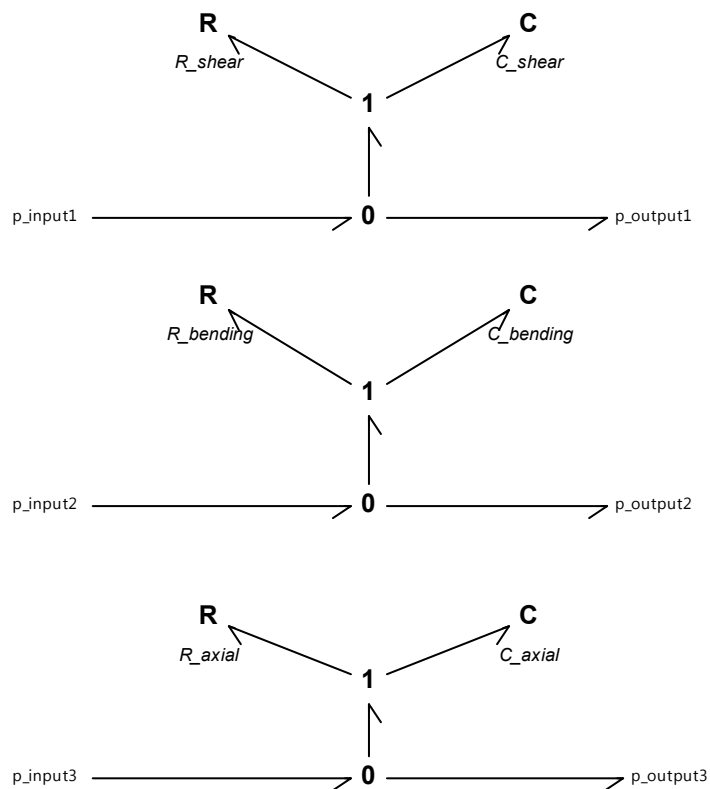


Figure 5.18 Bond graph model of a joint

Figure 4.18 represents the 2D bond graph model of drillstring.

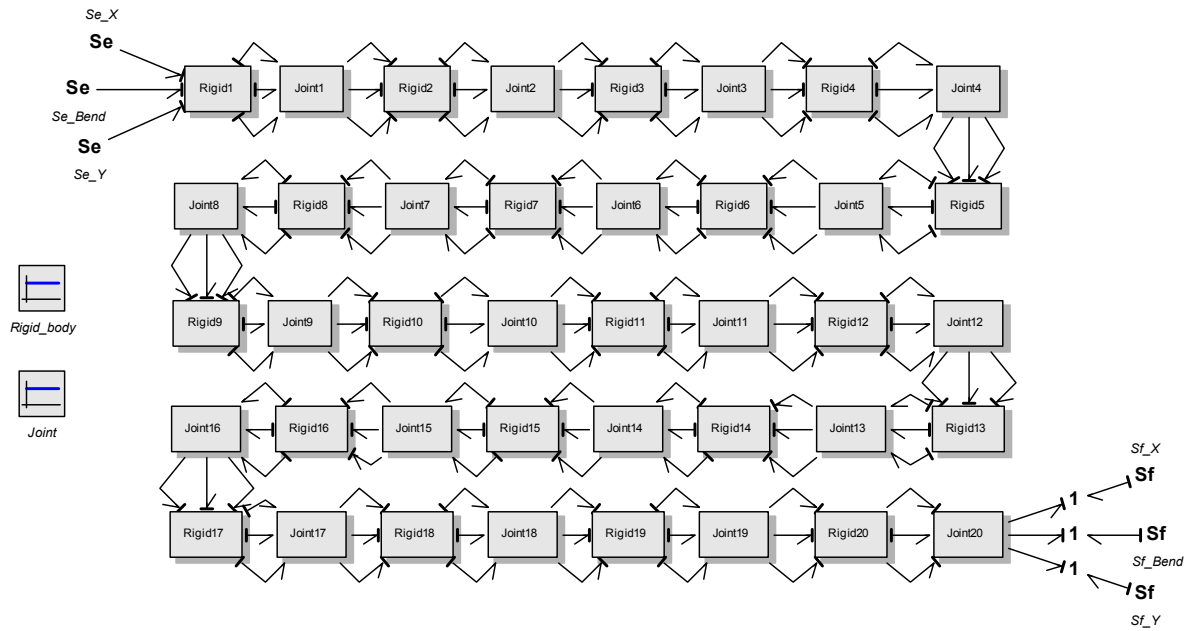


Figure 5.19 Bond graph model of a 2D drillstring model

5.4.3.2 Results and Model Validation

The main objective of this 2D model is to study the natural frequency of the drillstring and to determine the severity of the vibration. The natural frequency calculated from the 2D model has been compared with the theoretical natural frequency for axial and lateral motion of the drillstring. Measured natural frequencies from 2D model and theoretical natural frequencies for axial and lateral motion are listed in Table 5.8 and Table 5.9 respectively.

Table 5.8 Axial Natural Frequency

<i>Length (m)</i>	Measured natural frequency			<i>Theoretical natural frequency</i>		
	f_1 (Hz)	f_2 (Hz)	f_3 (Hz)	f_1 (Hz)	f_2 (Hz)	f_3 (Hz)
30	41.03	122.84	203.88	42.06	126.19	210.31
60	20.52	61.42	101.97	21.03	63.09	105.16

Table 5.9 Lateral Natural Frequency

<i>Length (m)</i>	<i>Measured natural frequency</i>			<i>Theoretical natural frequency</i>		
	f_1 (Hz)	f_2 (Hz)	f_3 (Hz)	f_1 (Hz)	f_2 (Hz)	f_3 (Hz)
30	0.11	0.68	1.90	0.11	0.71	1.99
60	0.03	0.17	0.48	0.03	0.18	0.50

For 30 *m* length of drillstring, the first axial natural frequency measured from the 2D model is 41.03 Hz and the theoretical first axial natural frequency is 42.06 Hz. So the percentage of error is 2.45%. Similarly, for 60 *m* the percentage of error for first axial natural frequency is 2.42%. For 30 *m* length of drillstring, the first lateral natural frequency measured from the model is 0.11 Hz and the theoretical first lateral natural frequency is 0.11 Hz. So the percentage of error is 0%. Similarly, for 60 *m* the percentage of error for first lateral natural frequency is 0%.

Table 5.10 and 5.11 shows the measured lateral natural frequency obtained from the 2D model when different axial load is applied. First three natural frequencies are captured for both 30 *m* and 60 *m* of length. The result shows that increased axial load on the 2D model results in lowered lateral natural frequency. For 30 *m* of length, with no axial load condition the first natural frequency captured from the model is 0.71 *rad/s* and when 2000 *N* axial

load is applied the natural frequency reduces to 0.58 rad/s . Similarly, for 60 m length, when no axial load is applied the first natural is measured from the model is 0.19 rad/s and 0.09 rad/s when 2000 N axial load is applied.

Table 5.10 Lateral natural frequency with axial load for 30m length

Load (N)	Measured natural frequency		
	$\omega_1 \text{ (rad/s)}$	$\omega_2 \text{ (rad/s)}$	$\omega_3 \text{ (rad/s)}$
0	0.71	4.29	11.96
500	0.68	4.25	11.93
1000	0.65	4.21	11.90
1500	0.61	4.17	11.88
2000	0.58	4.13	11.85

Table 5.11 Lateral natural frequency with axial load for 60m length

Load (N)	Measured natural frequency		
	$\omega_1 \text{ (rad/s)}$	$\omega_2 \text{ (rad/s)}$	$\omega_3 \text{ (rad/s)}$
0	0.19	1.08	2.99
500	0.17	1.05	2.97
1000	0.15	1.02	2.94
1500	0.13	0.99	2.92
2000	0.09	0.96	2.90

The model developed is the first generation model of a 2D drillstring which can capture coupled axial and lateral vibration. The frequency analysis validates the model to be working. This model can be used to determine the severity of vibrations in future with more accurate tuning.

6 CHAPTER 6:

SUMMARY AND CONCLUSIONS

6.1 Introduction

This chapter gives a summary of the study presented in this thesis which involves description and contribution of the author in developing a downhole sensor sub, application and testing of its data interpretation method and developing a 2D drillstring dynamic model. The limitation of this present work is also identified and presented in this chapter. Finally, recommendations are provided for future work.

6.2 Summary of Present Work

Past field investigations have established a conclusion that downhole vibration can do severe downhole tool damage even to the extent to tool failure. Due to tool damage or failure the Non-Productive Time increases which is not desirable in industry. Moreover, Rate of Penetration will be decreased with the increasing wear of the drill bit and damage to other drillstring components. The main motivation behind this work is to study the downhole dynamic condition so that the downhole tool failure can be reduced thus saving time and money in the industries by investigating the downhole vibration data.

The present research work gives an overview of a downhole vibration monitoring tool (Sensor Sub) developed in Advanced Drilling Laboratory of Memorial University of Newfoundland. The tool is highly cost effective, whereas in industrial downhole dynamic recorder tools are very expensive and have limitations. The developed sensor sub is designed to record downhole vibration and rotation data at a high sampling rate. A previously developed data interpretation method was applied to field test data. Data recorded in the monitoring tool is the raw data which needs to be processed according to the sensor position. From the interpreted data different modes of vibration can be identified. Methods have been developed to identify stick slip, bit whirl and bit bounce if better data could be achieved from field trial. Downhole rotary speed also can be calculated from the sensor sub data to justify the surface RPM.

A 2D bond graph dynamic model of the drillstring is also proposed using lumped segment approach. This proposed model includes the axial and lateral vibration of the drillstring and

they are mutually dependent on each other. 20-sim software package is used for modelling and simulation. The proposed model can be used to predict the axial and lateral vibration of the drillstring with more accurate tuning in future.

6.3 Limitations of Present Work

The developed downhole vibration monitoring tool has some drawbacks in design. The electrical circuit design is done in the conventional way by connecting the sensors, microcontrollers and other electronics using flexible wires. During drilling operation when downhole vibrations were induced those connections couldn't withstand the vibration and the connections broke down several times during the experiments in field trial. Moreover, the wire connections require more space in the downhole sensor sub to connect all the electronics requiring more material removal from the tool and thus reduces the safety factor. In addition, the mechanical design of the sensor sub met the requirements but there was an error in manufacturing the tool which resulted the damage of sealing in the tool during field experiments.

This downhole vibration monitoring tool is capable of recording downhole dynamic data and store the data in a SD card but does not have any real time transmission facility.

The 2D dynamic bond graph model is proposed based on simple beam theory. This model is valid only if axial and lateral vibration is involved; torsional vibration is not considered in this model. Moreover, no bit rock interaction and effect of fluid flow is taken into consideration in the bond graph model. Another limitation of this work is the proposed 2D model is validated with theoretical results only.

6.4 Recommendations for Future Work

The vibration monitoring tool developed in the Advanced Drilling Laboratory is the first version of the tool. In future the concept developed can be revised as follows:

- Instead of using the wired connection for electronics, a PCB (Printed Circuit Board) can be used to minimize the space requirement and to avoid connection break down or loose connection. Loose connections reduce the sensor performance introducing noise in the system and accelerometers are highly sensitive to noise.
- FPGA (Field Programmable Gate Array) can be used for more advanced tool development. In FPGA data can be sampled at a very high speed than Arduino and data can be recorded in the SD card at high speed i.e. high frequency writing speed into SD card.
- A real time data telemetry system can be developed to know the downhole dynamic conditions instantly.
- A data processing software can be developed for easy data processing.
- Performing laboratory scale experiments before going for any large scale experiment with the developed tool.
- Bit rock interaction and fluid flow can be added in the proposed 2D bond graph model.
- The proposed bond graph model can be used to determine the severity of vibration with more accurate tuning of the model and can be validated with the experimental data.

REFERENCES

- [1] History of Drilling. <http://www.rigsinternational.com/our-offer/history-of-drilling/>
- [2] Jamal J. Azar, G. Robello Samuel (2007), “Drilling Engineering”.
- [3] K. G. Pierce, B. J. Livesay, J. T. Finger (1996), “Advanced Drilling Syatem Study”.
- [4] Mohd Fauzi Hamid, Wan Rosli Wan Sulaiman, “Fundamentals of Petroleum Engineering – Drilling Operations”, Department of Petroleum Engineering, Universiti Teknologi Malaysia.
- [5] Chien-Min Liao, Nicholas Vlajic, Hamad Karki, Balakumar Balachandran, Parametric studies on drill-string motions, International Journal of Mechanical Sciences, Volume 54, Issue 1, January 2012, Pages 260-268
- [6] ReedHycalog™ Drill Bits - <http://www.nov.com/>
- [7] Jardine, S., Malone, D., & Sheppard, M. (1994). “Putting a Damper on Drilling’s Bad Vibration”. Oilfield Review, January 1994.
- [8] Drillstring Dynamics Analysis: Shock & Vibration – Schlumberger. http://www.slb.com/services/drilling/engineering_modeling/optimization/drilling_optimization_real_time/shock_vib.aspx
- [9] Drillstring Vibrations and Vibration Modeling – Schlumberger. http://www.slb.com/~media/Files/drilling/brochures/drilling_opt/drillstring_vib_br.ashx

- [10] Junor, Duncan J. (2007), “Challenges and developments in direct measurement of down hole forces affecting drilling efficiency”, MSc thesis, Robert Gordon University, Aberdeen.
- [11] http://www.unitools.ru/images/chisel_tool_id_62/1.pdf
- [12] <http://simplebooklet.com/publish.php?wpKey=NQTEFlqCvuLiatQW3CSCsH#page=4>
- [13] <http://www.iadd-intl.org/LinkClick.aspx?fileticket=A8Vcf2UnNRI=>
- [14] Elsayed, M.A; Dareing, D.W; Dupuy, C.A, “Effect of downhole assembly and polycrystalline diamond compact (PDC) bit geometry on stability of drillstrings”, Journal of Energy Resources Technology, Transactions of the ASME, Vol. 119, pp 159 – 163.
- [15] M.P. Dufeyte, H. Henneuse. (1991) “Detection and Monitoring of the SlipStick Motion”, SPE 21945, SPE/IADC, drilling conference, Amsterdam.
- [16] P.C. Kriesels, W.J.G. Keultjes, P. Dumont, Issam Huneidi, O.O. Owoeye, R.A. Hartmann (1999), “Cost Savings through an Integrated Approach to Drillstring Vibration Control” SPE-57555-MS, SPE/IADC Middle East Drilling Technology Conference, Abu Dhabi, UAE.
- [17] D.K. Ashley, X.M. McNary, and J.C. Tomlinson. (2001). “Extending BHA Life with Multi-Axis Vibration Measurements”. SPE/IADC Drilling Conference, Amsterdam, Netherlands.
- [18] Spyro J. Kotsonis (1994), “Effects of Axial Forces on Drillstring Lateral Vibration”, M.Sc. thesis, Rice University.
- [19] Jamal J. Azar, G. Robello Samuel (2007), “Drilling Engineering”.

- [20] W.D. Aldred, M.C. Sheppard (1992), “Drillstring vibrations: a new generation mechanism and control strategies”, Proceedings of the 67th Annual Technical Conference and Exhibition of SPE, Washington, DC.
- [21] A.S. Yigit, A.P. Christoforou (1998), “Coupled torsional and bending vibrations of drillstrings subject to impact with friction” Journal of Sound and Vibration, 215(1), pp. 167–181.
- [22] Martin E. Cobern, Mark E. Wassell, “Drilling Vibration Monitoring & Control System”, APS Technology Inc, Cromwell, CT, USA.
- [23] Vibration Memory Sub, APS Technology. <http://www.aps-tech.com/tds/APS-VMS.pdf>
- [24] Paul E. Pastusek, Eric Sullivan, Thomas Mitchell Harris (2007), “Development and Utilization of a Bit Based Data Acquisition System in Hard Rock PDC Applications”, SPE/IADC Drilling Conference, February 20-22, Amsterdam, Netherlands.
- [25] D.A. Close, S.C. Owens, J.D. MacPherson (1988), “Measurement of BHA Vibration Using MWD”, SPE/IADC Drilling Conference, 28 February-2 March, Dallas, Texas.
- [26] S.A. Zannoni, C.A. Cheatham, C-K.D. Chen, C.A. Golla (1993), “Development and Field Testing of a New Downhole MWD Drillstring Dynamics Sensor”, SPE Annual Technical Conference and Exhibition, 3-6 October, Houston, Texas.
- [27] Rana, Pushpinder Singh, Project Manager & PhD student, Advanced Drilling Laboratory, Memorial University of Newfoundland.

- [28] <https://www.sparkfun.com/products/9836>
- [29] http://www51.honeywell.com/aero/common/documents/myaerospacecatalog-documents/Defense_Brochures-documents/HMC5983_3_Axis_Compass_IC.pdf
- [30] <http://www.digikey.com/product-detail/en/HMC5983-EVAL/342-1094-ND/3465633>
- [31] <http://arduino.cc/en/Main/arduinoBoardLeonardo>
- [32] <http://www.adafruit.com/products/254>
- [33] Advanced Drilling Laboratory, Memorial University of Newfoundland, St. John's, NL, Canada.
- [34] Butt, S. (2014). Unpublished report for Husky Energy, Suncor Energy and Noble Drilling Canada.
- [35] Qian Gao (2014), "Development of Laboratory and Field Drilling Tools to Measure Bit Operating Conditions and Drill String". Unpublished M.Eng. thesis, Memorial University of Newfoundland, St. John's, NL, Canada.
- [36] FFT tutorial, ELE 436 Communication System, Department of ECE, University of Rhode Island.
- [37] <http://cdn.adinstruments.com/adi-web/techniques/tn-SignalFiltering.pdf>
- [38] <http://mirlab.org/jang/books/audiosignalprocessing/example/output/butter05.png>
- [39] Smith, S. "Digital Signal Processing: A Practical Guide for Engineers and Scientists".

- [40] Dean C. Karnopp, Donald L. Margolis, Ronald C. Rosenberg. “System Dynamics: Modeling, Simulation, and Control of Mechatronic Systems” -5th Edition.
- [41] Rao, Singiresu S. “Mechanical vibrations”- 5th Edition.
- [42] <http://www.bondgraph.org/>
- [43] <http://www.20sim.com/>
- [44] Robert Thomas McBride (2005), System Analysis Through Bond Graph Modelling, PhD thesis, University of Arizona.
- [45] Jan F. Broenink, “Introduction to Physical Systems Modelling with Bond Graphs”, University of Twente, Dept EE, Control Laboratory, Enschede Netherlands.
- [46] Peter Breedveld, “Bond Graphs” University of Twente, Enschede Netherlands.
- [47] <http://engineering.sdsu.edu/~jvaldes/sd/sdof.pdf>
- [48] Hutchinson, J.W. (2001) “Shear Coefficient for Timosenko Beam Theory”, ASME Journal of Applied Mechanics, Vol. 68, No. 1, pp.87-92.

APPENDICES

Appendix A

20-sim Programming Codes

// rigid body codes//

parameters

```
real rho = 7850;           //Steel density, Kg/m3
//real E = 200e9;          // Elastic modulus, Pa
//real G = 80e9;           //Shear modulus, Pa
real pipe_L = 60;          //Drillpipe length, m
real pipe_n = 20;          //Number of segments
real pipe_OD = 0.1143;     //Drillpipe OD, m (4.5")
real pipe_ID = 0.0889;     //Drillpipe ID, m (3.5")
```

variables

```
real global pipe_delx;
real global pipe_area;
real global pipe_mass;
real global pipe_weight;
real global r;             //distance from center
real global J;             //moment_of_inertia
```

equations

```
pipe_delx = pipe_L/pipe_n;
pipe_area = 3.1416*(pipe_OD^2 - pipe_ID^2)/4;
```

```

pipe_mass = rho*pipe_area*pipe_delx;
pipe_weight = pipe_mass*9.81;
r = pipe_delx/2;
J = (pipe_mass*(3*((pipe_OD/2)^2 + (pipe_ID/2)^2) + pipe_delx^2))/12;

```

// Codes for joint//

parameters

```

real E = 200e9;                // Elastic modulus, Pa
real G = 80e9;                // Shear modulus, Pa
real pipe_OD = 0.1143;        // Drillpipe OD, m (4.5")
real pipe_ID = 0.0889;        // Drillpipe ID, m (3.5")
real neo = 0.3;                // Poison ratio
//real k = 0.579;              //shear coefficient, (using Hutchinson, 2001 |
for poison ratio, neo = 0.3)

real spring_resistance_shear = 2000;
real spring_resistance_axial = 2000;
real spring_resistance_bending = 100;

```

variables

```

real global pipe_delx;
real global pipe_area;
real global K_shear;
real global K_axial;
real global K_bending;
real global I;                //area moment
real global a;
real global b;
real global k;
real global R_shear;

```

```

real global R_axial;
real global R_bending;

```

equations

```

I = (3.1416/4)*((pipe_OD/2)^4-(pipe_ID/2)^4);
K_shear = pipe_delx/(k*pipe_area*G);
K_axial = pipe_delx/(E*pipe_area);
K_bending = pipe_delx/(E*I);
a = pipe_ID/2;
b = pipe_OD/2;
k
=
6*((a^2+b^2)^2*(1+neo)^2)/(7*a^4+34*(a^2)*(b^2)+7*b^4+neo*(12*a^4+48*(a^2)*(b^
2)+12*(b)^4)+neo^2*(4*a^4+16*(a^2)*(b^2)+4*b^4));
R_shear = spring_resistance_shear;
R_axial = spring_resistance_axial;
R_bending = spring_resistance_bending;

```

Appendix B

MATLAB FFT Codes

```
% Example - How to create a frequency spectrum in MatLab:

clear all;
close all;

% Import time t and data f(t) from Excel
% NOTE: You must put the Excel data file in the same folder as the
MatLab m-file
%
% The format of the data in the Excel file must match what we read here:
%     Cell B3 = N (number of data points)
%     Cell B4 = f_s (sampling frequency)
%     Cell A7 = first time data point (the time column is column A)
%     Cell B7 = first f(t) data point (the f(t) column is column B)
%
xls_filename = 'C:\Users\ruSseL\Dropbox\MUN\Project work\09. FFT\03.
FFT\FFT - Torsional\f.xlsx';
sheet_number = 1;
N = xlsread(xls_filename,sheet_number,'B3');
f_s = xlsread(xls_filename,sheet_number,'B4');
time_column = 'A'; % Column letter
frequency_column = 'B';
first_row = 7; % Row number
last_row = first_row + N;
first_row = num2str(first_row);
last_row = num2str(last_row);
data_range1 = [time_column first_row ':' time_column last_row];
t = xlsread(xls_filename,sheet_number,data_range1); % time data
data_range2 = [frequency_column first_row ':' frequency_column
last_row];
f = xlsread(xls_filename,sheet_number,data_range2); % signal data

%Calculated values:

T = N/f_s; % Total sample time (s)
del_t = 1/f_s;
del_f = 1/T;
f_fold = f_s/2; % Folding frequency = max frequency of FFT = NYQUIST
frequency
N_freq = N/2; % Number of discrete frequencies

% FFT of the time signal

for k = 0:N/2
```

```

    frequency(k+1) = k*del_f;
end

%NFFT = 2^nextpow2(N); % Use power of 2 for FFT (NOT necessary in
Matlab, but faster)
%F = fft(f,NFFT); % Compute FFT for case with integer multiple of 2
data points
F = fft(f,N); % Compute FFT for general case: N not necessarily a
multiple of 2

for k = 0:N/2
    Magnitude(k+1) = abs(F(k+1))/(N/2);
end
Magnitude(1) = Magnitude(1)/2; % Divide first term by a factor of 2

% Plot the frequency spectrum

figure(1)
hold on;
% plot(frequency,Magnitude,'-
bo','MarkerFaceColor','r','MarkerEdgeColor','r','LineWidth',2)
plot(frequency,Magnitude)
%title('FFT Frequency Spectrum','FontWeight','Bold','FontSize',16)
title('FFT Frequency Spectrum')
xlabel('frequency, f (Hz)','FontWeight','Bold')
ylabel('|F|','FontWeight','Bold')
xmin = 0;
xmax = f_fold;
xlim([xmin xmax])
% ylim([0 3])
% grid
hold off;

```


MATLAB Magnetometer Data Smoothing Codes

```
clear all
close all

load MgSm207_217v2_1.txt % Import data from text file
t = MgSm207_217v2_1(:,1);
th = MgSm207_217v2_1(:,2);
S = size(th);
N = S(1);
j = 1;
for i=2:N;
    del = th(i)-th(i-1);
    if del > 0.25
        T(j) = t(i-1);
        P(j) = th(i-1);
        j = j+1;
    end

    if i == N
        T(j) = t(i);
        P(j) = th(i);
    end
end

plot(t,th);
hold on
plot(T,P,'r');
xlabel('time (s)');
ylabel ('radian');
title ('Magnetometer data smoothing');

for k=2:j-1
    delP=P(k)-P(k-1);
    delT=T(k)-T(k-1);
    omega(k-1)=(delP/delT)/0.1047 % Instantaneous RPM
end
avg = mean (omega) % Average RPM
```